The Growth of Large-Scale Single-Crystal Monolayer Transition Metal Disulfide Materials in High-Vacuum System Based on Passivated Semiconductor

Kunpeng Zhang

University of York

Electronics Engineering

December 2020

Abstract

Two-dimensional transition metal disulfides (TMDs) possess fantastic physical properties. However, many as-prepared TMDs are limited in sample size, which highly hinder their wide applications in high-performance electrical devices. We designed the growth mode by combining the passivation method and molecular beam epitaxial (MBE) system, so as to obtain a full-coverage single-crystal monolayer transition metal disulfide material.

We have successfully obtained the S / GaAs (111) B substrate and found the domain structures unidirectionally aligned. Every drop-shaped domain has nearly same size and direction which this is solid foundation for the next MBE growth. Also, this is the first time that AFM was used to observe the domain structures on GaAs (111) B substrate passivated by sulfur and the domains with consistent directions were observed, which is believed the passivated S atoms homogenous deposition on GaAs (111).

The monolayer CoS_2 was measured by in-situ reflective high-energy electron diffraction, atomic force microscopy, X-ray photoelectron spectroscopy, scanning electron microscopy and transmission microscopy, which demonstrated the monolayer CoS_2 was 100%-coverage, single-crystal and monolayer film on the substrate of GaAs. Monolayer CoS_2/GaAs was fabricated as a heterojunction field effect transistor (FET) transistor in order to tune and improve the properties of GaAs. Theoretical calculation indicate that the grown monolayer CoS_2 on GaAs is a semiconductive and antiferromagnetic film, which well correspond to experimental results. Besides, monolayer PtS_2 film also can be grown by this method, which single-crystal full-coverage can be achieved. By calculation results, the grown monolayer PtS_2 is one of nonmagnetic semiconductor. In this project, single-crystal platinum disulfide film was successfully grown on GaAs substrate, and its thickness, coverage and chemical composition were confirmed by various measurement methods.

List of Contents

Abstract 2

List of Contents 3

List of Figures 6

Acknowledgements 13

Declaration 14

Chapters 15

Chapter 1 Introduction 15

1.1 Two-dimensional Materials 17

1.2 Transition Metal Dichalcogenides Materials (TMDCs) 19

1.3 Growth methods for two-dimensional materials 21

1.4 Antiferromagnetic Property 23

Chapter 2 Film Growth Theory 24

2.1 The Process of Film Nucleation 25

2.2 Concept of Interface Phase and its Application in Sulfide Passivation on GaAs (111) 27

2.3 Homoepitaxy and Heteroepitaxy 30

Chapter 3 Theory Background and Literature Review 34

3.1 Sulfur-passivation GaAs 35

3.2 Two-dimension Materials Growth 41

3.3 The Growth of 2D Transition Metal Chalcogenide Materials by Passivated GaAs 44

Chapter 4 Experimental Techniques 46

4.1 Vacuum Film Growth 47

4.2 Molecular Beam Epitaxy (MBE) Technique 48

Chapter 5 Measurement Techniques 53

5.1 Reflective High-Energy Electron Diffraction (RHEED) 55

5.2 XPS Measurement (X-Ray Photoelectron Spectroscopy) 60
5.3 Scanning Electron Microscopy Measurement (SEM) 64
5.4 Atomic Force Microscopy (AFM) 67
5.5 Transmission Electron Microscopy 73
5.6 Superconducting Quantum Interferometer Device Measurement 75
Chapter 6 Sulfur-passivation Method on GaAs Substrate 77
6.1 Background 78
6.2 Sulfide passivation on the GaAs (111) B 80
6.3 RHEED Detection of S-Passivation GaAs 82
6.4 XPS Measurement of S/GaAs (111) 84
6.5 AFM Measurement of S/GaAs (111) 86
6.6 Summary of Findings 88
Chapter 7 The Growth of Single Crystal of Monolayer CoS_2 89
7.1 Introduction of CoS_2 90
7.2 Sample Growth of Monolayer CoS_2 93
7.3 RHEED Patterns of Monolayer CoS_2 95
7.4 XPS Measurement and Analyze of CoS_2 97
7.5 Scanning Electron Microscopy (SEM) Measurement of CoS_2 on GaAs and Analysis 98
7.6 AFM Measurement of Monolayer CoS_2 100
7.7 TEM Measurement Result and Analysis 102
7.8 I-V measurement of CoS_2/GaAs (111) and Analysis 106
7.9 Antiferromagnetic Monolayer CoS_2 Measurement and Analysis 110
7.10 Results and Analysis of Theoretical Calculation 112
7.11 Summary of Findings and Discussion 118
Chapter 8 The Growth of Layered 2D Material PtS_2 121
8.1 Background of TMDs Monolayer by MBE System Growth 122
8.2 Growth of PtS_2 126

8.3 RHEED Patterns of PtS_2 and Analyses 128

8.4 XPS Measurement of PtS_2/GaAs 131

8.5 SEM Measurement of Full Coverage PtS_2 133

8.6 AFM Measurement of PtS_2 135

8.7 PtS_2 Theoretical Calculation and Analysis 137

8.8 Summary of Findings and Discussion 139

Chapter 9 Conclusions 141

Chapter 10 Future Work 143

Reference 145

List of Figures

Fig 1.1 temperature-dependence susceptibility χ for para-, ferro-, and antiferromagnetic material[67]. 24

Fig 2.1 Spherical corona like crystal nuclei on substrate.......... 25

Fig 2.2 Interface phase between solid and liquid.......... 30

Fig 3.1 the top panel shows the atomic configurations of clean (111) A and (111) B surfaces, while the bottom panel describes the model that interprets the experimental data after treatment and annealing, corresponding to nitrogen adsorption at the B surface and to adsorption of sulfur on the A one. It is proposed that sulfur atoms on the A surface are dimerized[85].......... 37

Fig 3.2 adsorption configurations of sulfur atoms on the GaAs(111)Ga surface: (a) the exchange site and (b) the on-top site[86] 38

Fig 3.3 the Ga-S bond and As-S bond length on the GaAs (111) Ga surface and GaAs (111) As surface with an adsorbed S monolayer in the top and exchange sites.[86] 39

Fig 3.4 a, A schematic illustration of the structural transformation from the sputtered Nb film to a 2H-$NbSe_2$ film. b, A photograph of a Nb film and a selenized Nb film on the 2-inch double-side polished sapphire wafers, which are homogeneous and transparent. c, AFM images and the corresponding height profiles of an as-sputtered Nb film, a selenized ($NbSe_2$) film and a heat-treated (50 °C for 5h in air) $NbSe_2$ film. A height increase of ~50% is exhibited after selenization. Scale bars, 1 μm. d, XPS spectra of Nb 3d and Se 3d from a selenized Nb film (0.7 nm in thickness) after long-time exposure to air. e, Raman spectra with perpendicular polarization for the $NbSe_2$ films after different treatments[8]. 42

Fig 3.5 a, A low-magnification STEM image showing the polycrystalline structure of a $NbSe_2$ film; the grain boundaries are marked by green dashed lines. b, The atomic structure of a tilt grain boundary with a misorientation of ~25°,

where the pentagon (yellow), heptagon (red) and hexagon (blue) structures in the grain boundary region are marked out accordingly. Only 5–7 pairs exist. c, The lattice structure in a single-crystalline grain, showing a perfect single-crystalline structure (as confirmed by the inset fast Fourier transform pattern), where no obvious atomic defect is detected even after exposure to air for several days. d, Atomic structure image of the area marked out by a purple square in c, with the inset showing the atomic model of $NbSe_2$ (top view) with 2Hc structure. e,f, STEM images at different magnifications showing the atomic structure of the NbSe2 film after heat treatment at 50 °C for 5 h in air, where no obvious atomic vacancy is observed. Scale bars, 20 nm (a), 2 nm (b,d,f), 5 nm (c,e).[8] 43

Fig 3.6 schematic diagrams of NbSe2 films on a van der Waals GaAs surface realized by the Se termination of surface dangling bonds (a), and by the growth of GaSe thin films on Se-GaAs (h).[58] 45

Fig 4.1 the schematic of MBE system: (1) pump system, (2) manipulator, (3) RHEED gun, (4) transfer arm, (5) main chamber, (6) laser of MOKE system, (7) e-beam source, (8) evaporator source 51

Fig 4.2 the illustration of sample holder. The molybdenum sample holder is 14mm length and 12mm width. The clamps were fixed by molybdenum fine screws. 53

Fig 5.1 diagram of the device reflecting high energy electron diffraction in MBE vacuum chamber. 56

Fig 5.2 RHEED electron beam grazing on the sample surface. (A) incidence beam (black) on the film (yellow) that is grown on the substrate (blue), and reflective beam (green) to fluorescent screen. (B) cross section views of the sample and electron beams. 57

Fig 5.3 schematic representation of electron scattering mechanism, film morphology and RHEED diffraction of various surface structures. (A) and (B) schematic and RHEED diffraction of electron scattering and single-crystal layered growth films. (C) and (D) schematic and RHEED diffraction of

electron scattering in single-crystal island films. (E) and (F) the diagram of electron beams incidence onto multi-crystal of films and RHEED diffraction of multi-crystal films...58
Fig 5.4 illustration of XPS measurement. X-ray focusing onto surface of substrate and collected electrons from a smaller area of surface. 61
Fig 5.5 the photoelectric process of XPS. Incident x-ray motivating an electron of 1s shell. 62
Fig 5.6 relative sensitivities of the elements: 1s orbital (red line), 2p orbital (green line), 3d orbital (blue line), 4d orbital (navy one) and 4f orbital (pink one). 63
Fig 5.7 schematic of SEM working principle. 66
Fig 5.8 SEM image of hBN in previous study[18]. SEM image of aligned hBN domains on the Cu (110) substrate...67
Fig 5.9 AFM structure diagram: the probe is connected with the cantilever arm, and the optical position detector determines the three-dimensional position of the probe by receiving the laser signal...69
Fig 5.10 Schematic diagram of probe and sample surface. The feedback system controls and maintains a constant distance (d) between the probe and the sample surface...70
Fig 5.11 structure and AFM imaging of monolayer MoS_2. a, three-dimensional representation of the structure of MoS_2. Single layers, 6.5 Å thick, can be extracted using scotch tape-based micromechanical cleavage. b, Atomic force microscope image of a single layer of MoS_2 deposited on a silicon substrate with a 270-nm-thick oxide layer. c, Cross-sectional plot along the red line in b[28]. 71
Fig 5.12 layout of components in a basic TEM 74
Fig 5.13 SQUID working principle and device diagram. a, diagrammatic sketch of signal collection coil; b, voltage response of sample measurements; c, instrument external photo.[93]...76

Fig 6.1 the GaAs (111) B dipped into $(NH4)2Sx$ solution. 80

Fig 6.2 RHEED patterns taken from S/GaAs (111) B surface with 500K annealing for 20 mins. A) the diffraction pattern from [1 1 -2] axis crystal orientation of the S/GaAs (111). B) the [1 0 -1] direction of crystal orientation. 83

Fig 6.3 XPS data of S/GaAs substrate. A) the S 2s peak with character peak of 227.9eV. B) the Ga 3d peak at binding energy of 18.9eV. C) the As $3p_{1/2}$ and As $3p_{3/2}$ at 141.1eV and 145.6eV respectively. D) the overview XPS of S/GaAs (111)..85

Fig 6.4 the AFM measurement of GaAs substrate and S/GaAs substrate and their corresponding heights. A) the average roughness of S/GaAs with 0.5Å which is the AFM equipment minimum accuracy. B) the S-passivation GaAs roughness under 2nm. 87

Fig 7.1 the illustration of atomic CoS2 structure with lattice parameter of a 5.538Å [45]. The cubic CoS_2 lattice parameter is 5.538Å......................................91

Fig 7.2 X-ray photoelectron spectra of the (E) Co 2p and (F) S 2p regions for as-synthesized (upper black traces) and electrochemically characterized (lower magenta traces) CoS_2 film electrodes[43]...92

Fig 7.3 in-situ RHEED images during growth of CoS_2. A) the RHEED pattern of S/GaAs from [1 1 -2] crystal orientation. B) RHEED pattern from [1 0 -1] direction after deposition of cobalt atoms. C) RHEED image of monolayer CoS_2 [1 0 -1] after 750K post annealing. D) after post annealing, the CoS_2 patten from [1 1 -2] direction..95

Fig 7.4 In-situ RHEED pattern d-spacing plot of [1 1 -2] crystal orientation: (A) GaAs (111), (B) single-crystal CoS_2...96

Fig 7.5 the X-ray photoelectron spectroscopy of S 2s and Co 2p from the monolayer cobalt disulfide. (A) the S 2p character peak at 226.4eV. (B) CoS_2 character peak at 778.6 and 793.4ev..97

Fig 7.6 passivated method growth of 100% coverage film. A) the SEM image of sample at the boundary between clamp and film which the dark part is the

monolayer of CoS_2 and the light part is GaAs substrate. B) the SEM image of the film area. 98

Fig 7.7 atomic force microscopy of CoS_2 monolayer. A) the average roughness of $5 \times 5\mu m$ area which is under ± 1Å. B) a cross line of the sample with roughness of ± 1.8Å. 101

Fig 7.8 cross-section bright-filed scanning TEM micrography of Al (3nm)/ CoS_2 (1ML)/ GaAs (111) in [1 0 -1] crystal orientation. The CoS2 of monolayer can be seen two layers atoms which the lattice constant is larger than GaAs. 103

Fig 7.9 the TEM image and its atomic structure diagram of cobalt disulfide. The lattice constant a of monolayer CoS_2 is 3.8Å. The atomic structure indicates the CoS_2 with 2H phase 104

Fig 7.10 HAADF-EDS images of CoS_2 on GaAs. A) HAADF image of Co. B) HAADF of element sulfur. C) and D) the element images of Ga and As respectively. 105

Fig 7.11 the I-V curve of undoped GaAs. (111) at room temperature, which the resistance is $3.7 \times 108\Omega$. 106

Fig 7.12 the structure of CoS_2/GaAs transistor; the monolayer CoS_2 on GaAs substrate and Al_2O_3 capped on the CoS_2 film; indium as source, drain and top gate electrodes. 107

Fig 7.13 the temperature-dependence and gate-voltage CoS_2/undoped GaAs (111) semiconductor. (A) temperature-dependence I-V curve of CoS_2/GaAs from 60K to 300K. (B) the I-V curve from ohmic curve to Schottky curve. (C) tuning gate-voltage of transistor at room temperature. (D) zoom-in the gate-voltage tuning transistor of CoS_2/undoped GaAs. 108

Fig 7.14 the structure of Al/CoS2/GaAs sample, which the Al capping layer thickness is 3nm and CoS_2 is 0.87nm. 110

Fig 7.15 FC (Field Cooling) and ZFC (Zero Field Cooling) measurement of monolayer CoS_2 film from 300K to 2K; the antiferromagnetic feature peak at 82K in FC line. 111

Fig 7.16 Single layer CoS_2 atomic structure: (a) top view, (b) side view, (c) polyhedral coordination diagram. 112
Fig 7.17 The possible magnetic configurations of monolayer CoS_2 are: (a) ferromagnetic configuration FM, (b) antiferromagnetic configuration AFM 1, (c) AFM2. The red arrows are used to indicate the spin down and blue for up. 113
Fig 7.18 Spin resolved charge density map of the ground state of a single layer of CoS_2. The yellow (blue) isosurface represents the positive (negative) spin charge density respectively. The isosurface of spin charge density is 0.04 e/$Å^3$. 115
Fig 7.19 The electronic band structure and density of states diagram of single layer CoS_2. The blue (red) lines indicate spin up (spin down) respectively. The Fermi level is 0 eV. 116
Fig 7.20 The local density of states (LDOS) diagram of single layer CoS_2. The Fermi level is 0 eV. 117
Fig 8.1 constant current STM topography of MoS_2 on Gr/Ir (111). (a) MoS_2 coverage of 0.6 layers. (b) MoS_2 coverage of 1.4 layers. Small areas of exposed Gr are visible. The TL forms islands of ≈20 nm diameter. Gr wrinkles are visible in the lower section in both typographs. STM parameters: (a) V = 1.5V, I = 0.01 nA; (b) V = 1.0V, I = 0.08 nA; each image size is 200 × 190 $nm2$[70]. 123
Fig 8.2 schematic drawing of crystal structure of PtS_2 in 3D, top- and side-views. Blue balls represent Pt atoms and S atoms are presented by yellow balls[116]. 124
Fig 8.3 atomic force microscopy (AFM) image of the flakes of the exfoliated PtS_2 film[116]. 125
Fig 8.4 presents the RHEED patterns of PtS_2 growth on GaAs. (A) the passivated S/GaAs (111) substrate from crystal orientation of [1 1 -2]. (B) the disappeared RHEED from [1 1 -2] after 1 ML Pt growth. (C) after post annealing at 480℃ for 60 mins. (D) the PtS_2 monolayer film from the

orientation of [1 0 -1]. 129

Fig 8.5 X-ray photoelectron spectroscopy of monolayer PtS_2. (A) the character peaks of $4f72$ and $4f52$ at 72.4 eV and 75.7 eV. (B) the S2s character peak of $PtS2$ at 226.76 eV. (C) Ga3s and S2p peaks around 160 eV. (D) the overview XPS of PtS_2. 132

Fig 8.6 the SEM measurement images of PtS2 morphology. (A) the clamp boundary (orange dash line) between GaAs substrate and PtS2 with scale bar $200\ \mu m$. (B, C and D) center area of the sample with different resolution of $100\ nm$, $2\ \mu m$ and $200\ \mu m$ scale bar. 134

Fig 8.7 the AFM measurement of platinum disulfide monolayer. (A) the AFM image of the stair between the PtS_2 monolayer and GaAs substrate. (B) the height curve of the sample with the thickness of 0.71nm. 135

Fig 8.8 The atomic structure of PtS_2 monolayer: (A) top view, (B) side view, (C) coordination diagram of polyhedron. 137

Fig 8.9 The electronic band structure and density of states diagram of single layer PtS_2. The blue and red lines indicate spin up and spin down respectively. The Fermi level is 0 eV. 138

Table. 1 The lowest energy value of closed packed monolayer and bilayers of homogenous epitaxy. 31

Table. 2 The lowest energy value of closed packed monolayer and bilayers of heterogenous epitaxy. 32

Table. 3 The energy difference between AFM1 and NM, FM, AFM2 in the antiferromagnetic configuration of monolayer CoS_2. 114

Table. 4 Magnetic moments of atoms and total magnetic moments of unit cell in monolayer CoS_2 ground state system. 114

Table. 5 Energy difference between nonmagnetic and FM, AFM1, AFM2 of single layer PtS_2. 137

Table. 6 The magnetic moment of each atom and the total magnetic moment of unit cell in the ground state system of single layer PtS_2. 138

Acknowledgements

A paper is a summary of the research work and achievements over the years, which can only be achieved with the help of many people. I thank the people around me for their help and support. These people's support for me in these four years is an important part of my achievements in scientific research.

First of all, I would like to thank Prof. Yongbing Xu for providing me with a healthy and independent doctoral research opportunity and greatly supporting my research. He gave me very professional guidance and advice, and he encouraged me to develop freely in the field I was interested in.

I would also like to thank Dr. Iain for his guidance and training during my doctoral period, which enabled me to have the basic qualities of a doctoral student. The technicians, Mr Jonathan Creamer and Mr Charan Panesar in the electronic engineering department of York University have also paid a lot for my research work in recent years. Thank them for their support and maintenance of MBE laboratory and super clean room.

Thank you for advice and help of Dr. Jing Wu in my Ph. D career. Thanks to you, my practical experience has improved, and I benefited a lot during the whole doctoral period.

During my four-year doctoral career, my family's support is an important factor for me to stick with it. My family's support and company are crucial for me to get through difficulties.

In York-Nanjing University joint laboratory, there were many people whom I would like to thank: Prof. Liang He, Dr Yao Li, Mrs Qian Wang, Dr Long Yang, Mr Qinwu Gao and Mr Yizhe Sun.

Finally, my colleagues' support is unparalleled and I sincerely thank them. Your names are: Dr Xianyang Lu, Dr Yu Yan, Dr Junlin Wang, Dr Yichuan Wang, Mr Guanqi Li, Mr Xiangyu Zheng, Mr Wenjia Li, Mr Lingyu Yan, Mr Hua Lin.

Declaration

I declare that this thesis titled, 'The Growth of Large-Scale Single-Crystal Monolayer Transition Metal Disulfide Materials in High-Vacuum System Based on Passivated Semiconductor', and the work presented in it are my own.

I ensure that this thesis is original work. This work has not previously been presented for an award at this, or any other. All sources are acknowledged as Reference.

Where the thesis is based on work done by myself jointly with others, I have made clear exactly what was done by others and what I have contributed myself.

Chapters

Introduction

Since successful synthesis of Graphene by top-down methods in 2004, graphene and other Van der Waals 2D materials have been paid enormous attention due to its excellent properties in physics and chemistry and materials science. Two-dimensional transition metal disulfides (2D-TMDs) as promising potential application with low-power consuming and high performance, have already arisen much interests in the widely world. Due to the spin hall effect found in topological insulator, the topological insulator (TI) materials such as Bi_2Se_3, Bi_2Te_3 and NaBi have attracted much attention[1-3]. Meanwhile, the dynamic process of growth has become a hot topic since almost 10 years ago [3-5], but the earliest research about growth of topological insulator (TI) is in the 1999[6]. Comparing with transition metal selenide and tellurium films synthesized by molecular beam epitaxy (MBE) system 10 years ago, the transition metal disulfide materials such as MoS_2 were grown by MBE system until 2018[7]. Recently, the monolayer of transition metal selenide films has been proven that can be stable and large-scale by chemical vapor deposition (CVD) growth[8].

A two-dimensional (2D) material with few atoms thick is defined a free charge that is immovable in one spatial dimension and movable in the other two. This characteristic makes two-dimensional materials have new or superior functions, different from traditional bulk materials or films. Interest in two-dimensional films can be traced back to the late 1970s and early 1980s, when two-dimensional electron gas was formed in III-V semiconductors by molecular beam epitaxy (MBE).

In 2004, graphite was successfully peeled into two-dimensional graphene with atom-scale thin film, which aroused people's interest in two-dimensional materials[9]. Graphene has super light, flexible, high transmittance and faster electronic movement speed than other materials with higher thermal conductivity[10-12]. With the rapid

development of graphene research and the continuous innovation of material preparation technology, other materials with two-dimensional layered structure, such as transition metal disulfides (TMDC), have been gradually studied and applied. TMDC has many excellent properties, such as good mechanical flexibility and thermal stability, especially in the conversion of electrochemical energy storage, and has been widely used in optical and electrical devices.

Transition metal dichalcogenides (TMDC) are a group of layered materials with hexagonal structure and van der Waals bond. The molecular formula is MX_2 (M = Mo, W, Nb and other transition metals, x = S, Se, Te and other sulfur sources). TMDC materials exhibit strong in-plane bonding and weak out of plane bonding, which makes the materials split into two-dimensional single crystals with atomic thickness. [13-16].

1.1 Two-dimensional Materials

Two dimensional materials refer to materials in which electrons can only move freely (in plane) on two-dimensional nanoscale (1-100nm), such as nano film, superlattice and quantum well. The two-dimensional material was proposed along with the successful separation of graphene, a single-layer graphite material, by Geim group of Manchester University in 2004[9, 17]. Subsequently, some other two-dimensional materials were separated successively, such as boron nitride (hBN)[18], molybdenum disulfide (MoS_2)[16, 19], tungsten disulfide (WS_2)[20] and Mxene[21, 22]. Recently, it has been widely studied in the field of condensed matter physics. Since graphene won the Nobel Prize in physics in 2010, scientists and industry began to pursue graphene enthusiastically. Unlike bulk graphite, graphene has only one carbon atomic layer thickness. Honeycomb structure is the thinnest, lightest and strongest material known in the world, with excellent conductivity and thermal conductivity. Therefore, its application fields are very broad, such as flexible electronics, high-efficiency transistors, new sensors, new materials[12], batteries[14, 23], super capacitors[23], semiconductor manufacturing[24], new energy, communications, terahertz technology[25], aerospace energy technology, molecular electronics[25], etc.

Two-dimensional materials need to meet three basic conditions, grow in two-dimensional plane, have ordered structure, and are ultrathin in three-dimensional.

Graphene is defined as a monoatomic layer. In fact, the performance of mono-atomic layers in some applications is not the best, sometimes 2-3 or about 5 layers of multilayered graphene have the best performance. As a result, most scientists do not strictly define the thickness of two-dimensional materials, but more importantly, they define it in terms of performance differences from bulk materials.

The discovery of graphene exhibits how novel physical properties emerge when a bulk crystal of macroscopic dimensions is exfoliated down to one atomic layer. Like graphite, TMDCs bulk crystals are formed of monolayers bound to each other by van der waals integration[26].

In addition to graphene, scientists have developed five families of two-dimensional materials: MXenes, Xenes, Organic materials, TMDC (transition metal dichalcogenides) and Nitrides. Besides, in recent researches, two-dimensional transition metal halides are also one of the hot spots[27].

TMDCs monolayers such as MoS_2, WS_2, $MoSe_2$, $MoTe_2$, have a direct band gap, and can be used as future transistors and optical emitters and detectors[15, 28-30]. The TMDCs monolayer crystal structure has no inversion center, which lead to a new research field of physics: valleytronics[31]. The monolayers of TMDCs have been observed the spin splitting at valence band and conduction band which are hundreds of meV and few meV respectively. Strong spin-orbital coupling was proven to take the responsibility of these band splitting. Some three-dimensional semiconductor materials have dangling bonds on their surfaces, and many electrons are bound. Such as bulk GaAs and Si substrate, every topset layer atoms have one dangling bond because that the topset cubic lattices were cleaved by surface. The topset Ga atoms in GaAs (111) A and As atoms in GaAs (111) B have dangling bonds. Two-dimensional semiconductor materials have atomic-level smoothness, allowing electrons to move more freely. This enables them to have excellent electrical performance in extremely thin thickness.

1.2 Transition Metal Dichalcogenides Materials (TMDCs)

Since Geim and Novoselov et al. successfully exfoliated monolayer graphite by micromechanical exfoliation in 2004[17], two-dimensional materials have become the focus of attention in the scientific community. However, as it is a zero band gap material[14], this limits the application of graphene in optics and optoelectronics. Other two-dimensional materials like graphene, such as transition metal sulfides, have attracted much attention due to their unique optical, electrical, electrochemical and other properties, and become another hot spot in materials technology[13, 28, 32-35]. Two-dimensional (2D) transition metal dichalcogenide (TMDC), a sandwich-like structure MX_2 (M represents transition metals in the periodic table of elements, X represents S Se), and similar to graphene, TMDCs interlayer also grow through van der Waals force interlayer. Therefore, monolayer or multilayer TMDs can be peeled off from bulk materials. TMDCs have a variety of physical properties, such as: they can be used as insulator materials (e g, HfS_2), semiconductors (e.g. MoS_2 and WS_2), metals (e.g. TiS_2, VS_2 and $NbSe_2$)[8, 12, 14, 15, 20, 27, 36-38]. Furthermore, the band gap of semiconductor materials depends on the number of layers of TMDCs[24]. For example, the band gap of molybdenum disulfide can be increased from 1.2 eV (bulk material) to 1.8-1.9 eV (single layer)[39, 40]. Most TMD materials have three kinds of phase characteristics: the triangle (1T), the hexagon (2H) and the 3R. These three phases are not fixed and can be transformed into each other under certain conditions, Molybdenum disulfide generally exists in the form of semiconductor phase (2H), but it can be converted into metastable metal phase (1T) when electron transition occurs.

In recent years, nanomaterials based on TMDC have been widely used in integrated circuits for electrochemical energy storage and conversion, mainly because of the advantages of TMDC. The ultra-thin structure of the TMDC material can confine the carrier to 1 nm space at the interface, which can effectively suppress the short channel effect of the transistor, thus reducing the loss of the device, achieving a MoS_2 field effect transistor (FET) with a gate length of 1 nm and a switch ratio of 10^6[41].

Even there are many studies on 2D materials whatever monolayer or bulk phase, some new materials and properties are found ceaselessly. CoS_2, one of the subjects of our study, has a lot of controversy so far. Some researchers believed that CoS_2 has many phases such as 2D pentagonal structure, but most researches indicated that CoS_2 is one of pyrite structure[42-47]. In those papers, bulk cubic CoS2 is magnetic and metallic; 2D pentagonal structure is antiferromagnetic semiconductor. In this paper, the growth methods by MBE system for TMDC materials will be discussed, especially for the growth of transition metal disulfides.

1.3 Growth methods for two-dimensional materials

So far, there have been many insightful comments on the preparation of TMDC materials. Because 2D materials do not require lattice matching, a wide range of material combinations become possible[25]. Generally, the preparation methods can be summarized as chemical vapor deposition (CVD), molecular beam epitaxy growth (MBE), hydrothermal (Solvo) Synthesis, electrospinning, mechanical exfoliation (peeling), chemical vapor transition (CVT)[48], Sol-Gel method, etc. in this section, some of growth methods of TMDCs will be introduced.

Chemical vapor deposition (CVD) is the most widely used and mature technology for the deposition of various TMDC materials. Its principle is to introduce two or more gaseous raw materials into a reaction chamber, and then they react with each other to form a new material, which is deposited on the wafer surface. For precise control of parameters, TMDC materials with single layer, single heterojunction and multi heterojunction can be grown by CVD[8, 26, 49-51]. However, due to most TMDCs can react with O_2 and H_2O, it is difficult to grow large area single-layer TMDC films by CVD. The atmosphere of CVD system is not as low as MBE system; therefore, the grown samples have many crystal orientations[8].

The peeling method mainly uses polymer-assisted peeling to obtain TMDC material from bulk materials. This method can obtain high-quality, single-layer TMDC material. In peeling method, it can be divided into intercalation peeling method, mechanical peeling method and liquid peeling method[23, 52, 53]. Interlayer peeling method is to insert ions, small molecules or organic molecules into layers and to peel them by ultrasound. This makes it easier to obtain a single two-dimensional material[54]. Mechanical peeling separates nano-layers from layered crystals mainly by applying mechanical forces (friction, pull, etc.) between layers of layered compounds and van der Waals. A few or even single layers of two-dimensional transition metal sulfide materials are obtained by tearing them apart on layered TMDC block materials using viscous alternating adhesion[55, 56]. The liquid phase stripping method is mainly

through the interaction between the solvent and TMDC material, under the replication of ultrasonic wave, the solvent molecules enter into the interlayer to have an effect[57]. To overcome the van der Waals force in the TMDC material and realize the layer-by-layer stripping, the target material is obtained. The key of the liquid phase stripping technology is the surface tension between the solvent and the TMDC bulk material. When the surface of the solvent and the material match, then the interaction between materials can balance and satisfy the energy needed for TMDC stripping[52].

The growth of MEB in transition metal selenides and tellurides has been successfully demonstrated many times[3, 4, 6, 15, 29, 30, 36, 58-63]. Recently, traditional MBE growth methods have made important progress in the growth of transition metal disulfides. Because of the low sublimation point of sulfur powder, the choice of sulfur source is important to grow MS_2 (M= transition metal) films. In previous study, FeS_2 as an S source successfully provided a sulfur environment for molybdenum disulfide growth[7].

1.4 Antiferromagnetic Property

Antiferromagnets have very small positive susceptibility at any temperature, but their susceptibility varies with temperature. Louis Néel and other researchers, in a series of papers that began in 1932, he developed the theory of antiferromagnetism by applying the Weiss molecular field theory to antiferromagnetism[64].

In antiferromagnetic materials, the magnetic moment of an atom or molecule, usually related to the spin of an electron, is arranged regularly with adjacent spins and points in the opposite direction. Like ferromagnetism and antiferromagnetism, it is a manifestation of ordered magnetism. Generally speaking, the antiferromagnetic order may exist at a sufficiently low temperature, but disappear at or above Neel temperature, which is named after Louis Néel, who first discovered this type of magnetic order. Above the Neel temperature, the material is usually paramagnetic. When there is no external magnetic field, the antiferromagnetic structure corresponds to a total magnetization that disappears. In an external magnetic field, the antiferromagnetic phase may exhibit a kind of ferromagnetic behavior, in which the absolute value of the magnetization of one sublattice is different from that of the other sublattice, resulting in non-zero net magnetization. Although the net magnetization should be zero at absolute zero, the spin tilt effect usually results in a small net magnetization[65].

The variation of antiferromagnetic susceptibility with temperature is shown in Fig 1.1[66]. As the temperature decreases, the χ increases but reaches its maximum at the critical temperature T_N, known as Neel temperature. The substance is paramagnetic above T_N and antiferromagnetic below it. T_N is usually much lower than room temperature, which means it may be necessary to lower the susceptibility measurements to a fairly low temperature in order to discover whether a given substance paramagnetic at room temperature has antiferromagnetism at some lower temperatures. Most, but not all, antiferromagnetism are ionic compound-oxides, sulphides, chlorides, and the like- and a very large number are known, which makes them much more common than ferromagnetism.

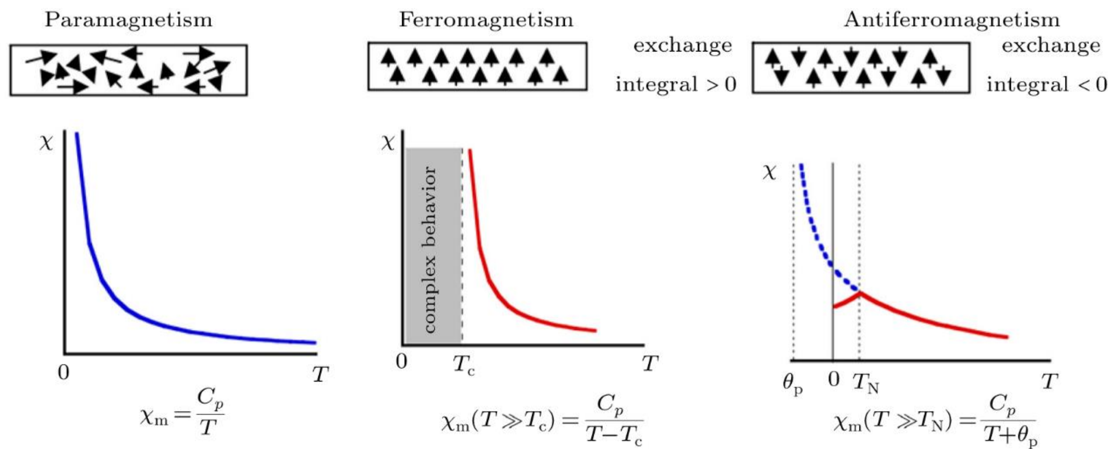

Fig 1.1 temperature-dependence susceptibility χ for para-, ferro-, and antiferromagnetic material[67].

Film Growth Theory

Like bulk materials, the phase equilibria of thin films depend on the thermodynamic functions under the corresponding conditions. It is necessary to explain some processes between grown atoms and substrate surface through the concept of interface phase. Through the concept of interface phase, the feasibility of the way and method of this project is discussed. The driving force of nucleation and growth comes from the fact that the free energy of solid phase is lower than that of gas phase. The higher the supersaturation of gas phase is, the more significant the decrease of free energy μ is.

2.1 The Process of Film Nucleation

Basically, under the vacuum environment of film growth, the atoms from vapor deposition to substrate will gather together on the substrate and grow up. Heterogeneous epitaxial growth is generally heterogeneous nucleation on existing substrates, such as Fe/GaAs, Co/GaAs, Bi_2Se_3/GaAs and system of this project CoS_2/GaAs PtS_2/GaAs. The nuclei on the substrate form a ball corona. The radius of curvature of the spherical surface is r, the wetting angle between the spherical surface and the substrate is θ, and the height of the spherical corona (h) is $r(1-\cos\theta)$.

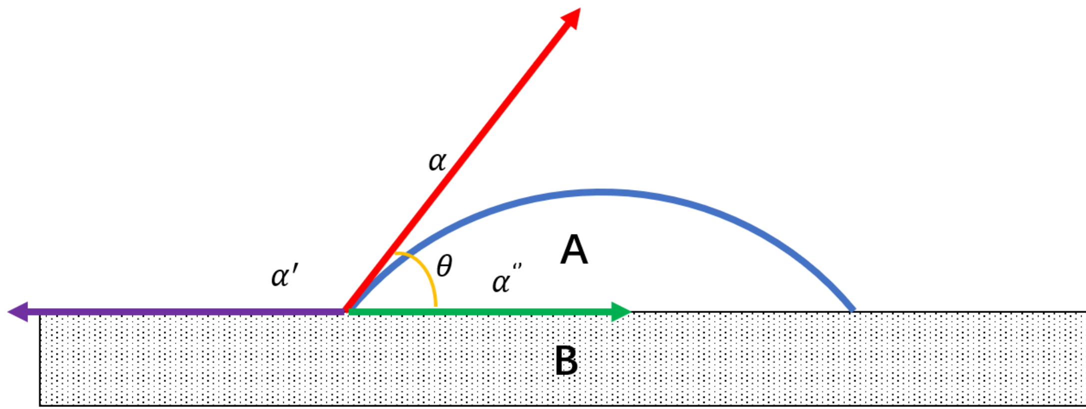

Fig 2.1 Spherical corona like crystal nuclei on substrate.

In the Fig 2.1, α is the surface tension of the spherical coronary crystal nuclei (A), α' is the surface tension of the substrate (B), and α'' is the interface tension between the crystal nuclei and the substrate. When the surface tension and the interfacial tension balance, there is the following mathematical relation

$$\alpha\cos\theta = \alpha' - \alpha'' \quad (1)$$

The wet angle θ determines the radius of curvature r and the ratio of corona height (h) / radius (r). The smaller θ is, the flatter corona is. When fully wetted, the corona becomes a single atomic layer covering the substrate, and the wet angle is $\theta = 0$, $\cos\theta = 1$.

For GaAs substrate, the adsorption free energy α_s is the free energy obtained by the adhesion of the unit area crystal and substrate, that is

$$\alpha_s = \frac{u_{AB}}{a^2} \tag{2}$$

Where u_{AB} is bond energy between A and B atoms, and a is lattice parameter. α_s also has relationship with crystal surface energy, substrate surface energy and interfacial energy, which is

$$\alpha_s = \alpha + \alpha'' - \alpha' \tag{3}$$

According to the above formula, adsorption free energy plays an important role in the height of crystal nucleus and wetting angle. Therefore, it can be concluded that reducing the surface chemical energy can reduce the wetting angle and improve the film quality. From (3), the formula can be obtained

$$\alpha\, cos\, \theta = \alpha - \alpha_s \tag{4}$$

It can be seen from formula (4) that the smaller the value of α_s is, the larger the value of $\cos\theta$ is, and the smaller the wettrfgva fngle value of θ is. Because symmetry broken of GaAs substrate, high bond energy will result in low adsorption free energy. In this project, sulfur passivation is an effective way to combine S atoms and topset As atoms resulting in reducing the adsorption free energy α_s. According to formula (4), to reduce α_s, the wet angle θ will be smaller. However, like surface relaxation, researchers can provide qualitative analysis reduced α_s rather than qualitative analysis.

2.2 Concept of Interface Phase and its Application in Sulfide Passivation on GaAs (111)

Like bulk materials, the phase equilibrium of films is determined by the thermodynamic function under the corresponding conditions, so the phase diagram obtained in bulk materials can guide the appearance of equilibrium phases in films. Generally, the growth process of thin films is that atoms in gas phase are deposited on solid substrate, which occurs at the interface of two phases (gas and solid). According to the law of thermodynamics, the interface phase can be formed between two phases. However, there are also differences between the interface phase and the bulk phase. As shown in Fig.2, there are very small density change areas (blue part) between the solid phase and the liquid phase after that. The range of rapid density change can be defined as the interface phase. However, this definition is arbitrary, because it is difficult to define precisely when the density changes rapidly.

The interface phase is basically defined as an infinitely thin plane, so PV in Gibbs function is zero. If the system is partitioned as shown in Fig. 2.2, its total mass is M.

$$M = M_S + M_L + M_I \tag{5}$$

Where M_S, M_L, M_I are mass of solid, liquid and interface respectively. The differential of the internal energy of a system can be written as

$$dU = dU_s + dU_L + dU_I = TdS - PdV + \gamma dA \tag{6}$$

Because the quality of interface phase can be regarded as zero, the internal energy differential of solid phase, liquid phase and interface phase is

$$dU_s = TdS_s - PdV_s \tag{7}$$

$$dU_L = TdS_L - PdV_L \tag{8}$$

$$dU_I = TdS_I + \gamma dA \tag{9}$$

Where γdA is the increase of internal energy caused by the increase of interfacial area

A caused by interfacial tension γ. The sign of γdA is opposite to that of PdV, because the work done when the volume V of the bulk phase is reduced by the external pressure P increases the internal energy of the bulk phase.

The increment d_U of internal energy of the system is equal to the sum of the heat Td_s obtained by the system and the work Pd_V of the external system. TdS_s, TdS_L, TdS_I are the differential of heat over entropy of solid liquid and interface.

According to the thermodynamic calculation, the change of free energy caused by external work on the boundary phase is

$$dF_I = dW = \gamma dA \tag{10}$$

Where F_I is free energy of interface phase and W is external work. By formula (10), we can get that interfacial tension is the free energy of unit area interface:

$$F_I = \gamma A \tag{11}$$

It can be seen that the interfacial tension is the free energy of the interface per unit area. The volume of the interface phase is zero, and PV does not appear in the Gibbs free energy G of the interface phase, so for the interface phase, the free energy and Gibbs free energy are equal.

The interface energy can be calculated by the relationship between internal energy and free energy after partial derivative treatment of the free energy of the interface phase:

$$\alpha = \frac{U_I}{A} = \gamma - T\frac{d\gamma}{dT} \tag{12}$$

Through this important formula, we know that the interface energy α is the internal energy of the unit area interface, and the interface tension γ is the free energy of the unit area. When $T = 0\ K$, the interfacial energy is equal to the interfacial tension. The energy in the interface is generally greater than the interface tension, $\alpha > \gamma$.

By calculating the system of unitary element, we can similarly define the interface phase of a binary system. For binary system, the first element is used to define the CD position of the interface shown in Fig.2.2, meanwhile the chemical potential energy of the second element needs to be considered. In binary system, the effect of the growth of the second element on the interface phase is

$$d\gamma = -\frac{M_{2I}}{A} d\mu_2 \quad (13)$$

where μ_2 is chemical potential of the second element and M_{2I} is the amount of growth of the second element. Through the important formula of (9), we can infer the influence of the growth of binary system on the interface. The amount of the second element in the interfacial phase can change the interfacial tension. At a constant T and P, the mass concentration ($\frac{M_{2I}}{A}$) of the two elements in the binary system is equal to the negative value of the derivative of the interfacial tension to the chemical potential of the binary elements. It shows that the atoms soluble on the surface or at the interface are segregation phenomenon for the alloy. For the growth of semiconductor, the surface will be uneven and difficult to nucleate.

Surfactant, which plays an important role in the growth of thin films, is an element that can be segregated on the surface. It can significantly change the surface energy (or surface tension), improve the wettability of the substrate when the film nucleates, and significantly reduce the surface roughness of the film.

In this research project, the sulfur deposited on the surface of GaAs by passivation plays the role of surfactant. When the transition metal grows, the sulfur surface can significantly improve the growth process. At the same time, because the sulfur element is passivated to the surface of the sample. When there are defects on the surface, after passivation, there will be a single layer of bonded sulfur atoms on the surface to form surfactant, which can remarkable change the surface tension. Therefore it can also overcome the defects of the film during nucleation. The growth principle of two-dimensional binary semiconductor is similar to that of single metal MBE. This method greatly reduces the difficulty and uncertainty of growth, and also improves the film quality of two-dimensional single-layer TMDC.

The translational symmetry or surface periodicity of the crystal should continue to infinity. The appearance of the surface means the periodic interruption, so the surface is also a kind of crystal defect. The additional energy caused by surface is very high, especially for strongly bonded crystals. Therefore, the method of sulfur-passivation can form a layer of sulfur on the surface of GaAs.

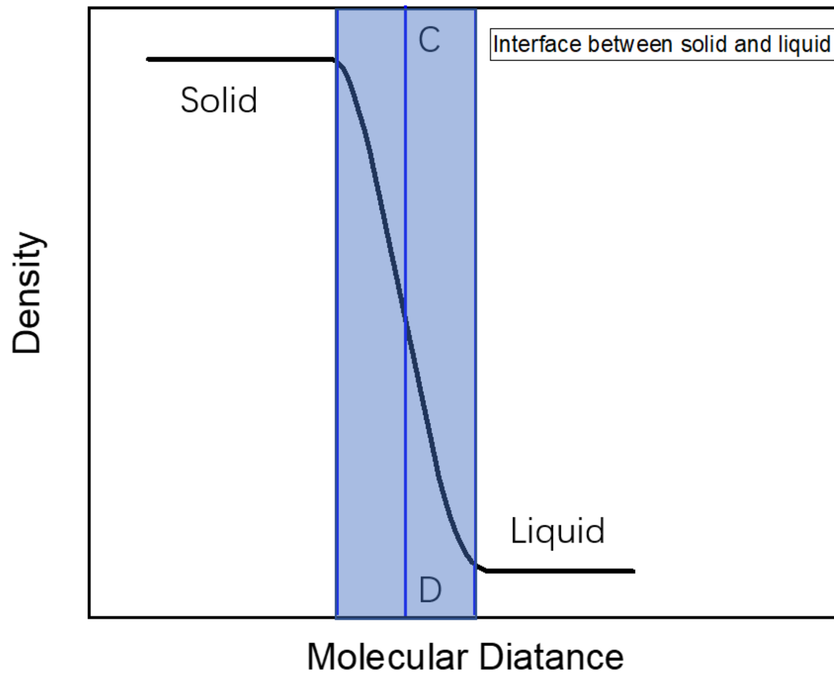

Fig 2.2 Interface phase between solid and liquid

2.3 Homoepitaxy and Heteroepitaxy

In the different growth modes of homogenous and out heterogenous epitaxy, bond energy u_{AA} (A: atoms of substrate) is the crucial factor to determine the film quality. The epitaxial film of A atoms on A substrate is called homogenous epitaxy. On the contrary, the epitaxial film of B atom on A substrate is called heterogenous epitaxy. In the case of homogenous epitaxy, A clusters on A substrate can have many configurations. When the temperature is high and the atoms are easy to migrate, many configurations tend to a most stable configuration.

In the case of cubic crystals, if there are four deposited atoms, they can be form in a

row or in a square. The former forms seven AA atomic bonds (four bonds with the substrate and three bonds between the deposited atoms), the latter forms eight atomic bonds (four bonds with the substrate and four bonds between the deposited atoms), reducing the energy by $7u_{AA}$ and $8u_{AA}$ respectively. Therefore, the square configuration of the four atoms is the most stable for heterogenous epitaxy. Based on the conclusion that the formation of tetragonal structure by homogenous epitaxy reduces the maximum energy, we can analyze the growth mode of thin film in homogenous epitaxy. When there are eight atoms deposited on substrate, they may form a close-packed double-layer square or a single-layer film. At this time, the bond energy of atoms is reduced by $16u$ and $18u$ respectively. Table 1 shows the minimum energy values of single layer and double layer packing under different number of deposited atoms (N). Therefore, the most stable growth mode of homoepitaxy is monolayer growth rather than island multilayer growth.

N	8	18	32	72	98
Monolayer	$-18u_{AA}$	$-45u_{AA}$	$-84u_{AA}$	$-199u_{AA}$	$-274u_{AA}$
Bilayer	$-16u_{AA}$	$-42u_{AA}$	$-80u_{AA}$	$-192u_{AA}$	$-266u_{AA}$

Table. 1 The lowest energy value of closed packed monolayer and bilayers of homogenous epitaxy.

Compared with homoepitaxy, the situation of heteroepitaxy is more complicated. In terms of energy. Heteroepitaxy can grow layer by layer or island, which depends on the AB (A: deposited atoms; B: substrate) bond energy and AA bond energy. If the AB bond energy is greater than the AA bond energy, the layer-by-layer growth is favorable; otherwise, if the AA bond energy is significantly greater than the AB bond energy, it tends to island growth. Take the deposition of A atom on the cubic crystal B (100) as an example. If there are 8 A atoms packed in two layers, the energy will be reduced by $-4u_{AB} - 12u_{AA}$; if they are packed in one layer, the energy will be reduced by $-8u_{AB} - 10u_{AA}$. Table.2 reveals the lowest energy value of closed packed monolayer and bilayers of heterogenous epitaxy. It can be seen from table 2 that the number of

assembly bonds is less than that of single-layer close pack in case of double-layer close pack. With the number of atomic depositions from 8 to 98, the favorable condition for double-layer packing is: $u_{AA} > 2u_{AB}$ (N=8); $u_{AA} > 1.5u_{AB}$ (N=18); $u_{AA} > 1.33u_{AB}$(N=-32); $u_{AA} > 1.24u_{AB}$(N=72); $u_{AA} > 1.2u_{AB}$(N=98). With the increase of the number of particles N, the favorable condition of double (Island) layer will be further reduced.

N	8	18	32	72	98
Monolayer	$-8u_{AB}$ $-10u_{AA}$	$-18u_{AB}$ $-27u_{AA}$	$-32u_{AB}$ $-52u_{AA}$	$-72u_{AB}$ $-127u_{AA}$	$-98u_{AB}$ $-176u_{AA}$
Bilayer	$-4u_{AB}$ $-12u_{AA}$	$-9u_{AB}$ $-33u_{AA}$	$-16u_{AB}$ $-64u_{AA}$	$-36u_{AB}$ $-156u_{AA}$	$-49u_{AB}$ $-217u_{AA}$

Table. 2 The lowest energy value of closed packed monolayer and bilayers of heterogenous epitaxy.

In order to pursue high-quality single-layer two-dimensional growth, AB bond energy should be greater than or equal to AA bond energy, which is called complete wetting. Therefore, in order to improve the quality of transition metal disulfide single-layer films, a new growth mode is explored from the perspective of chemical energy, and a more suitable growth method is found. By passivating sulfur on GaAs substrate and heating the substrate, higher substrate chemical bond energy can be achieved. Unlike previous film growth concepts, we no longer only pursue the reduction of the chemical potential energy of the substrate. During the growth process, the lowest possible reduction of the chemical potential energy of the whole system will be our goal. In previous studies, similar researches have done on the growth of transition metal selenides. Better quality films can be obtained by passivation of selenium on GaAs substrate and growth of transition metal selenides[58, 68, 69]. Similarly, there are some studies on the growth of transition metal selenides using sulfur passivation. These studies show that the sulfur atoms on the surface of GaAs can promote the film quality of transition metal selenides grown by MBE to be better[68].

Because we need smaller, more efficient electronic devices, and transition metal sulfide 2-D materials need to form large-area film like silicon in industrial production, we need a lot of improvement when growing in ultra-high vacuum. However, at this stage, the growth of transition metal sulfides is not able to prepare large-area monoatomic layers, which makes it difficult for subsequent device research[70]. The specific process will be described in detail in later chapters.

Theory Background and Literature Review

In this chapter, the background theory of this project and its relevant experiments will be discussed. The researches of sulfur-passivation GaAs will be reviewed, which will be discussed deeply in the thesis. Then a brief on the studies about growth of two-dimension materials will document in this chapter. Finally, the properties of some 2D materials will be introduced such as magnetic and electronic properties.

3.1 Sulfur-passivation GaAs

Gallium arsenide has many very superior semiconductor characteristics. Its electron mobility is 5 times larger than silicon, and it is also a direct gap semiconductor. It has obvious advantages over silicon in manufacturing ultra-high-speed devices and optoelectronic devices. Although the research on gallium arsenide has a history of nearly 50 years, its potential has not been fully exploited to make it play a leading role in the application of semiconductor devices. For a long time, the dominant position of silicon devices has been unshakable. There are many reasons for this situation, mainly in terms of technology, including the integrity of materials, difficulties in preparing large single crystals, high cost and complex device preparation technology. Among them, the surface passivation technology of GaAs is a problem that has not been solved completely.

For silicon devices, SiO_2 is a very ideal passivation film, which can be formed by the surface oxidation of silicon, so it is called self-oxidation layer. The Si/SiO_2 interface has very low density of states and good chemical stability. It can be used as a passivation film for silicon devices and as a metal oxide half conductor (MOS) FET. In the 1960s and 1970s, great efforts were devoted to the study of the autoxides of GaAs. It was found that, on the other hand, the arsenic oxide is unstable, and the following reactions will take place between it and GaAs:

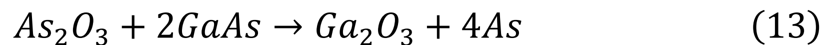

$$As_2O_3 + 2GaAs \rightarrow Ga_2O_3 + 4As \tag{13}$$

Therefore, since the 1980s, people have realized that it is not feasible to passivate compound semiconductors with self-oxide layer, and it is necessary to find passivation layer made of other materials.

For silicon devices, the formation of SiO_2 layer on the Si substrate is the essential for metal-insulator-semiconductor devices having low density of interface states. On the contrary, as the second generation of semiconductor, the oxide native GaAs does not exhibit passivating properties similar to those of silicon oxide, which obstruct the

performance and reliability of GaAs-based devices[71, 72]. The passivation of GaAs is key technical method in development of GaAs performance. The passivated GaAs surface have been researched for more than 30 years, which the earliest study can be traced to 1977[73]. The sulfide passivation on GaAs become a hot topic from the 1980s'[74-78]. In the beginning of studies of sulfur passivation, Na_2S was employed to deposit S atoms onto GaAs surface[72, 73]. The following studies of sulfide passivation, $(NH_4)_2S$ and $(NH_4)_2S_2$ treatment have also been found to improve the properties of metal-insulator-semiconductor characteristics significantly[78-80]. Those observations reveal that the interface state density is efficiently reduced by various sulfuric solution treatments, which the controllable Schottky-barrier heights are achieved by $(NH_4)_2S_x$-treated GaAs (001) surface[78]. Even though many investigation[76, 77, 81-83], in spite of lack direct evidence in atomic size demonstration, the nature of S-GaAs bonds on the sulfide-treated GaAs surface is still controversial. Some studies reported that As-S bonds are most strong among all S bonds[76]. However, some other groups believed that the strongest Ga-S bonds and weak As-S bonds[77, 79, 84].

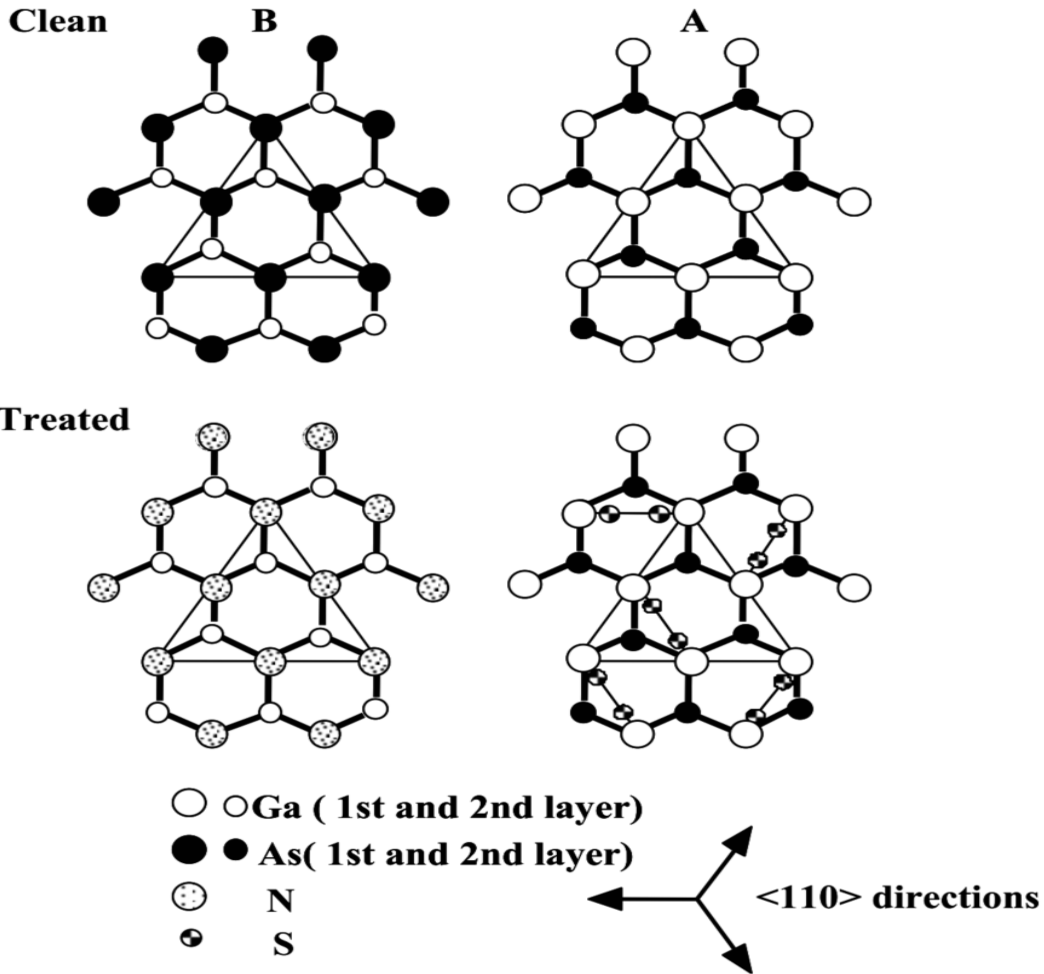

Fig 3.1 the top panel shows the atomic configurations of clean (111) A and (111) B surfaces, while the bottom panel describes the model that interprets the experimental data after treatment and annealing, corresponding to nitrogen adsorption at the B surface and to adsorption of sulfur on the A one. It is proposed that sulfur atoms on the A surface are dimerized[85].

The initial motivation of S passivation is to seek the mean that form the structure of metal-insulator- semiconductor, hence, the researches of S-passivation GaAs (111) are not as much as GaAs (100). One of the representative researches[85], the hydrazine-sulfide solution (N_2H_2 and Na_2S solution) is utilized to treat the GaAs (111) B and GaAs (111) A surfaces. The results of treatment indicate the as-treated GaAs (111) B surface is covered by both N and S atoms but only S atoms on the GaAs (111) A surface, as seen in Fig.3.1. The Auger spectra present the sulfur element is probed on the GaAs (111) B after post annealing with over 500℃ to remove physiosorbed overlayer,

however, the sites of S atoms cannot be provided in the research. By the wet-treatment GaAs (111) B, single monolayer GaN can be achieved on the GaAs surface. If the increase the time of passivation, there is not only chemisorption but physisorption which the effective thickness is around 0.6nm.

Another report discussed the possible sites of S atoms on the GaAs (111) b surface after passivation. The adsorption energies of S atoms are various between the total energy at the optimal position and that of the faraway position. In the exchange site, the S atoms established single bond with three neighboring atoms to form a three-fold coordination where S atoms replace either the outermost Ga atoms (or As atoms) of the GaAs (111)Ga surface [or GaAs(1 1 1)As surface], or connect with the Ga (As) atoms on the surface to form the on-top configuration, as shown in Fig.3,2(a)[86]. However, their theory was not directly observed in experiment. According to Bringans et al[87], T.Ohno designed the configuration of S bonds to achieve the bond energy, bond length and band bending of Ga-S and As-S bonds. In this report, the surface monolayer of S atoms was considered to bond with the surface Ga atoms or As atoms. However, some other researchers believed the S atoms will replace the As atoms in the bulk.

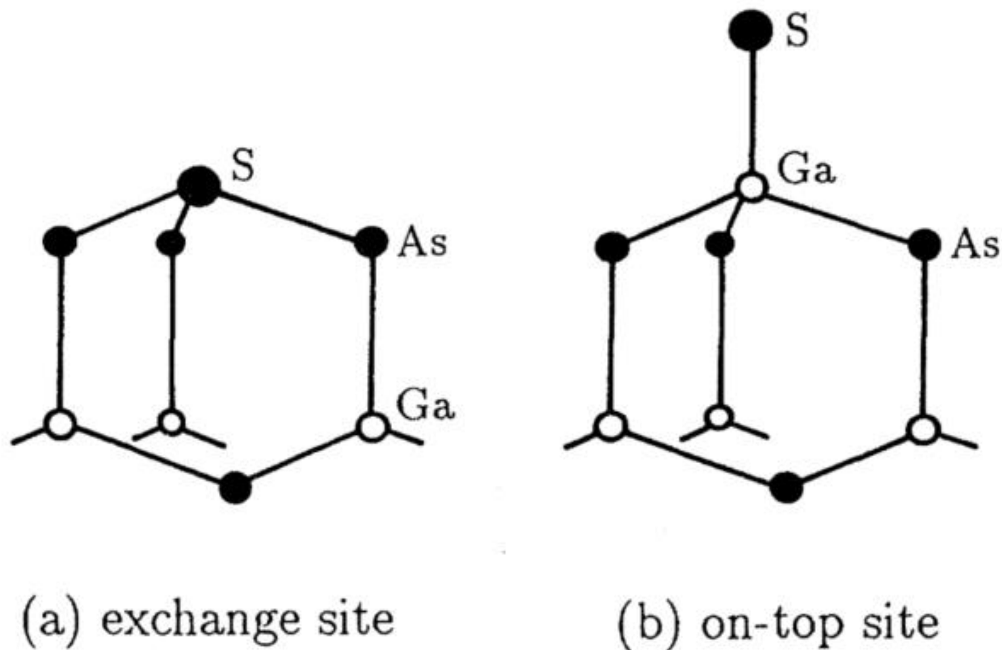

Fig 3.2 adsorption configurations of sulfur atoms on the GaAs(111)Ga surface: (a) the exchange site and (b) the on-top site[86]

In Fig.3.2 the example of passivated-GaAs (111) B configuration is considered to be same with GaAs (111) A. Therefore, the position of S atom in GaAs (111) B will be regarded as equivalent to GaAs (111) A.

Adsorption site	Bond	Length (Å)	Energy (eV)
	(111)Ga surface		
on-top (—As≡Ga—S)	Ga—S	2.11	4.02
exchange (—As≡S)	As—S	2.40	4.32
	$(\bar{1}\bar{1}\bar{1})$As surface		
on-top (—Ga≡As—S)	As—S	2.17	3.69
exchange (—Ga≡S)	Ga—S	2.41	6.07

Fig 3.3 the Ga-S bond and As-S bond length on the GaAs (111) Ga surface and GaAs (111) As surface with an adsorbed S monolayer in the top and exchange sites.[86]

In term of theoretical calculation, the adsorption energy of Ga-S bonds and As-S bonds are shown in the Fig.3.3. The Ga-S bonds are stronger than As-S bonds for both on-top and exchange sites. The Ga-S bond has also been found to be stronger than As-S bonds on the surface of GaAs (100). Moreover, the S atoms are more likely to occupy the exchange site for both GaAs (111) A and GaAs (111) B.

For the passivation of GaAs studies, the initio motivation is to establish the structure of metal-insulator-semiconductor leading to reduce the surface-state density of interface. Hence, the researchers do not have much interests in the studies of GaAs (111) B because the sulfide GaAs (111) B does not have reduction of surface-state density on the interface[86].

Even though the various types of S position were reasonedly discussed the report did not point out the exact sites of S atoms on the GaAs (111) A and B. The sulfide passivation includes many complicated reactions than the adsorption of S atoms[86]. The treated surfaces are not only synthesized the ordered S/GaAs monolayer, which

other researches are proven that Sb atoms can infiltrate the third layer GaAs (001)[88]. In 1995, a detailed research of S-passivation of GaAs (111)b introduced that S-As bonds are stronger than S-Ga bonds[84].

3.2 Two-dimension Materials Growth

Recently, many excellent works revealed indicated that various growth methods, such as chemical vapor deposition (CVD), molecular beam epitaxy (MBE), and other chemical methods, can achieve high-quality thin films[7, 8, 89-91].

Two-step methods was firstly applied in CVD growth in 2019[8], which can synthesize the high-quality, large-scale thin films. In Fig.3.4b, the 2D materials of transition metal selenide thin film could be synthesized full-coverage 2-inch wafer. The Fig.3.4c indicates the roughness and profiles of as-sputtered Nb, $NbSe_2$ and heat-treated $NbSe_2$ thin films. Fig.3.4d and 3.4e show the chemical binding energy and Raman spectra of $NbSe_2$. There is no obvious in changes of X-ray photoelectron spectroscopy (XPS) and Raman measurement, which the $NbSe_2$ thin film of two- step growth is stable in air.

The scanning transmission electron microscopy (STEM) measurement indicates that the CVD growth thin film has polycrystalline structure. The Fig.3.5b is zoomed-in image with misorientation of $\sim 25°C$. The boundary of 5-7 pairs can be detected. To detect individual lateral grain, a near-perfect lattice structure can be demonstrated across a $25nm \times 25nm$ area.

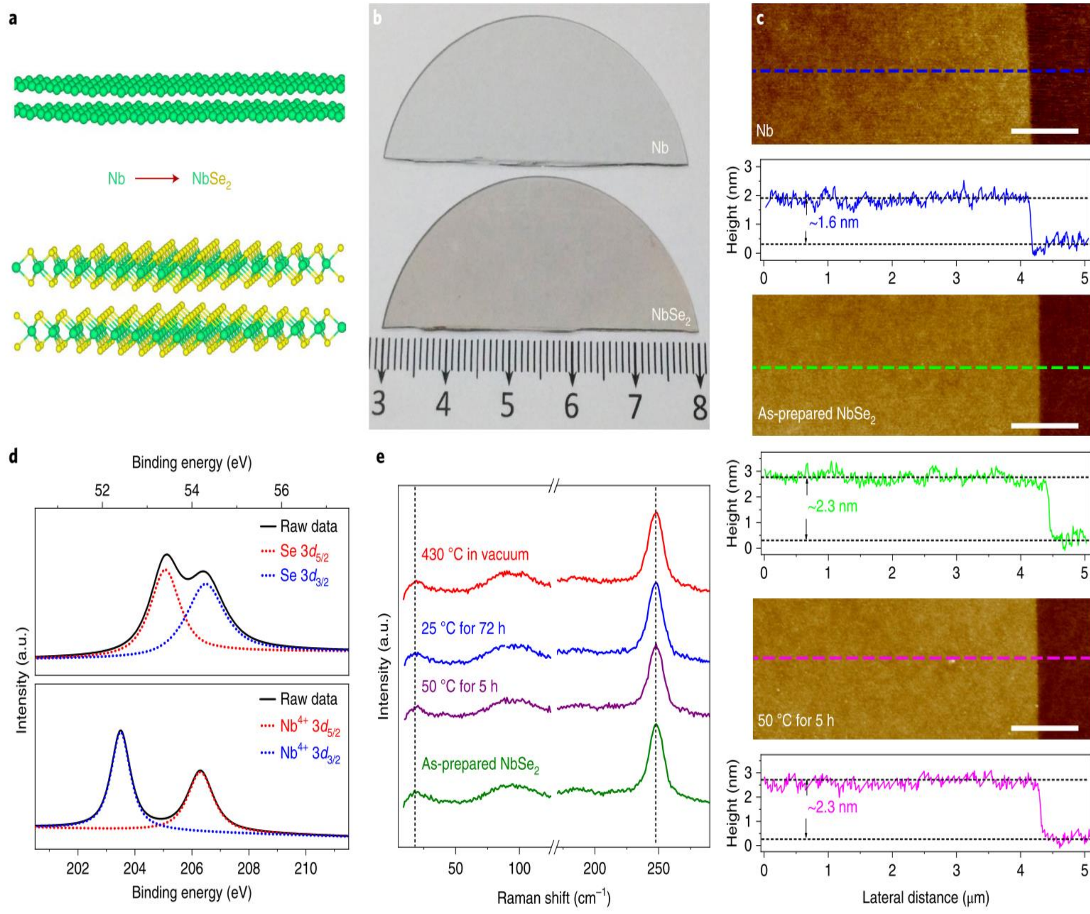

Fig 3.4 a, A schematic illustration of the structural transformation from the sputtered Nb film to a 2H-$NbSe_2$ film. b, A photograph of a Nb film and a selenized Nb film on the 2-inch double-side polished sapphire wafers, which are homogeneous and transparent. c, AFM images and the corresponding height profiles of an as-sputtered Nb film, a selenized ($NbSe_2$) film and a heat-treated (50 °C for 5h in air) $NbSe_2$ film. A height increase of ~50% is exhibited after selenization. Scale bars, 1 μm. d, XPS spectra of Nb 3d and Se 3d from a selenized Nb film (0.7 nm in thickness) after long-time exposure to air. e, Raman spectra with perpendicular polarization for the $NbSe_2$ films after different treatments[8].

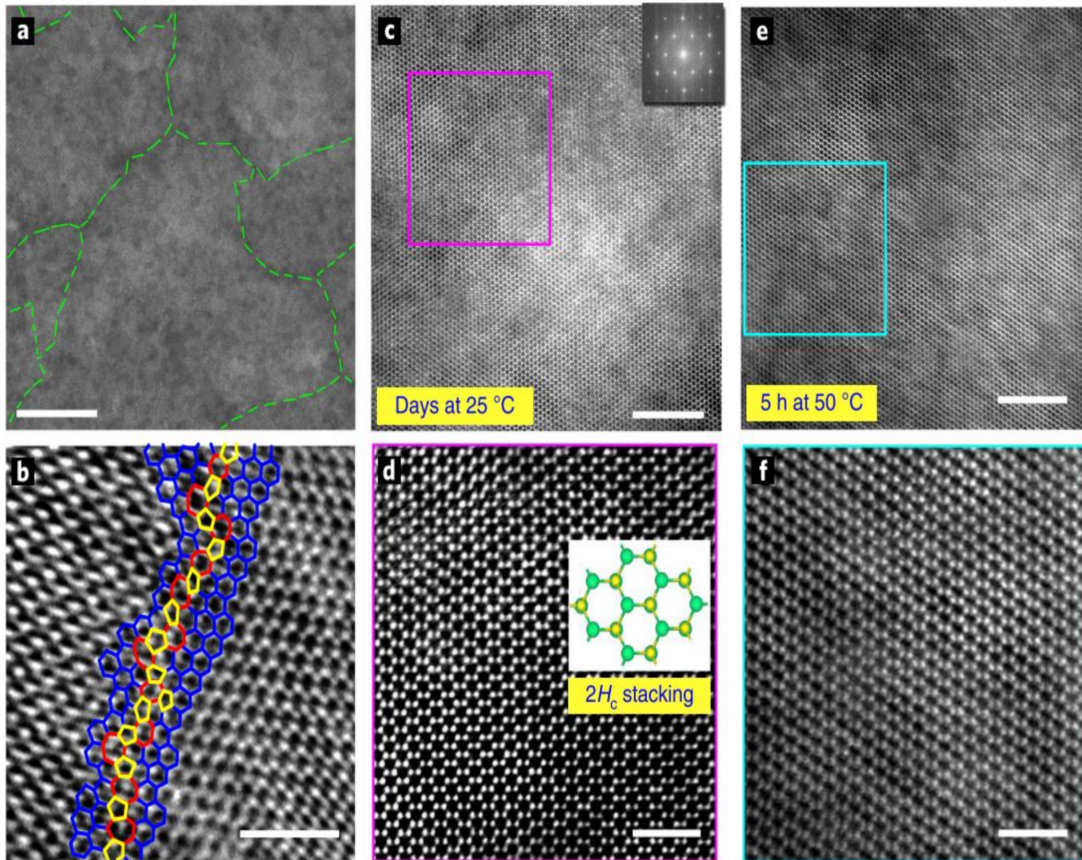

Fig 3.5 a, A low-magnification STEM image showing the polycrystalline structure of a $NbSe_2$ film; the grain boundaries are marked by green dashed lines. b, The atomic structure of a tilt grain boundary with a misorientation of ~25°, where the pentagon (yellow), heptagon (red) and hexagon (blue) structures in the grain boundary region are marked out accordingly. Only 5–7 pairs exist. c, The lattice structure in a single-crystalline grain, showing a perfect single-crystalline structure (as confirmed by the inset fast Fourier transform pattern), where no obvious atomic defect is detected even after exposure to air for several days. d, Atomic structure image of the area marked out by a purple square in c, with the inset showing the atomic model of $NbSe_2$ (top view) with 2Hc structure. e,f, STEM images at different magnifications showing the atomic structure of the NbSe2 film after heat treatment at 50 °C for 5 h in air, where no obvious atomic vacancy is observed. Scale bars, 20 nm (a), 2 nm (b,d,f), 5 nm (c,e).[8]

3.3 The Growth of 2D Transition Metal Chalcogenide Materials by Passivated GaAs

By using passivation to synthesize 2D materials can be trace to 1994[58]. Even lattice matching is difficulty that lead to barrier of combination of constituent materials, the mismatching is overcome in van der Waals epitaxial (VDWE)[69, 92]. The surface dangling bonds can be terminated by using S or Se atoms in GaAs (111) B much easier than in any other materials that are very flat. Until heating the substrate up to 580℃ under the Se circumstance, the spotty RHEED pattern originated from the streak of GaAs (111) pattern. Decreasing to 500℃ of substrate or less under the continuous irradiation of the Se beam, the dangling bonds were terminated with Se atoms to form GaSe quasi-van der waals substrate surface as shown in Fig.3.6. High-quality $NbSe_2$ films as thick as 100nm have been grown on the substrate of GaSe. Two-dimensional nucleation growth is classified into single nucleation growth and multinucleation growth, here multinucleation growth means that many nuclei are formed on the surface before the monolayer growth is completed. $NbSe_2$ films grown by the conventional method had many domains, and their size was estimated to be nanometer-size or less from the broadness of the reflection high energy electron diffraction (RHEED) streaks[7]. It should be noted that the film described here is not a so-called multidomain one but a pseudo-single crystalline one in the sense that crystal axes of all domains align to those of the substrate.

The method of generating quasi-van der waals substrate is the core to grow the transition metal disulfide materials. The recent studies have already refocused on this method[69]. Therefore, in case of overcoming the misfit with the substrates and generating large-scale thin films, the passivated GaAs (111) could provide a potential possibility of transition metal disulfide materials. Moreover, this method could be ubiquitous for all transition metal disulfide materials growth.

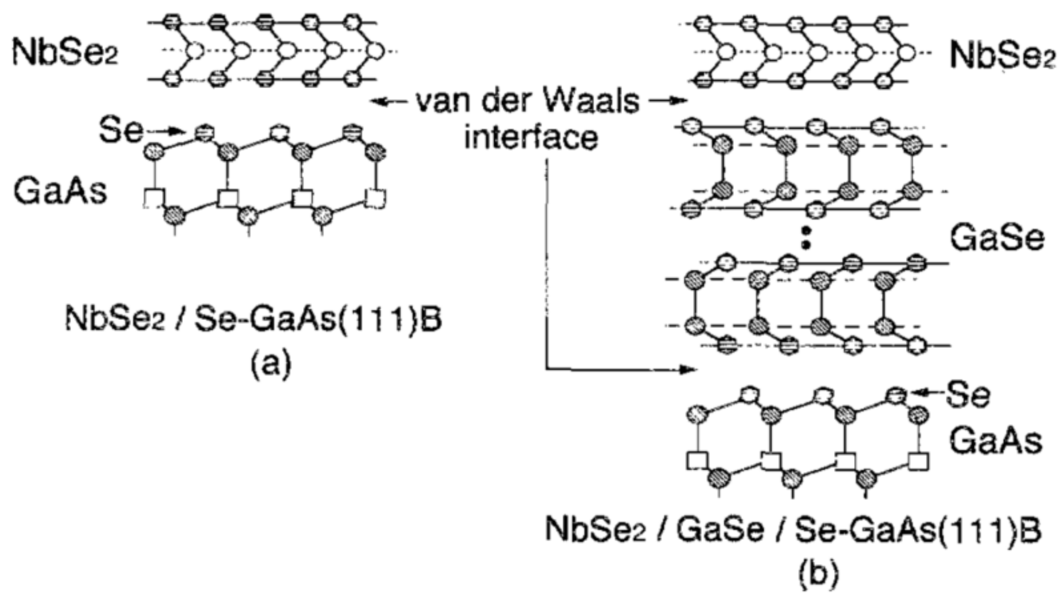

Fig 3.6 schematic diagrams of NbSe2 films on a van der Waals GaAs surface realized by the Se termination of surface dangling bonds (a), and by the growth of GaSe thin films on Se-GaAs (h).[58]

Experimental Techniques

A wide range of experimental techniques have been established and utilized to fabricate and detect the monolayer film of 2D materials for this project. Major facilities are provided by joint laboratory of York-Nanjing university. Some of experiments are supported by other laboratories' experimental techniques. Various experimental techniques which heavily involved in this project are introduced in this chapter. This chapter has four main sections: the first part is about the growth facilities; the second part introduces the substrate selections and cleanroom equipment; the reagents selections will be presented in the third part; the final is devoted by the characterization techniques;

4.1 Vacuum Film Growth

Vacuum film growth refers to a method of heating metal or non-metallic materials under high vacuum to evaporate and condense on the surface of plated parts (metal, semiconductor or insulator) to form a thin film. Vacuum coating is an important aspect in the field of vacuum application. It is a new technology based on vacuum technology, using physical or chemical methods, and absorbing a series of new technologies, such as electron beam, molecular beam, ion beam, plasma beam, radio frequency and magnetic control, to provide a new technology for scientific research and practical production.

Vacuum coating technology is generally divided into two categories: physical vapor deposition (PVD) and chemical vapor deposition (CVD).

Chemical vapor deposition (CVD) is a method to produce metal or compound films on the substrate by the chemical reaction on the surface of the substrate or the gas phase action.

Physical vapor deposition (PVD) technology refers to the method of directly depositing the source material on the surface of the substrate by using various physical methods to vaporize the material into atoms, molecules or dissociate it into ions under vacuum. Most of the thin films are prepared by physical vapor deposition, which uses some physical processes, such as the thermal evaporation of materials, or the sputtering of atoms on the surface of materials when bombarded by ions, to realize the controllable transfer process of material atoms from the source materials to the films. Physical vapor deposition technology has many advantages, such as good film / substrate bonding force, uniform and dense film, good film thickness controllability, wide application target, wide sputtering range, thick film deposition, alloy film with stable composition and good repeatability. MBE growth technology is one of the vacuum film growth technologies. The films have the characteristics of high precision and high quality.

4.2 Molecular Beam Epitaxy (MBE) Technique

4.2.1 Introduction

The development of UHV technology promotes the development of precision-controlled growth technologies, such as molecular beam epitaxy (MBE), pulsed laser deposition (PLD), etc. This breakthrough makes it possible to achieve highly controllable coherent epitaxial growth under non-equilibrium conditions. Compared with other growth methods, MBE has the advantage that it can guarantee the epitaxial layer growth of the sample by very slow growth rate, such as several atomic layer thickness per minute.

Molecular beam epitaxy (MBE) is a newly developed epitaxial coating method and a special vacuum coating process. Epitaxy is a new technique for the preparation of single crystal thin films. It is a method for the growth of thin films layer by layer along the crystal axis of the substrate material under suitable substrate and conditions. The advantages of this technology are: low substrate temperature, slow film growth rate, easy to control the beam intensity accurately, and the film composition and doping concentration can be rapidly adjusted with the change of the source. By using this technique, we have been able to prepare single crystal films as thin as dozens of atomic layers, as well as ultra-thin layer quantum microstructure materials formed by alternately growing films with different components and dopants.

MBE (molecular beam epitaxy) is a precious technique for growing high quality crystal films on crystal substrates. Under the condition of ultra-high vacuum, the vapor generated by heating the furnace with various required components is directly sprayed onto the single crystal substrate at a proper temperature by the molecular beam or atomic beam formed after collimation through a small hole. At the same time, controlling the molecular beam to scan the substrate, the molecules or atoms can be arranged in layers according to the crystal to form a film on the substrate. Molecular

beam epitaxy has many unique advantages, which make it a hot technology in materials, physics and other fields.

MBE growth rate is very slow, about 100 nm / hour, which is equivalent to a single atomic layer every 10 seconds. Therefore, it is conducive to achieve accurate control of thickness, structure and composition, and to form a steep heterostructure. In fact, MBE is an atomic level processing technology, which is the reason why MBE is particularly suitable for the growth of superlattice materials.

Due to low temperature of epitaxial growth, the lattice mismatch effect caused by thermal expansion on the interface and the self-doping diffusion effect of substrate impurities on the epitaxial layer are reduced.

Because the growth is carried out in the ultra-high vacuum, the substrate surface can be completely clean after treatment, and contamination can be avoided in the epitaxial process, so the epitaxial layer with excellent quality can be grown. In molecular beam epitaxy device, there are also instruments for detecting surface structure, composition and vacuum residual gas, which can monitor the integrity of composition and structure of epitaxial layer at any time, which is conducive to scientific research.

The traditional MBE is an ultra-high vacuum physical deposition process, which does not need to consider the intermediate chemical reaction, and is not affected by mass transfer. Moreover, the growth and interruption can be controlled instantaneously by using the shutter. Therefore, the composition and doping concentration of the film can be adjusted rapidly with the change of the source. This is both an advantage and a disadvantage for MBE growth. Due to the lack of chemical process, it is difficult to obtain high quality MBE films in the process of single-layer compound growth.

There are three kinds of gauges used to detect vacuum degree, which have different detection range of vacuum degree. The first is Pirani gauge, which is mainly used to detect the vacuum degree of mechanical pump. Its detection range is from atmospheric pressure to 1×10^{-3} mbar.

4.2.2 MBE System Composition

As shown in the Fig.4.1, main chamber (5) keeps ultrahigh vacuum by pump system (1), the sample holder is transferred by transfer arm （4） into main chamber. To keep sample holder onto sample stage, it must coordinate the position of transfer arm and manipulator (2). Before growth, the surface of substrate is checked by RHEED (3). (7) and (8) are evaporator source and electron beam source respectively. For some researches, in-situ MOKE (magnetoresistance optical kerr effect) detection is required. (6) is the laser of MOKE system.

The low deposition rate of MBE is required to operate in UHV environment. Generally, the pressure requirement is lower than 10^{-10} mbar, which can be achieved by combining mechanical pump, molecular pump, ion pump and titanium sublimation pump. The crude vacuum reduces the air pressure of the chamber from atmospheric pressure to about 10^{-3} mbar by mechanical pump, which can quickly extract a large amount of air. Moreover, molecular pump, ion pump and titanium sublimation pump all depend on the operation of mechanical pump.

The molecular pump uses turbine blades to operate at a high speed of 20000 ~ 50000 rpm to extract gas. Usually, its working pressure is 10^{-1} ~ 10^{-10} mbar. The ion pump first ionizes the gas in the container, and uses high pressure to accelerate the ion to enter the solid electrode, thus reducing the pressure. Under ideal conditions, the ion pump can reach a vacuum of 10^{-11} mbar. In contrast, titanium sublimation pump (TSP) can further vacuum to the order of 10^{-12} mbar. The working principle of TSP is that the titanium filament is heated up to the sublimation point, and the sublimated titanium covers the surface to form a reaction layer to capture active elements such as O, N and H.

There are two kinds of gauges used to detect vacuum degree, which have different detection range of vacuum degree. One is Pirani gauge, which is mainly used to detect the vacuum degree of mechanical pumps. Its detection range is from atmospheric pressure to 1×10^{-3} mbar. The other one is the ion gauge with the highest working accuracy, ranging from 1×10^{-3} mbar to 1×10^{-11} mbar, which is generally used in the

main chamber. By using these gauges in combination, the vacuum (atmospheric pressure to 1 × 10^{-10} mbar) can be detected in all aspects. The atomic layer can be deposited on the substrate layer by layer by heating and evaporating the source material with high purity. If the growth of the film material and the substrate lattice constant match, the perfect epitaxial growth can be achieved. Therefore, by selecting a specific substrate and growth parameters, the non-equilibrium crystal structure can be generated, so as to tune and control the material properties at the atomic level. For the growth of two-dimensional materials, the requirement of the lattice matching between the film and the substrate is not high due to the van der Waals force between the layers.

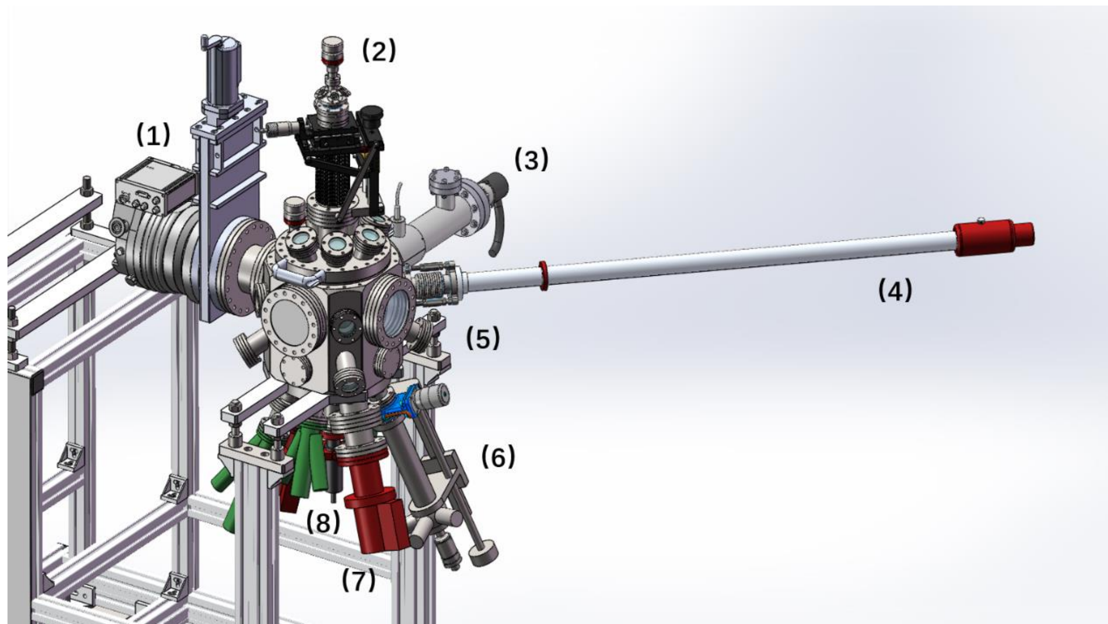

Fig 4.1 the schematic of MBE system: (1) pump system, (2) manipulator, (3) RHEED gun, (4) transfer arm, (5) main chamber, (6) laser of MOKE system, (7) e-beam source, (8) evaporator source

Traditional MBE process usually includes a series of carefully operated steps. Starting with substrate preparation, then stabilizing and calibrating the evaporation source, preparing buffer layer, and then growing thin film or heterojunction. After the growth, the samples were annealed again, and the samples were protected by the coating. MBE

growth parameters have a large operating space, such as growth temperature, evaporation rate, component ratio, thickness and substrate stress.

In this project, MBE system is the main technology of material preparation. In MBE system, there are usually three kinds of solid sources for evaporation of elemental materials. For low melting point materials, Knudsen cell can be used to evaporate high purity elements. Its principle is to use tungsten filament to heat the pyrolytic boron nitride crucible. The highest temperature of the beam source furnace is limited by the thermal stability of the crucible. Therefore, it is usually used in materials with relatively low melting point, such as Si and III - V group elements, including Ga, Al, In, Mg, etc. Since the evaporation of the beam source furnace is directly proportional to the source temperature, and the source temperature can be controlled within 0.1 ° C, the beam source furnace is very stable and easy to control.

4.2.3 Sample Holders and Clamps

The passivated GaAs was placed on the molybdenum sample holder (3mm thickness) and clamped by molybdenum flake of 0.1mm thickness. The area of sample holder is slightly larger than the size of sample, $14 \times 10\ mm$ and $10 \times 12\ mm$ respectively, as shown in Fig.4.2. The sample holders and clamps were made by molybdenum, because molybdenum has high sublimination point. When the system was heated up, the sample holder will not be thermal decomposition.

Two fine screws fixed the clamps and there are also made by molybdenum.

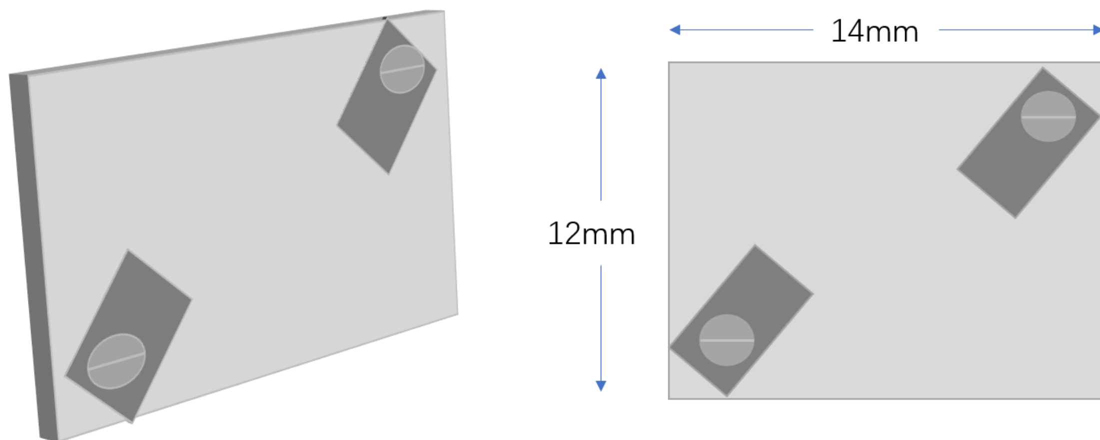

Fig 4.2 the illustration of sample holder. The molybdenum sample holder is 14mm length and 12mm width. The clamps were fixed by molybdenum fine screws.

Therefore, there are two regions that are covered by molybdenum clamps. This is the reason that SEM and AFM images can be seem the edges between substrate and transition metal disulfide monolayers.

■ Measurement Techniques

2D materials thin films have been the subject of much study over the last two decades due to the interest from the new generation of semiconductor and the magnetic materials.

The semiconductor of layered transition metal selenides generally has the characteristics of single-layer direct band gap and bulk indirect band gap. This feature makes transition metal sulfides such as molybdenum disulfide, tungsten disulfide, platinum disulfide and other materials have great potential to replace silicon as a new generation of semiconductor devices. Hence, there is a wide range of materials regarding practical application for these films. CVD and mechanical exfoliation are widely used in the growth of these single-layer two-dimensional materials, but it is difficult to obtain large-scale and high-quality single-layer films of transition metal sulfides at present. Therefore, there is still a long way to go in large-scale industrial production and replacing silicon as a new generation of semiconductor. In recent years, such as semiconductor of transition metal disulfide, the next generation semiconductor, have become increasingly hot and there are many studies in this emerging area. A wealth of research has been undertaken and a wide range of experimental techniques have been established and used to fabricate and characterize the sampled studies in all projects. Some of these techniques can be found in York-Nanjing university joint center, or in cooperated laboratories in Nanjing university. This chapter will present a description of various experimental techniques that have been utilized in this project, and is divided into several sections, including in-situ reflective high-energy electrons diffraction (RHEED), x-ray photoelectron spectroscopy (XPS), scanning electron microscopy (SEM), atomic force microscopy (AFM), transmission electron microscopy (TEM), and electron transport measurement.

5.1 Reflective High-Energy Electron Diffraction (RHEED)

There are many kinds of surface analysis methods. RHEED equipment and its working principle will be introduced in this section, which is one of the most direct in-situ detection methods in MBE chamber. Reflective high energy electron diffraction device (RHEED) is a very important part of MBE equipment, which can be used to in-situ observe the cleanliness, flatness and surface structure of sample surface. Therefore, reflective high-energy electron diffractometer has become a standardized technique for monitoring the surface morphology of thin films in MBE, PLD and other systems.

In our laboratory, RHEED uses 15 KV electrons to graze onto the smooth surface of the sample at a very small angle, so that the electrons that are elastically scattered back are confined to several layers of atoms on the surface after a long distance. The advantage of this method is that it can be easily mounted into a molecular beam epitaxy device to in-situ observe the growth process and mode. In an MBE device, a single crystal substrate is placed horizontally downward in a vacuum chamber to accept atoms that evaporate from the bottom up. The RHEED device is placed horizontally, and the electrons from the RHEED gun incident the single crystal substrate, reflecting the diffraction pattern onto the fluorescent screen at a very small grazing angle, as shown in Fig.5.1.

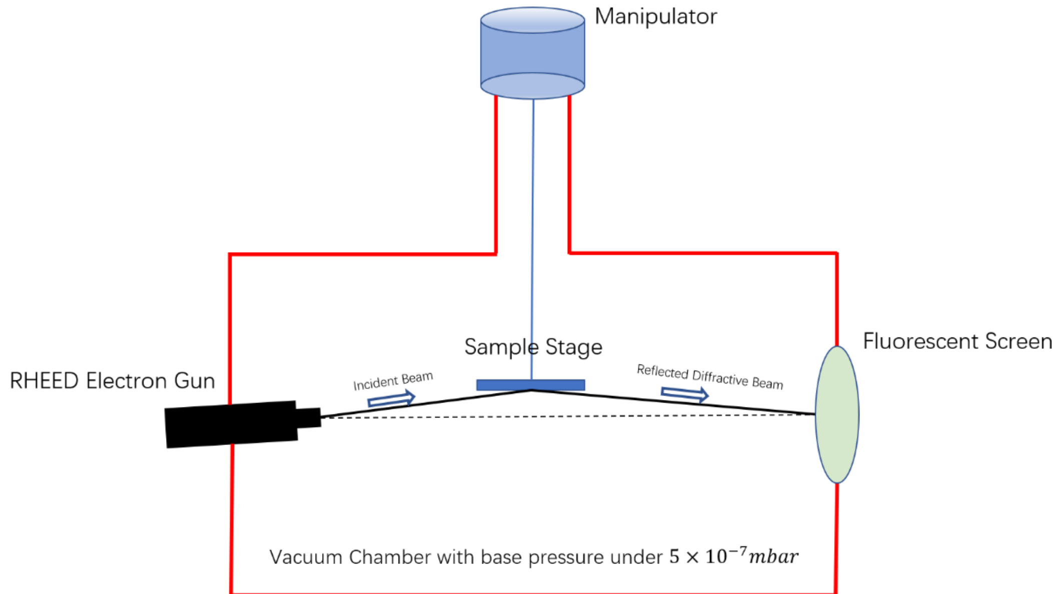

Fig 5.1 diagram of the device reflecting high energy electron diffraction in MBE vacuum chamber.

The surface sensitivity of the analytical method depends on the penetration depth of the particles injected into the sample or the escape depth of the particles escaping from the sample. The penetration depth and escape depth are related to the mean free path l of particles that depends on the electron energy and the properties of the interacting solid. When energy of incident electron beam reach to 15 KV, the l will be around 170Å for semiconductor. As shown in Fig.12, because RHEED is grazing incidence, its penetration depth d in solid can be obtained by formula:

$$d = \frac{l}{2} sin\,\theta \tag{14}$$

Where θ is grazing angle. From formula 14, the penetration depth or escape depth should be 4.45Å when the grazing angle is 3°. Therefore, RHEED can be a considerable method to detect the atoms of surface.

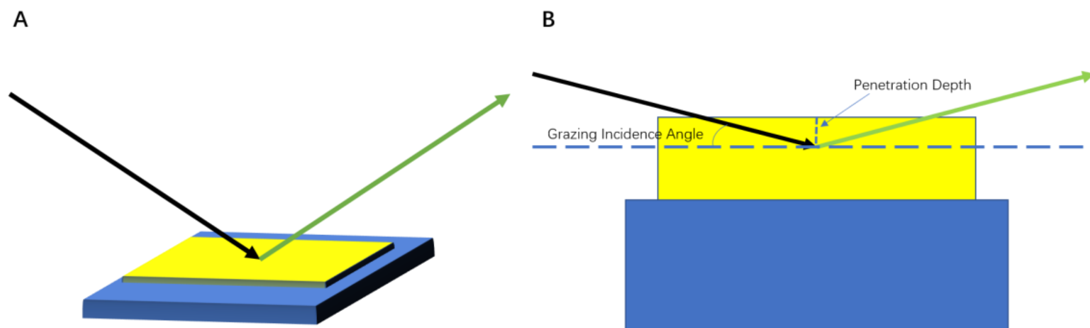

Fig 5.2 RHEED electron beam grazing on the sample surface. (A) incidence beam (black) on the film (yellow) that is grown on the substrate (blue), and reflective beam (green) to fluorescent screen. (B) cross section views of the sample and electron beams.

In fact, RHEED is very sensitive to surface morphology and crystallization properties due to its reflection and diffraction characteristics. RHEED patterns can be divided into reflection and transmission patterns. For single crystal thin films, both patterns can be observed, and the observed patterns depend on the surface morphology of the films, as shown in Fig.5.2 A and Fig.5.2 B.

On a smooth single crystal surface, electrons are reflected by the surface. In this reflection mode, electrons penetrate only the surface atomic layer, so the reciprocal space is some one-dimensional rod along the spherical normal in Fig.5.3 A. In Fig.5.3 B shows the Ewald spheres in the corresponding reciprocal space, where the sphere intersects each reciprocal bar to produce a reflection beam and extend the stripes, which are centered on the Laue's ring (dashed line). In RHEED geometry, only the upper half of the diffraction pattern can be used for analysis and calculation because the pattern at the bottom is obscured by the substrate, known as the shadow boundary. The direct incident spot is directly below the shadow because the incoming electrons do not impact the sample. From the reciprocal relation, the spacing of the diffraction fringes reflects the period of the crystal lattice along the direction of the electron beam. From the reciprocal relation, the spacing of the diffraction fringes reflects the period of the crystal lattice along the direction of the electron beam.

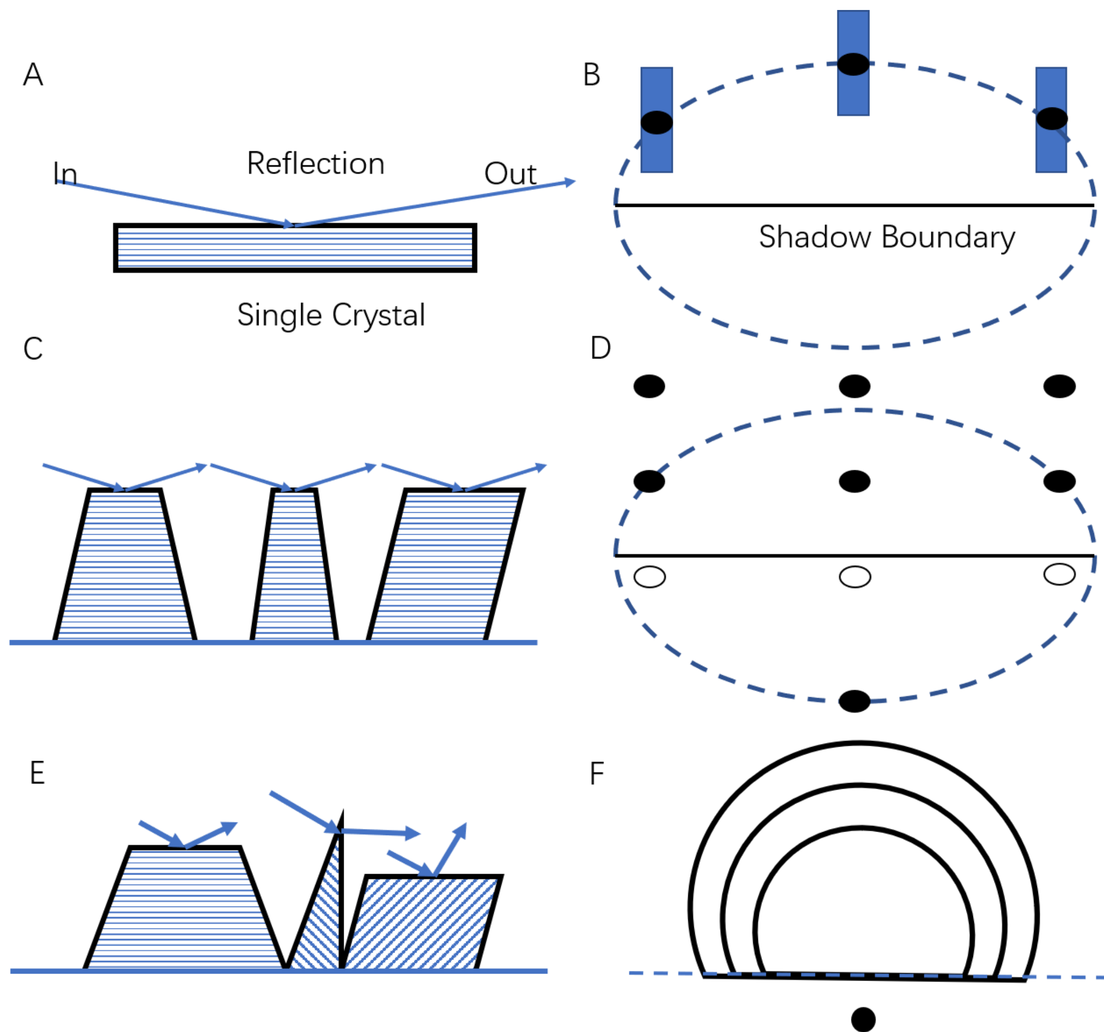

Fig 5.3 schematic representation of electron scattering mechanism, film morphology and RHEED diffraction of various surface structures. (A) and (B) schematic and RHEED diffraction of electron scattering and single-crystal layered growth films. (C) and (D) schematic and RHEED diffraction of electron scattering in single-crystal island films. (E) and (F) the diagram of electron beams incidence onto multi-crystal of films and RHEED diffraction of multi-crystal films.

Although RHEED reflection patterns are often used to study the surface properties of single crystals, transmission patterns can often be observed. As shown in Fig.5.3 C, there are obvious small island protuberances on the surface of the single crystal. It is because the electron beam easily penetrates these islands that the transmission diffraction is formed. In the transmission mode, most electrons enter the single-crystal film from one side of the island and scatter from the other side. Fig.5.3 D shows the corresponding diffraction pattern, which is very similar to the transmission diffraction

in TEM. The difference is that due to the shadow, the diffraction spots below the solid surface will not be observed by the projection diffraction of RHEED.

Polycrystals usually have rough surfaces because they are composed of many crystals with different orientations as shown in Fig.5.3 E. After the electrons penetrate the crystal, a diffraction pattern is formed in Fig. 5.3 F. Compared with the projection pattern formed by single crystal, the pattern of polycrystalline film has significant characteristics. In a polycrystalline film, all islands have different polycrystalline orientations and different directions of reciprocal space. The reciprocal spatial structure can be viewed as a series of concentric circles when the crystal is oriented freely. The radius and radian distribution of rings can reflect the structure and orientation of thin film crystals to some extent.

5.2 XPS Measurement (X-Ray Photoelectron Spectroscopy)

X-ray photoelectron spectroscopy (XPS) is an advanced analytical technology in the microanalysis of electronic materials and components. It not only provides information on molecular structure and atomic valence state for chemical research, but also provides information on element composition and content, chemical state, molecular structure and chemical bond of various compounds for electronic materials research. When analyzing electronic materials, it can not only provide general chemical information, but also provide surface, micro area and depth distribution information. In addition, because the X-ray beam incident on the sample surface is a photon beam, the damage to the sample is very small.

X-ray photoelectron spectroscopy (XPS) uses X-ray to irradiate the sample, which can excite the inner electrons or valence electrons of atoms or molecules. The electrons excited by photons are called photoelectrons, which can measure the energy of photoelectrons. Taking the kinetic energy of photoelectrons as the abscissa and the relative strength as the ordinate, the photoelectron spectroscopy can be made to obtain the composition of the object to be measured.

For growth of layered 2D materials, XPS is one of most wide method to detect chemical composition. XPS measurement is normally in ultrahigh vacuum chamber with level of $10^{-10}\ mbar$.

The illustration of XPS is shown in Fig.5.4 that the x-ray beam focuses on surface of substrate and emitted electrons are collected from a narrow area of surface. X-ray penetration depth is quite large with$1\ mm$, and the x-ray excitation area is $1 \times 1\ cm^2$. The emitted electrons can be from this whole $1 \times 1\ cm^2$, but not be extracted completely. The extracted electrons normally are from an area of circle with $1 \times 1\ mm^2$ diameter. $10\ nm$ thickness of film can be detected and extracted by XPS collector.

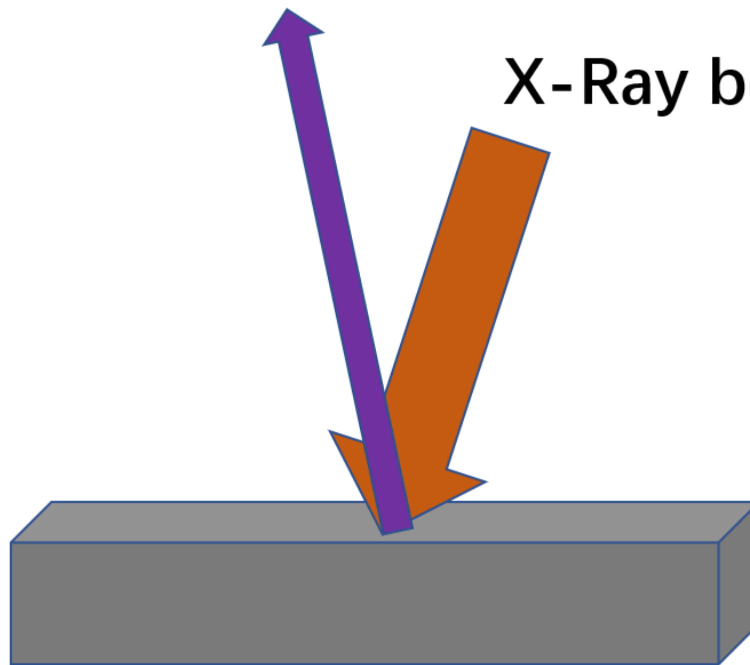

Fig 5.4 illustration of XPS measurement. X-ray focusing onto surface of substrate and collected electrons from a smaller area of surface.

The photoelectric process in XPS measurement is illustrated in Fig.5.5 that the ejected electron was motivated by incident x-ray (purple line). XPS spectral lines are identified by the shell from which the electron was ejected. Following this process, atom will release energy by the emission of an Auger electron.

If XPS spectra were presented on a kinetic energy scale, one would need to know the X-ray source energy used to collect the data in order to compare the chemical states in the sample with data collected using another source.

It is necessary to know that the various elements possibly have different sensitivities for extracted electron. As presented in Fig.5.6, there are different elements and their relative sensitivities. The binding energies of some elemental ejected electrons are same with those of other elements, such as both Ga 3s and S 2p at around 160 eV. If the system contains two or more elements at one binding energy, it is necessary to analyses

the peak by fitting data of multiple peaks.

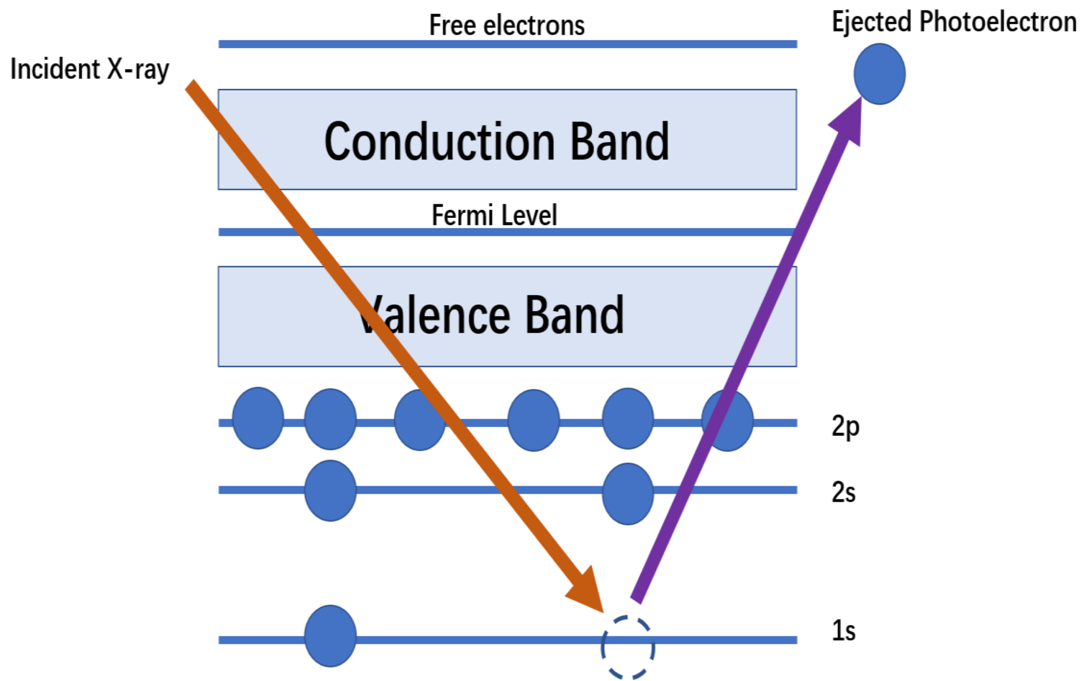

Fig 5.5 the photoelectric process of XPS. Incident x-ray motivating an electron of 1s shell.

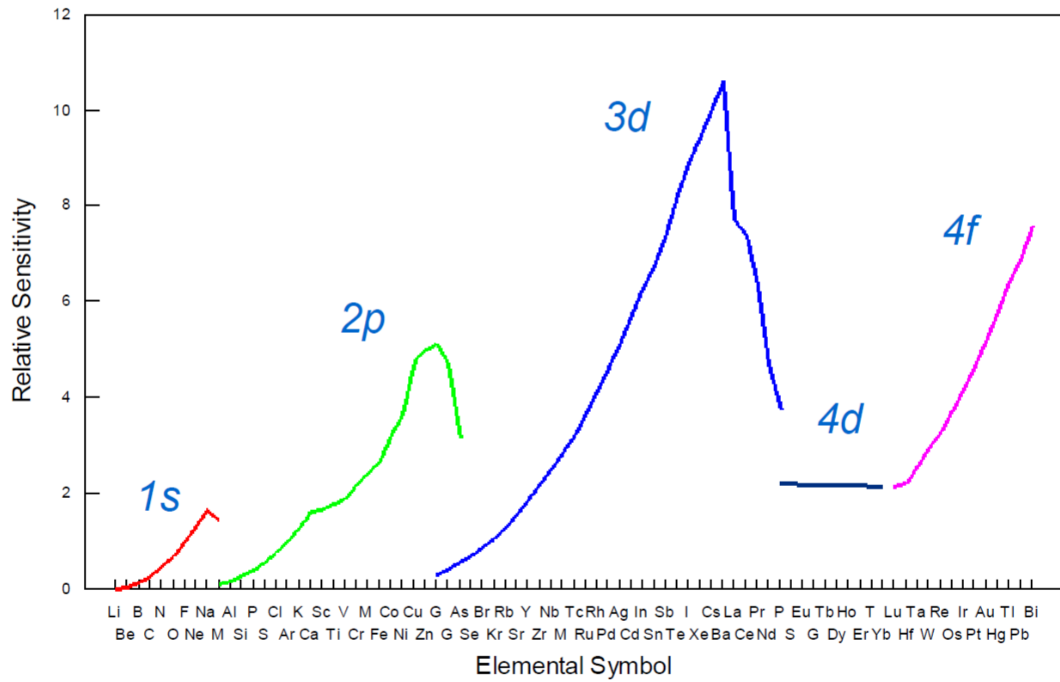

Fig 5.6 relative sensitivities of the elements: 1s orbital (red line), 2p orbital (green line), 3d orbital (blue line), 4d orbital (navy one) and 4f orbital (pink one).

5.3 Scanning Electron Microscopy Measurement (SEM)

SEM mainly uses the secondary electron signal imaging to observe the surface morphology of the sample. Scanning the sample with very narrow electron beam can produce various effects through the interaction between the electron beam and the sample, among which the secondary electron effect is the main one. Scanning electron microscopy (SEM) is a means of microscopic observation between transmission electron microscopy and optical microscopy, which can directly use the material properties of the sample surface for microscopic imaging. The advantages of SEM are: (1) high magnification, 20-200000 times continuously adjustable; (2) large depth of field, large field of vision, three-dimensional imaging, which can directly observe the fine structure of the uneven surface of various samples; (3) sample preparation is simple, and the current SEM is equipped with X-ray spectrometer device, which can simultaneously observe the microstructure and morphology. Area composition analysis (SEM-EDS), so it is one of the most important scientific research instruments.

In principle, scanning electron microscopy (SEM) is to scan the specimen with a very fine focused high-energy electron beam, which can excite all kinds of physical information. By receiving, amplifying and displaying this information, the surface morphology of the test sample can be observed.

When a very fine high-energy incident electron bombards the sample surface, the excited region will produce secondary electrons, Auger electrons, characteristic X-ray and continuous spectrum X-ray, backscattered electrons, transmission electrons, as shown in Fig.5.7. At the same time, it can produce electron hole pair, lattice vibration (phonon), electron vibration (plasma).

The secondary electron refers to the extranuclear electron bombarded by the incident electron. Because the binding energy between the nucleus and the outer valence electrons is very small, when the outer electrons of the atom get more energy than the corresponding binding energy from the incident electrons, they can break away from the atom and become free electrons. If the scattering process occurs close to the surface of the sample, those free electrons whose energy is greater than the work of the material

can escape from the surface of the sample and become free electrons in vacuum, i.e. secondary electrons. The secondary electrons come from the region 5-10nm away from the surface. It is very sensitive to the surface state of the sample and can effectively show the micro morphology of the sample surface. Because it comes from the surface of the sample, the incident electron has not been reflected many times, so the area of the secondary electron is not much different from the area of the incident electron, so the resolution of the secondary electron is high, generally 5-10nm. Secondary electrons and backscattered electrons can be used for imaging, but the latter is not as good as the former, so secondary electrons are usually used. The resolution of SEM is generally secondary electron resolution.

The vacuum system mainly includes two parts: vacuum pump and vacuum column. The vacuum column is a sealed cylindrical vessel. A vacuum pump is used to create vacuum in the vacuum column. There are three categories of mechanical pump, oil diffusion pump and turbine molecular pump. The combination of mechanical pump and oil diffusion pump can meet the vacuum requirements of SEM equipped with tungsten gun, but for SEM equipped with field emission gun or lanthanum hexaboride gun, the combination of mechanical pump and turbine molecular pump is required. Both the imaging system and the electron beam system are built into the vacuum column, and the bottom end of the vacuum column is used to place the sample.

The reason why vacuum is used is mainly based on the following two reasons: (1) The filaments in the electron beam system will oxidize rapidly in the ordinary atmosphere and fail, so in addition to the vacuum used in SEM, the vacuum column should be filled with pure nitrogen or inert gas at ordinary times. (2) In order to increase the average free path of electrons, more electrons are used for imaging.

Scanning electron microscope can clearly reflect and record the micro characteristics of samples, which is a convenient and easy way to observe and analyze the micro structure of samples. Samples do not need to be prepared, but can be observed directly in the sample room. At the same time, scanning electron microscope can realize the positioning analysis of samples from low resolution to high-resolution. The samples in the sample stage can not only move along the three-dimensional space, but also It can

rotate the space according to the observation needs, so as to facilitate the users to continuously and systematically observe and analyze the specific parts. The scanning electron microscope images are real, clear and full of three-dimensional sense, which have been widely used in the observation and research of three-dimensional microstructure of nano materials.

Fig.5.8 shows a SEM image of a previous research, which presents the morphology of 100-squre-centimenter single crystal hBN monolayer on copper[18]. From this image, the aligned hBN domains and their edges can be directly observed. To distinguish the edge between the film and the substrate by SEM is very important for MBE film growth.

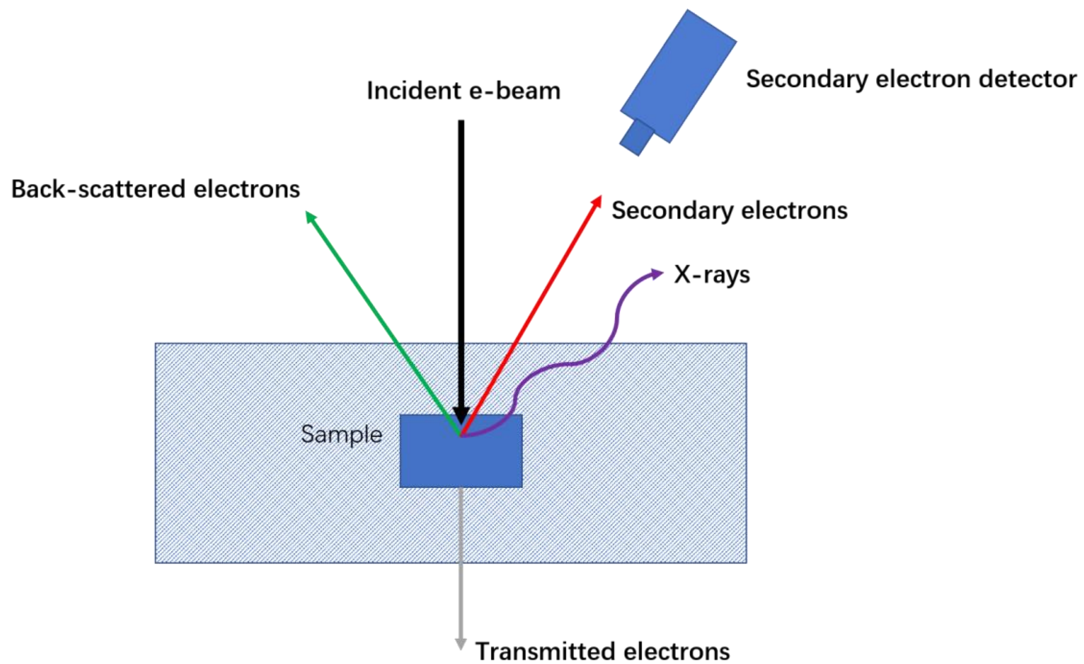

Fig 5.7 schematic of SEM working principle.

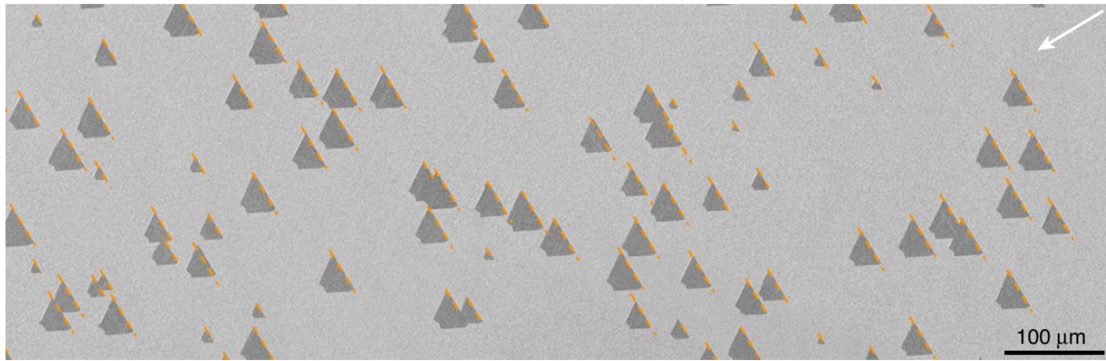

Fig 5.8 SEM image of hBN in previous study[18]. SEM image of aligned hBN domains on the Cu (110) substrate.

5.4 Atomic Force Microscopy (AFM)

AFM is called atomic force microscope. It is a new instrument with high resolution at atomic level invented after STM. It can detect the physical properties of various materials and samples in the atmosphere and liquid environment, including the morphology, or directly conduct nano manipulation. It has been widely used in semiconductor, nano functional materials, biology, chemical industry, food, medicine research and scientific research institutes. In the research and experiment fields of various nano related disciplines, it has become the basic tool of nano science research. Compared with STM, AFM has more extensive applicability because it can observe non-conductive samples.

Atomic force microscopy (AFM), an analytical instrument, can be used to study the surface structure of solid materials including insulators. It studies the surface structure

and properties of materials by detecting the extremely weak atomic interaction between the surface of the sample to be tested and a micro force sensing element. The basic AFM consists of laser generator, detector, cantilever arm and probe. as shown in Fig.5.9. The interaction force between the probe and the sample makes the micro cantilever deflect upward or downward. The laser is used to irradiate the light at the end of the cantilever, and the position change of the reflected light is used to measure the displacement of the cantilever. The cantilever is usually made of a silicon flake or silicon nitride flake which is generally $100-500\ \mu m$ long and about $500\ nm$-$5\mu m$ thick. The tip of the cantilever has a sharp tip, which is used to detect the interaction between the sample and the tip. In the system of atomic force microscope (AFM), when there is interaction between the prob tip and the sample, the cantilever will swing. When the laser irradiates the end of the cantilever, the position of the reflected light will also change because of the cantilever swing, which results in the generation of offset. In the whole system, the offset is recorded and converted into electrical signal by laser spot position detector.

From Fig.5.10, when one end of the cantilever which is extremely sensitive to weak force is fixed and the tip of the other end is close to the sample, and the force will make the microcantilever deform or change its motion state. When scanning the samples, the force distribution information can be obtained by using sensors to detect these changes, so that the surface morphology and structure information and surface roughness information can be obtained with nanometer resolution.

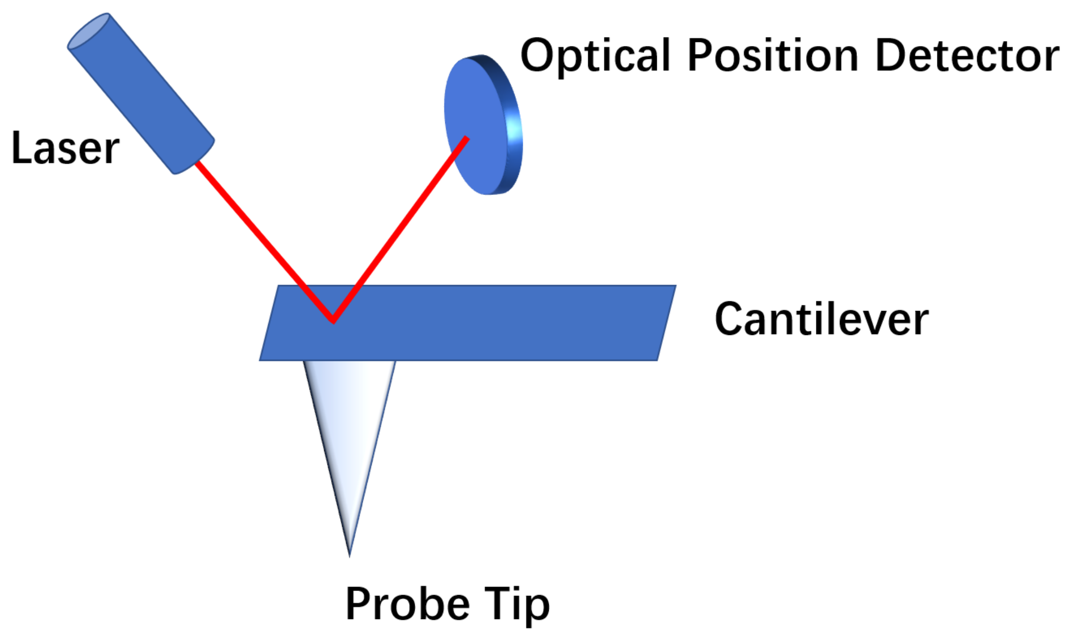

Fig 5.9 AFM structure diagram: the probe is connected with the cantilever arm, and the optical position detector determines the three-dimensional position of the probe by receiving the laser signal.

All AFM facilities in this project are tap mode tip AFM that are commonly used products with high resolution and general service life. Tapping mode is also called dynamic force or intermittent contact. The probe resonates under the driving of external force, and part of the vibration position of the probe enters into the repulsion zone of the force curve, so the probe contacts the sample surface intermittently. The probe requires a high cantilever elastic coefficient to avoid seizing the micro layer water film on the sample surface. Tapping mode has a small force on the sample, which is particularly beneficial to improve the resolution of the soft sample. At the same time, the lifetime of the probe is slightly longer than that of contact mode. In the process of using, the probe is constantly worn and the resolution is easy to decline. Tapping probe AFM is mainly used for surface morphology observation.

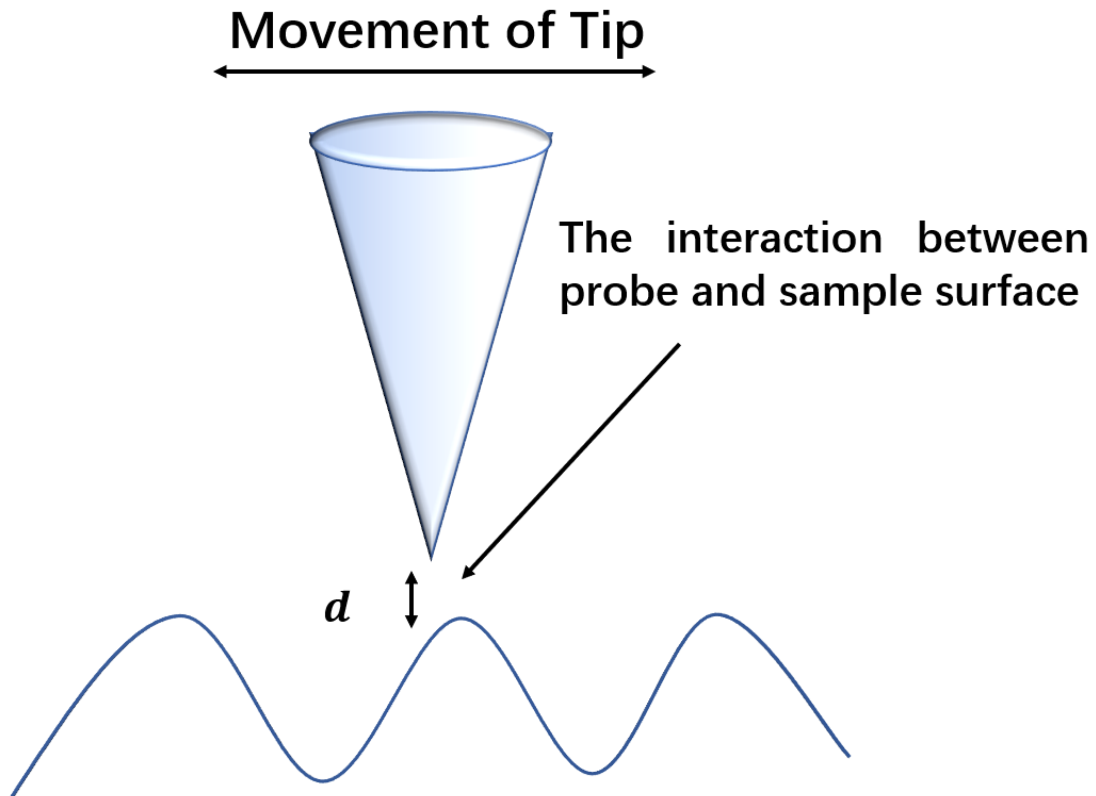

Fig 5.10 Schematic diagram of probe and sample surface. The feedback system controls and maintains a constant distance (d) between the probe and the sample surface

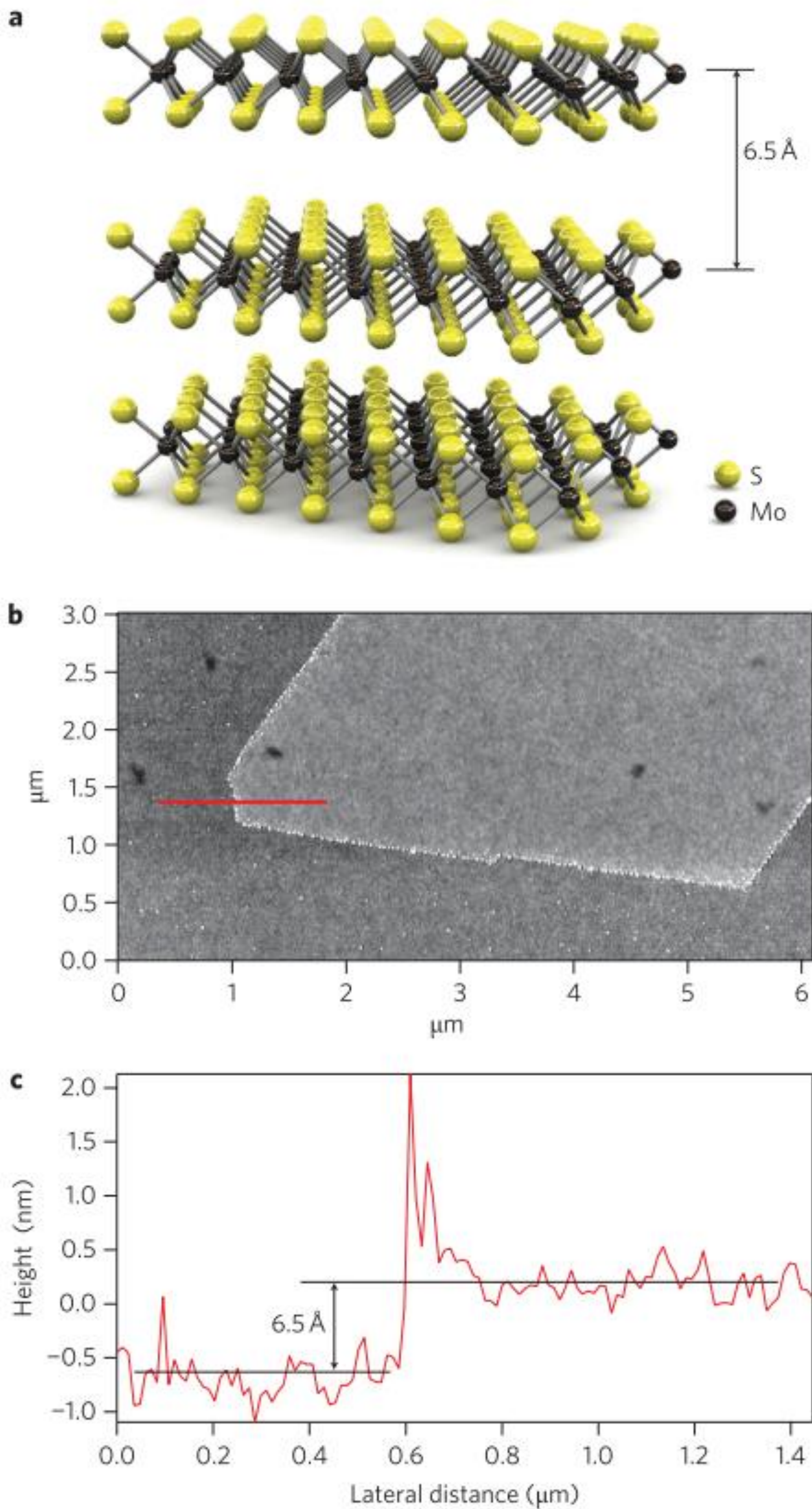

Fig 5.11 structure and AFM imaging of monolayer MoS_2. a, three-dimensional representation of the structure of MoS_2. Single layers, 6.5 Å thick, can be extracted using scotch tape-based

micromechanical cleavage. b, Atomic force microscope image of a single layer of MoS_2 deposited on a silicon substrate with a 270-nm-thick oxide layer. c, Cross-sectional plot along the red line in b[28].

Fig.5.11 is an AFM diagram of monolayer MoS_2, which was reported in 2011[28]. In the Fig.5.11a is the atomic structure diagram of molybdenum disulfide which the thickness is 6.5Å. The AFM image can be obtained from Fig.5.11b, which the MoS_2 domain and its edge can be clearly observed. The image size is $6 \times 3\ \mu m$. MoS_2 Domain and substrate can be distinguished by the change of color that the grey part is domain. Fig.5.11c shows the step thickness between molybdenum disulfide and substrate on AFM scanning surface. The scanning thickness of single layer MoS_2 is 6.5Å. Because of the mechanism of tapping AFM, there will be an obvious unrealistic jump on the thickness curve, which will happen near the step.

5.5 Transmission Electron Microscopy

Transmission electron microscope (TEM), is to project the accelerated and aggregated electron beam onto the very thin sample. TEM is a large-scale nonanalytic equipment, which uses high-energy electron beam as illumination source to magnify the sample. The electron collides with the atoms in the sample and changes the direction, resulting in the solid angle scattering. The size of the scattering angle is related to the density and thickness of the sample, so different light and shade images can be formed. The images will be displayed on the imaging devices (such as fluorescent screen, film, and photosensitive coupling components) after being magnified and focused.

The resolution of TEM is much higher than that of optical microscope, SEM and AFM, which can reach $0.1 - 0.2nm$, and the magnification is tens of thousands to millions of times. Therefore, the transmission electron microscope can be used to observe the fine structure of the sample, and even the structure of the single atomic layer. TEM is an important analytical method in many fields related to physics and biology, such as cancer research, virology, materials science, nanotechnology, semiconductor research and so on.

The imaging principle of electron microscope is basically the same as that of optical microscope, but the former uses electron beam as light source and electromagnetic field as lens. In addition, because the penetration of electron beam is very weak, the specimen used for electron microscopy must be made into ultra-thin sections with a thickness of about $50\,nm$. This kind of slice needs to be made by ultra-thin microtome. The magnification of the electron microscope can be up to nearly one million times, which is composed of five parts: lighting system, imaging system, vacuum system, recording system and power supply system. If it is subdivided, the main part is the electron lens and imaging recording system, which consists of the electron gun, condenser, sample port, objective lens, diffractometer, intermediate lens, projection lens, fluorescent screen and camera placed in the vacuum. As shown in Fig.5.12, we can know the structure of TEM and the distribution of main devices.

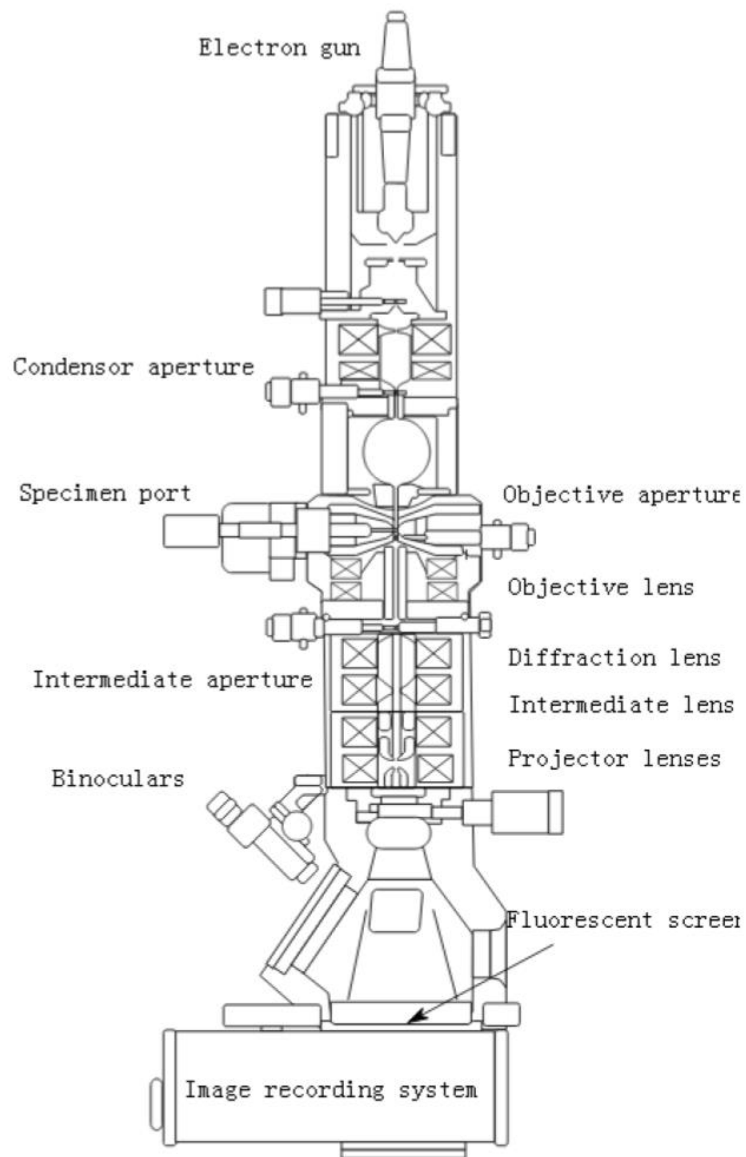

Fig 5.12 layout of components in a basic TEM

5.6 Superconducting Quantum Interferometer Device Measurement

As one of the most widely used representative magnetic measuring devices, SQUID-VSM works by characterizing the material's bulk magnetization by the change of magnetic flux when the magnetic sample in the induction coil vibrates near it. In a typical SQUID-VSM, the sample (usually 1-3mm) is usually mounted on a non-magnetic rod and connected to a mechanical vibrator (usually frequency < 40 Hz, amplitude ~several millimeters) or speaker (usually frequency < 100 Hz, amplitude ~0.1mm).

Due to the quantization of magnetic flux in the superconducting ring, any change in magnetic flux results in a change in the shielding current in the closed circuit, and SQUID responds by equally amplifying the output voltage. By fixing the detection coil and the sample moving speed, the voltage curve is directly proportional to the sample magnetization. To apply a magnetic field to the sample, the detection coil is fixed in the hole of the superconducting magnet. To achieve temperature control, the sample rod is placed in a sealed, variable-temperature chamber, and is thermally insulated from the magnet, as shown as Fig 5.13[93]. It is worth mentioning that although the instrument and calibration technology determine the measurement accuracy of SQUID, the environment also plays an important role.

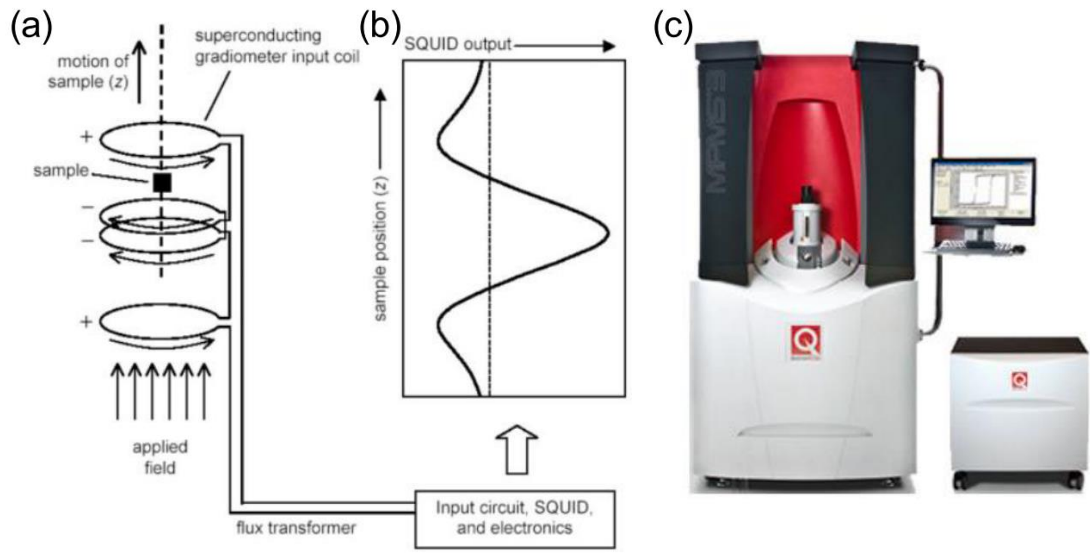

Fig 5.13 SQUID working principle and device diagram. a, diagrammatic sketch of signal collection coil; b, voltage response of sample measurements; c, instrument external photo.[93]

Sulfur-passivation Method on GaAs Substrate

In this section, the S atoms on the GaAs (111) B will be detailed introduced. Unlike the transitional growth of transition metal dichalcogenides (TMDC) materials, which the thin films are by co-growth method in the ultrahigh chamber system, the sulfide atoms are deposited on the GaAs (111) B on the air. This procedure makes strong chemical bonds of Ga-S and As-S. Even though some unrevealing details of sulfide passivation, the S atoms are strong connect the GaAs (111) B on the surface and inner GaAs (111) B bulk.

6.1 Background

Gallium arsenide has very superior semiconductor characteristics. Its electron mobility is 5 times larger than silicon, and it is also a direct gap semiconductor. It has obvious advantages over silicon in manufacturing ultra-high-speed devices and optoelectronic devices. Although the research on gallium arsenide has a history of nearly 50 years, its potential has not been fully exploited to make it play a leading role in the application of semiconductor devices. For a long time, the dominant position of silicon devices has been unshakable. There are many reasons for this situation, mainly in terms of technology, including the integrity of materials, difficulties in preparing large single crystals, high cost and complex device preparation technology. Among them, the surface passivation technology of GaAs is a problem that has not been solved completely.

For silicon devices, SiO_2 is a very ideal passivation film, which can be formed by the surface oxidation of silicon, so it is called self-oxidation layer. The Si/SiO_2 interface has very low density of States and good chemical stability. Due to outstanding properties of silicon, nowadays most applications and devices are made by silicon[94, 95]. It can be used as a passivation film for silicon devices and as a metal oxide semiconductor (MOS) FET. In the 1960s and 1970s, great efforts were devoted to the study of the autoxides of GaAs. It was found that, on the other hand, the arsenic oxide is unstable, and the following reactions will take place between it and GaAs:

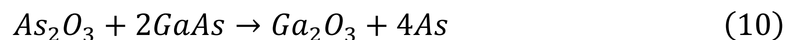

$$As_2O_3 + 2GaAs \rightarrow Ga_2O_3 + 4As \tag{10}$$

Therefore, since the 1980s, people have realized that it is not feasible to passivate compound semiconductors with self-oxide layer, and it is necessary to find passivation layer made of other materials.

Owing to the development of second-generation semiconductor devices GaAs, to improve the properties to meet various requirement in industry have attracted renewed interests. To pursuit the low current density of GaAs surface, similar with SiO_2/Si the initial studies utilized S atoms to reduce the current density of GaAs (100)[72, 73].

Meanwhile, according recent studies, sulfur also can improve properties of materials by other areas[96]. Following, the increasing studies focused on the passivation by various methods, such as Na_2S, $(NH_4)_2S$, and $(NH_4)_2S_x$[74, 75, 80, 84, 97-100]. However, there is an argument that the current density of S/GaAs (111) B is reduced than that of GaAs (111)[84, 101].

No matter the current density changes on the S/GaAs (111) B, the certain is sulfide atoms will be connected strongly with the surface atoms of GaAs. This feature provides me the indication of growth monolayers of transition metal disulfide materials.

6.2 Sulfide passivation on the GaAs (111) B

The GaAs (111) B surface is well known the structure of As-terminated threefold coordinate geometry. The solution of $(NH_4)_2S_x$ treated GaAs have been proven in the previous studies, and more importantly, the $(NH_4)_2S_x$ solution is reported oxygen free. Thereby, the $(NH_4)_2S_x$ solution is ideal for this growth.

Fig 6.1 the GaAs (111) B dipped into $(NH_4)_2S_x$ solution.

Fig.6.1 indicate the GaAs in the solution of $(NH_4)_2S_x$, which some light-yellow sulfide powder was in the solution. The substrate in this investigation was cut from commercial n-type GaAs (111) single crystal wafer from AXT company. The substrates were prepared by methanol at room temperature, and then etching by H_2SO_4: H_2O_2: H_2O (4:1:1). The sulfide treating procedure was in the $(NH_4)_2S_x$

solution at 340K for 60 min[98, 101]. The passivation temperature and time have been tried for many times, and XPS results show that 340k and 60 minutes were the most suitable. After this treatment, these samples were rinsed by deionized water, following blown by dry He. After this passivation manner, samples were introduced into load-lock chamber which base pressure is 1×10^{-8}mbar. The samples were transferred into MBE main chamber (base pressure of $3 \times 10^{-10} mbar$) from load-lock chamber. Because the $(NH_4)_2S_x$ passivation possibly make float S powder deposit on the GaAs surface, the samples were heated up to 500K for 20 mins. After annealing, the S/GaAs (111) B were fully prepared. The samples have strong oxidation resistance.

6.3 RHEED Detection of S-Passivation GaAs

In our experiment, we introduced the $(NH_4)_2S_x$ passivation treatment which has advantages of cleaning of the GaAs surface oxides and nearly complete S coverage[77, 98]. Furthermore, this treatment was applied to significantly reduce the current density. Also, the monolayer of S atoms is extremely stable and antioxidative.

The passivated sample should be placed into the high-vacuum chamber to get rid of residual S atoms which are near 100Å[98]. At the room temperature (RT), the residual S atoms would sublime fast. Following, the passivated GaAs (111) B was heated up to the range of 170℃-210℃ to get the well-order RHEED pattern in Fig.6.2.

Since the samples stay in the ultrahigh vacuum chamber, the only way to determine the quality of samples is to observe RHEED (Reflection High Energy Electron Diffraction) patterns. The merits of RHEED are mainly because of its in-situ, convenient operation and surface sensitive.

The sample was passivated to obtain sulfur atoms on the surface of GaAs and placed into the load lock chamber. After being placed in the load lock chamber (base pressure ~ 8×10^{-7}mbar) for one hour, it was transferred into the main chamber which the base pressure was $3 \times 10^{-10} mbar$. The sample was annealed at 180℃ for 30 minutes and cooled to room temperature.

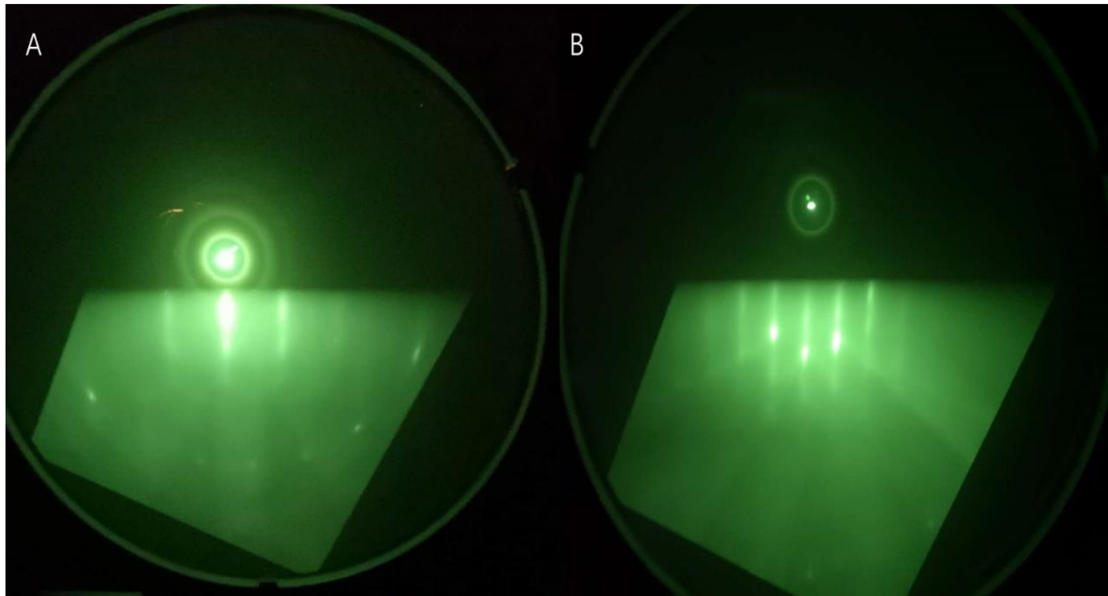

Fig 6.2 RHEED patterns taken from S/GaAs (111) B surface with 500K annealing for 20 mins. A) the diffraction pattern from [1 1 -2] axis crystal orientation of the S/GaAs (111). B) the [1 0 -1] direction of crystal orientation.

Fig.6.2 shows the RHEED patterns of various direction of atomic sulfide layer on the GaAs (111) substrate. From the RHEED patterns, it is clear that the S/GaAs (111) is single crystal. The beam voltage is 15 KV which the deepest distance of measurement is 4Å.

Fig.6.2A and B shows that RHEED images from two different crystal orientations, [1 1 -2] and [1 0 -1] respectively. The both images were taken when the sample was at room temperature. The Fig.6.2A can be seen that fingers are clear and secondary electrons can be observed on the screen. The Fig.6.2B not only can be achieved the clear fingers, but the Kikuchi line can be found.

The Fig.6.2 indicates that the annealed passivated-GaAs was single crystal. The crystal orientation and lattice structure corresponded with GaAs (111) B.

6.4 XPS Measurement of S/GaAs (111)

X-ray Photoelectron Spectroscopy (XPS) also known as Electron Spectroscopy for Chemical Analysis (ESCA) is a widely used technique to investigate the chemical composition of surfaces. The XPS penetration depth is around 10nm, which means when monolayer CoS2 was measured, the chemical information of substrate also could be detected. The XPS curves in this chapter is in-situ measurement, which the XPS chamber connects with MBE ultrahigh vacuum chamber.

Fig.6.3 shows the XPS data which indicate the chemical information of S/GaAs (111). The Fig.6.3A illustrates the S 2s peak with 227.9 eV. The single peak of 2s orbital electrons indicates all S atoms bond with GaAs surface nor float S atoms on the surface. The Fig 6.3B and C reveal the GaAs peaks. Fig.6.3D is the overview curve of S/GaAs (111).

XPS data indicated that there is a single sulfur peak at 227.9ev, and the peaks of gallium and arsenide are clearly visible. A single valence sulfur atom was detected on the surface of GaAs.

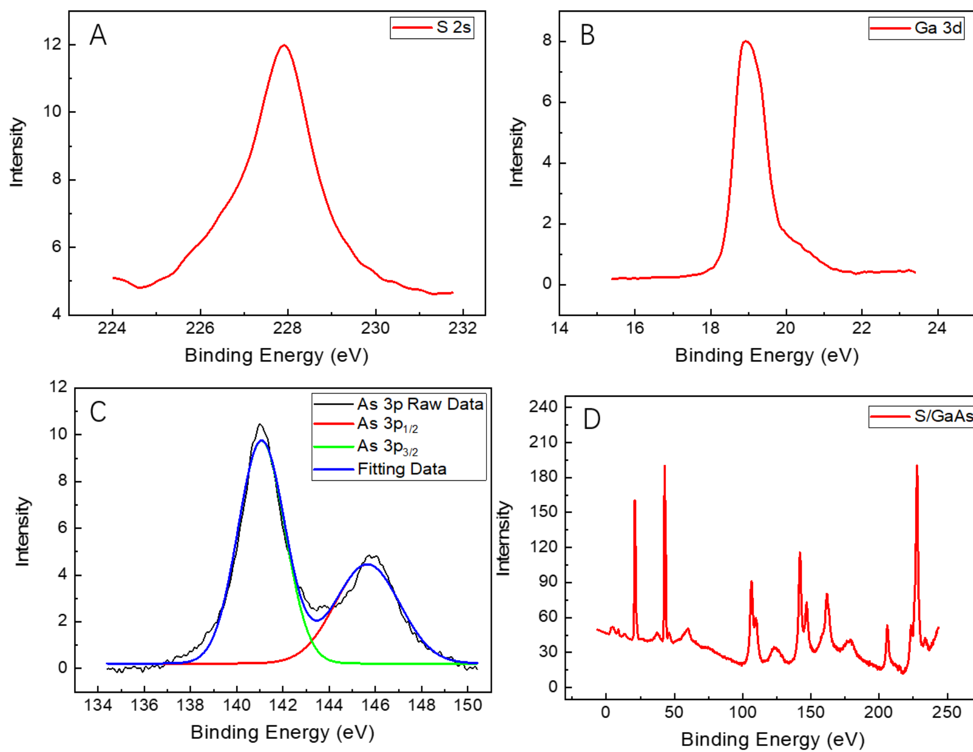

Fig 6.3 XPS data of S/GaAs substrate. A) the S 2s peak with character peak of 227.9eV. B) the Ga 3d peak at binding energy of 18.9eV. C) the As $3p_{1/2}$ and As $3p_{3/2}$ at 141.1eV and 145.6eV respectively. D) the overview XPS of S/GaAs (111).

6.5 AFM Measurement of S/GaAs (111)

Atomic force microscopy (AFM) is a wide technique to investigate surface morphology and thickness. The AFM perform in tapping mode, using repulsive Van der Waals force between the atoms on the surface and the atoms at the tip. A focused laser beam onto a cantilever, a photodetector collects the beam from the cantilever.

The passivated GaAs sample was introduced into the high-vacuum chamber with base pressure of $3 \times 10^{-10} mbar$ and kept in it for one hour, so that the floating sulfur on the sample surface can be removed easily. The S atoms will be sublimated at $-10°$ under $10^{-8} mbar$, which indicates that floating S atoms will be sublimated quicker under lower pressure environment. The smoothness of the films was measured ex-situ AFM as shown in Fig.6.4. Fig.6.4A shows the prepared GaAs morphology and thickness. The average thickness can be seen down to 0.5Å, which equalize to the device error. After passivation treatment, the surface is more rough than clean GaAs (111) as shown in Fig.6.4B. The maximum roughness is 2nm.

When the AFM tip sweeps the sample surface, the fluctuation of the film thickness on the substrate surface will be shown. The triangle like morphology of each small shape in the figure is a domain structure on the substrate. When the AFM tip sweeps the sample surface, the fluctuation of the film thickness on the substrate surface will be shown. The triangle like morphology of each small shape in the figure is a domain structure on the substrate. It can be seen from the Fig.6.4B that there are similar size and orientation quasi-triangle domains on the passivated sample surface. At the edges of domains of S/GaAs surface, the direction of the edges has same direction and length. It can also be seen from the figure that the surface of the passivated sample is much rougher than that of the substrate, which indicates that the passivated S atoms may not be a single layer. It is considered that aligned domains was caused by step-edge-mediated nucleation[18]. However, the difference between growth of hBN/Cu (111) and S/GaAs (111) is that passivation of GaAs is chemical method, which is should be homogenous and uniform.

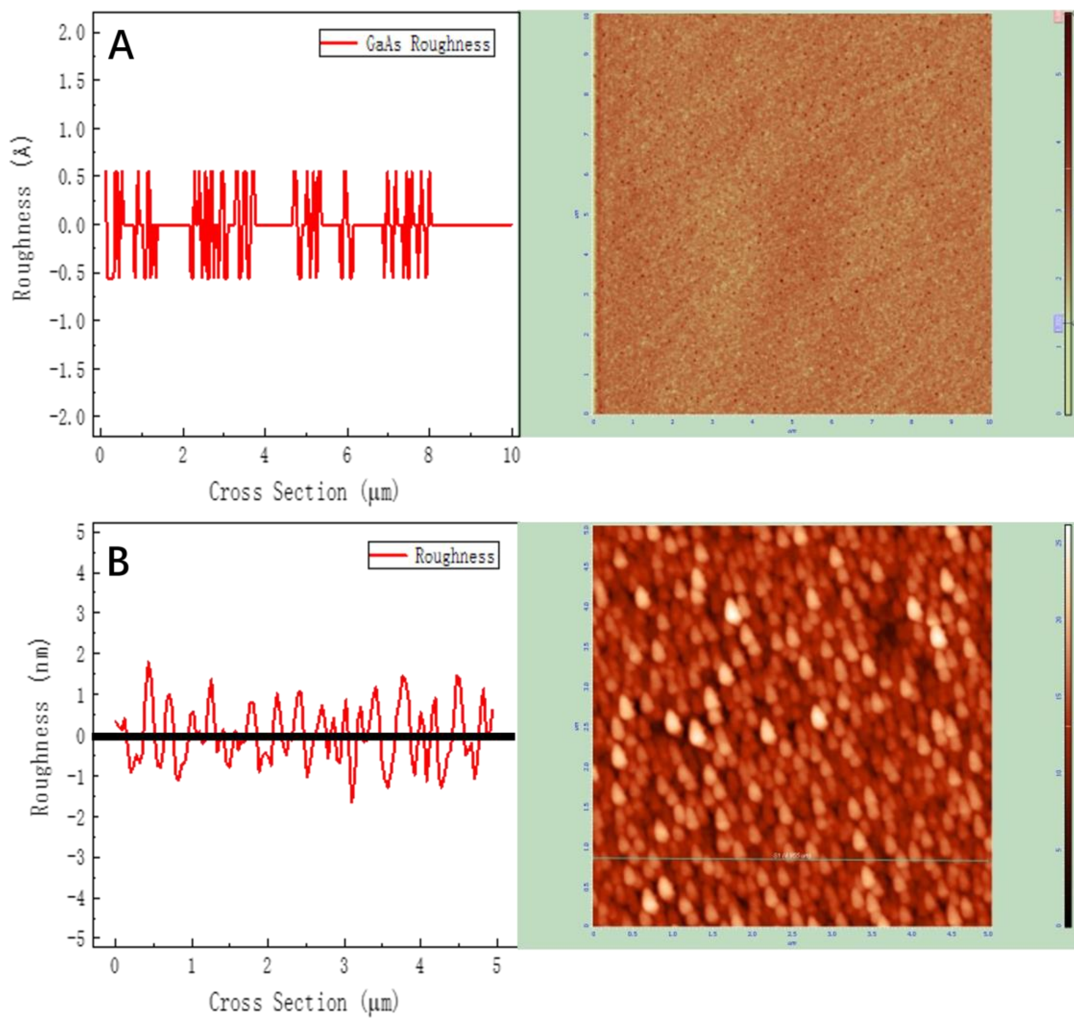

Fig 6.4 the AFM measurement of GaAs substrate and S/GaAs substrate and their corresponding heights. A) the average roughness of S/GaAs with 0.5Å which is the AFM equipment minimum accuracy. B) the S-passivation GaAs roughness under 2nm.

6.6 Summary of Findings

In this part, we have investigated the morphology and elemental composition of sulfur passivation on the GaAs (111) As terminated surface. The results obtained by RHEED images confirmed that sulfur atoms deposition on GaAs as single crystal after low-temperature annealing.

After low temperature annealing, the surface floating sulfur has been evaporated from the sample to measure XPS. The S 2s electrons in XPS measurements are 227.9eV that rarely reported in previous reports of sulfur passivated GaAs, because this value is not easily observed. The smooth single peak S 2s curve shows that sulfur forms a single valence sulfide on the surface of GaAs. for XPS measurement, the penetration depth can reach 10 nm thickness, which not only surface few layers but also part of bulk GaAs can be detected. In XPS measurement, the characteristic peak of S 2p in sulfide ($2p_{3/2}$ 160.5-163.5eV) is very close to that of Ga 3s in GaAs (160eV), and if GaAs is used as substrate, it is not easy to distinguish S 2p from Ga 3s. The XPS measurement of GaAs accords with the characteristic curve of gallium arsenide, which shows that only the surface gallium arsenide bonds with sulfur atoms.

To observe the morphology of passivated GaAs surface, AFM measurement was employed. AFM measurements in Fig. 6.4 show that the morphology of sulfur atoms on GaAs surface is interesting that the size and direction of domain structure are uniform. This domain structure is not found on the clean GaAs substrate, that is to say, due to the effect of chemical potential energy in the passivation process, this domain structure appears in S/GaAs samples. Passivated GaAs surface also indicated that the passivation process is homogenous. Every dangling bonds of substrate surface has homogenous bond energy. Also, the passivation results can optimize the transition metal growth.

The Growth of Single Crystal of Monolayer CoS_2

The growth process of monolayer CoS_2 can be concluded into two parts: sulfide passivation and MBE growth. S-passivation preparation was introduced in the chapter of 4.1. This chapter mainly present the MBE growth part.

In previous studies, to synthesize CoS_2 is by CVD and CVT hence bulk CoS_2 as the main role but not thin films. in this chapter, the growth of single crystal monolayer CoS_2 on the S/GaAs substrate will be detailed introduced. Meanwhile, the monolayer of CoS_2 will be detect by in-situ RHEED, XPS, AFM, TEM and electron transport. These measurements all were taken in Nanjing University.

7.1 Introduction of CoS_2

Many kinds of transition metal dichalcogenides of 3d material MX_2 (X=S, Se, Te) crystalize pyrite structure. This pyrite structure has cubic structure which is NaCl-like grouping transition metal atoms and two dichalcogenides atoms. Because of valence bonds between two X atoms, the distance of two chalcogen atoms is short. The previous studies believe that only under high pressure MX_2 with pyrite structure can be prepared[102, 103]. Cobalt disulfide CoS_2 with pyrite structure is one of most widespread disulfide materials. The family of pyrite structure compound is rather widespread, such as MnS_2, FeS_2, NiS_2, ZnS_2, RuS_2, $CoSe_2$, $CuSe_2$, etc. CoS_2 has prominent position for the catalyst, therefore, the studies of CoS_2 have been hot for these years. The atomic structure of CoS_2 as shown in the Fig.7.1 [45]. The S-S dimer bonds provide CoS_2 a dumbbell structure. As previous researches, the distance of S-S bonds is 2.065Å, which is shortest than that of other pyrite structure materials[102]. Though bulk undoped CoS_2 is half-metallic ferromagnet, with an electron spin polarization of 56%. CoS_2 remains highly spin polarized with a Curie temperature range of 116-120K.

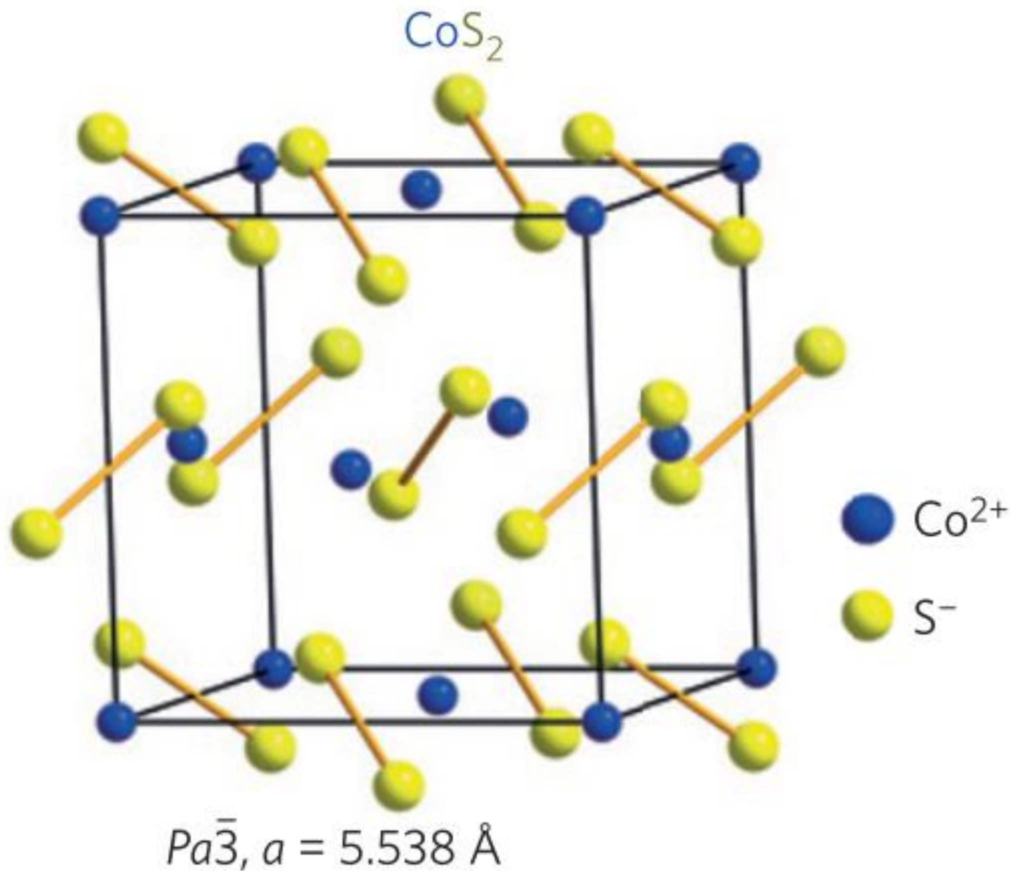

Fig 7.1 the illustration of atomic CoS2 structure with lattice parameter of a 5.538Å [45]. The cubic CoS_2 lattice parameter is 5.538Å.

As the Fig.7.1 shown, cubic CoS_2 crystalline, the lattice constant of CoS_2 is 5.538Å. However, the shown crystalline structure is a unit cell of CoS_2, which that of a single monolayer of CoS_2 has been revealed. From the Fig.6.1, the bottom layer of this unit, 5 atoms of Co^{2+} pair 8 atoms of S_2^{2-}, which is equal to the top layer. While, the middle layer of single unit, there are 4 Co^{2+} atoms and 10 S_2^{2-} atoms.

Therefore, the interesting topic of single layer CoS_2 is confused people due to growth techniques. Also, when the cubic CoS_2 down to one single monolayer, the properties of monolayer CoS_2 whether changes or not is a main task for us. The previous study indicates that the CoPS was prepared from CoS_2[45], which the electric properties has a change cause of different Co valence (Co^{2+} and Co^{3+}) presented in CoS_2 and CoPS respectively.

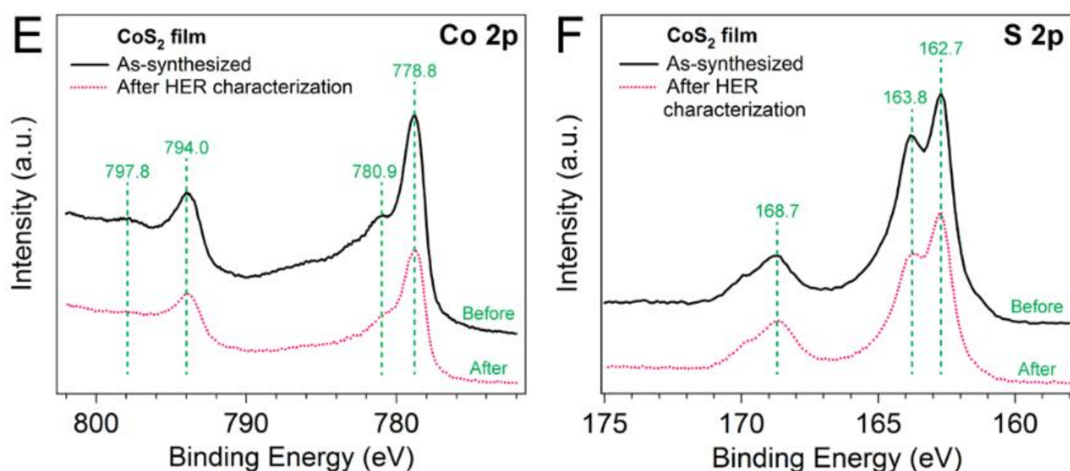

Fig 7.2 X-ray photoelectron spectra of the (E) Co 2p and (F) S 2p regions for as-synthesized (upper black traces) and electrochemically characterized (lower magenta traces) CoS_2 film electrodes[43].

As shown in Fig.7.2, to assess the chemical stability and oxidation states of CoS_2, X-ray photoelectron spectroscopy (XPS) was performed on CoS_2 films on graphite before and after electrochemical characterization[43]. The satellite peaks at 780.9 and 797.8 eV in the Co 2p spectrum (Fig.7.2E), as well as the sulfate peak at 168.7 eV in the S 2p spectrum (Fig.7.2F), indicate that CoS_2 is susceptible to oxidation in air, but these oxide products are removed upon exposure to the H_2SO_4 (aq) electrolyte[43]. The positions and relative intensities of the Co 2p (Fig.7.2E) and S 2p (Fig.7.2F) peaks, which are in good agreement with previous reports[102].

7.2 Sample Growth of Monolayer CoS_2

Monolayer of CoS_2 were grown on the GaAs (111) substrate in ultrahigh vacuum chamber. A 4-inch GaAs (111) B wafer was supplied by AXT company. Firstly, the GaAs wafer was cut into piece of $8mm \times 10mm$ size, which is match the sample holder size. Before transferred into MBE chamber, GaAs substrate was rinsed by acetone and deionized water in order to remove any contaminants. Secondly, the rinsed GaAs was immersed into solution of (H_2SO_4: H_2O_2: $H_2O = 3{:}\,1{:}\,1$) for 49s to remove the oxide layer. All these two steps were performed in a level 100 clean room to protect sample. Then rinsed GaAs was transferred into MBE main chamber with base pressure of 3×10^{-10} mbar. Thirdly, the clean GaAs substrate was heated up to $480℃$ for 60 mins (at annealing pressure of 5×10^{-9} mbar) to remove natural oxides and create flat GaAs (111) B surface. During the annealing process, some break-bonds GaAs atom on the surface were removed. Finally, the annealed GaAs substrate was taken out from vacuum chamber for sulfide passivation. The passivation steps mentioned above, the GaAs was dipped into solution of $(NH_4)_2S_x$ with $60℃$ for 90 mins. After passivation, the substrate was rinsed by deionized water and blown by N_2. After preparation of S/GaAs, the substrate was transferred into main chamber again for CoS_2 growth. An evaporator beam source of cobalt preciously supplies Co atoms onto the S/GaAs substrate with growth temperature of$300℃$. The Co K-cell evaporator will be heated up to $1360℃$, achieving the growth rate of 0.037 Å/s. When the cobalt K-cell source reached $1360℃$, the substrate of S/GaAs (111) was covered by shutter at the first 5min in order to get stable cobalt growth rate. When single layered cobalt layer deposited onto S/GaAs substrate, the shutter blocked the sample stage again. The growth pressure was under $3 \times 10^{-9}\,mbar$. Finally, the sample was annealed to $495℃$ with 50 mins under the environment of $8 \times 10^{-9}\,mbar$. These parameters are selected according to the results of repeated experiments. The temperature parameters are controlled by the combination of Euro surface and thermoelectric coupling. These parameters are also calibrated by infrared detection. The post-annealing procedure, it is

crucial for synthesis of monolayer CoS_2, the covalence bonds of Co-S and S-S bonds were connected during post-annealing process. Therefore, unlike other method of MBE growth, to increase temperature in post annealing should be gradual and slow.

7.3 RHEED Patterns of Monolayer CoS_2

The RHEED monitor was employed since the samples transferred into the main chamber of MBE system. The power supply of in-situ RHEED is 25KV and I_F 1.5 A.

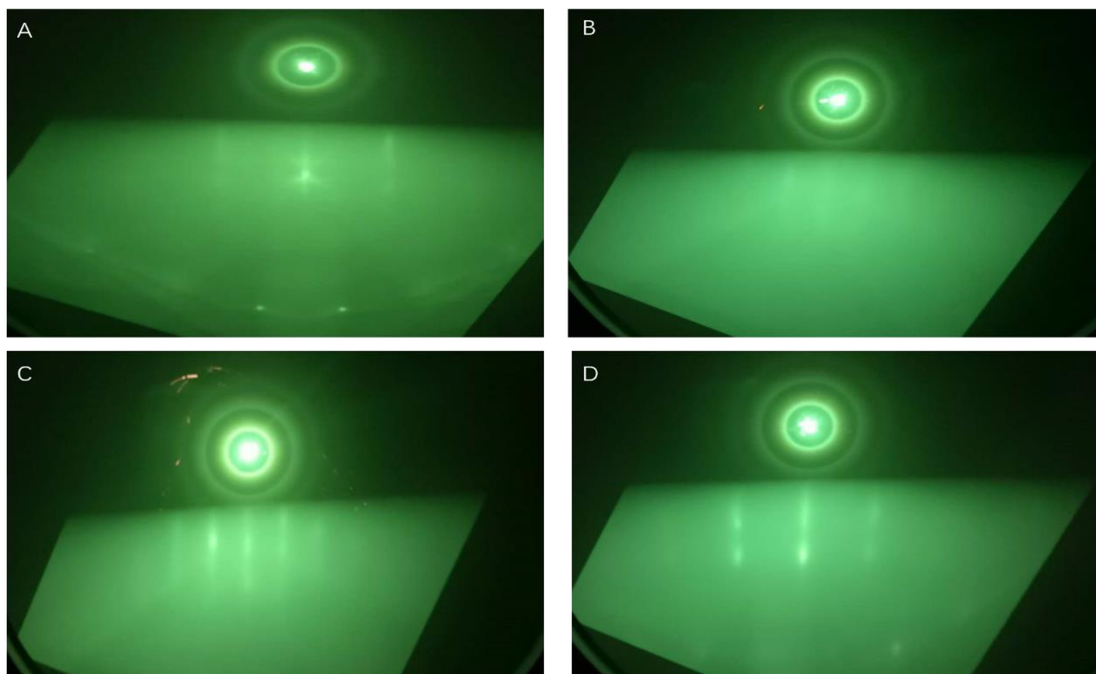

Fig 7.3 in-situ RHEED images during growth of CoS_2. A) the RHEED pattern of S/GaAs from [1 1 -2] crystal orientation. B) RHEED pattern from [1 0 -1] direction after deposition of cobalt atoms. C) RHEED image of monolayer CoS_2 [1 0 -1] after 750K post annealing. D) after post annealing, the CoS_2 patten from [1 1 -2] direction.

After growth of cobalt atoms, the S/GaAs RHEED patterns of disappeared on the screen and new patterns gradual presented. When the sample reached 750K, the CoS_2 patterns appeared.

The prepared S/GaAs substrate had a single crystal structure during the growth of cobalt disulfide from Fig.7.3A. However, after Co atoms grown, the sample becomes amorphous but had an undetectable linear RHEED pattern as shown in Fig.6.3B. Nonetheless, after 750K annealing, clear single crystal stripes appeared, and cobalt

disulfide monolayer can be used to determine the single crystal structure as shown in Fig.7.3C and D.

The RHEED pattern analysis was employed KAS 400 software, which can transfer RHEED strips to Gauss fit plot. From Fig.7.4, single-crystal CoS2 enlarged d-spacing 3.6% from 144 of GaAs (111) to 149, which means the lattice parameter of CoS2 decrease 3.6%. GaAs (111) lattice parameter is 4.0Å, therefore single-crystal CoS2 should be 3.86Å.

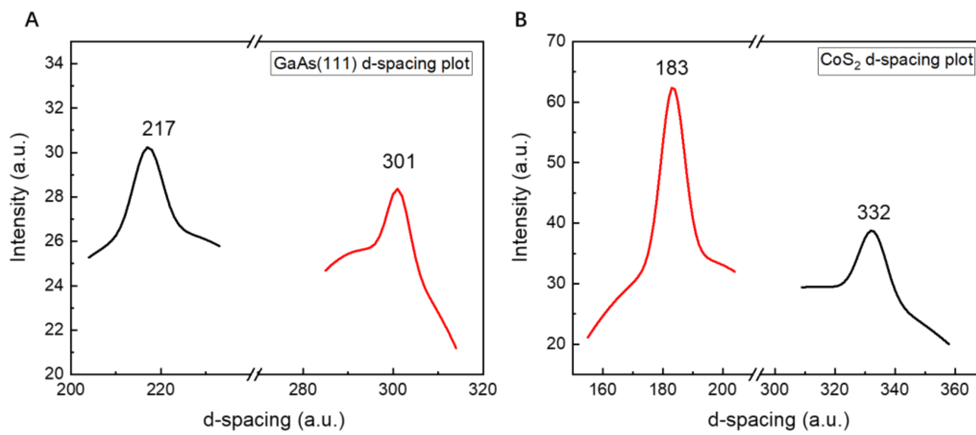

Fig 7.4 In-situ RHEED pattern d-spacing plot of [1 1 -2] crystal orientation: (A) GaAs (111), (B) single-crystal CoS_2.

7.4 XPS Measurement and Analyze of CoS_2

The CoS_2 XPS was detected ex-situ and without any capping layer. CoS_2 as one of hottest materials, the XPS data have been researched deeply. Without capping layer, the Co 2p will present 4 peaks which two of those are cobalt oxide[43].

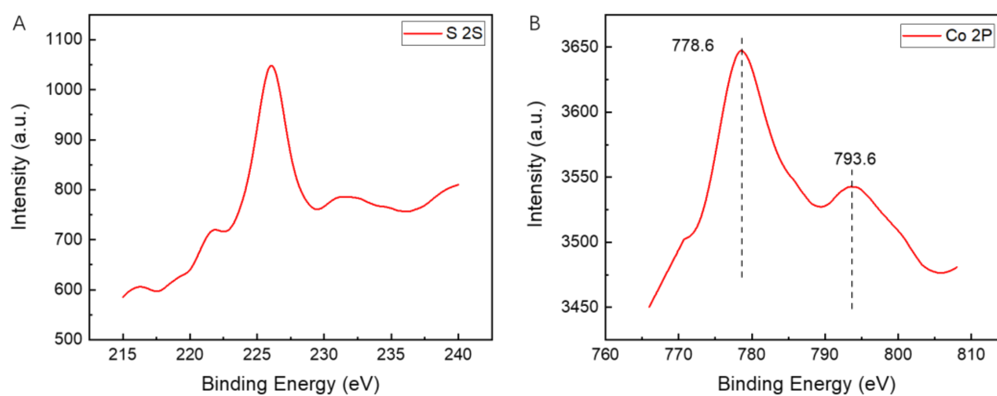

Fig 7.5 the X-ray photoelectron spectroscopy of S 2s and Co 2p from the monolayer cobalt disulfide. (A) the S 2p character peak at 226.4eV. (B) CoS_2 character peak at 778.6 and 793.4ev

To further assess the chemical stability of monolayer of CoS_2, the XPS measurement was performed ex-situ after expose, which proves the chemical robustness of the single-layer film as shown in the Fig.7.4. The position and relative intensities of Co 2p and S 2s electrons are in good agreement with previous studies[102, 104]. The satellite peaks at 778.6 and 793.6 eV in Co 2p (Fig.7.5B) and 226.3eV in S 2s (Fig.7.5A) indicate that CoS_2 is susceptible oxidation after exposure in the air. The sample was taken from the vacuum chamber. After exposure 10 hours, the sample was transferred into vacuum XPS chamber.

7.5 Scanning Electron Microscopy (SEM) Measurement of CoS_2 on GaAs and Analysis

SEM (scanning electron microscopy) is broadly used to detect the samples' morphology and chemical components. SEM measurement under vacuum environment with base pressure of 5×10^{-6} torr, the high-energy electrons beam focus on the surface of samples, and then collecting secondary electrons to present SEM images.

The SEM measurement in this experiment is a commercial SEM made by Zeiss, which the maximum resolution is 0.8nm at 15 KV.

Because of different electrical conductivity between CoS_2 and GaAs substrate, the SEM images present light color for low resistance and dark color for high resistance as shown in Fig.7.6A.

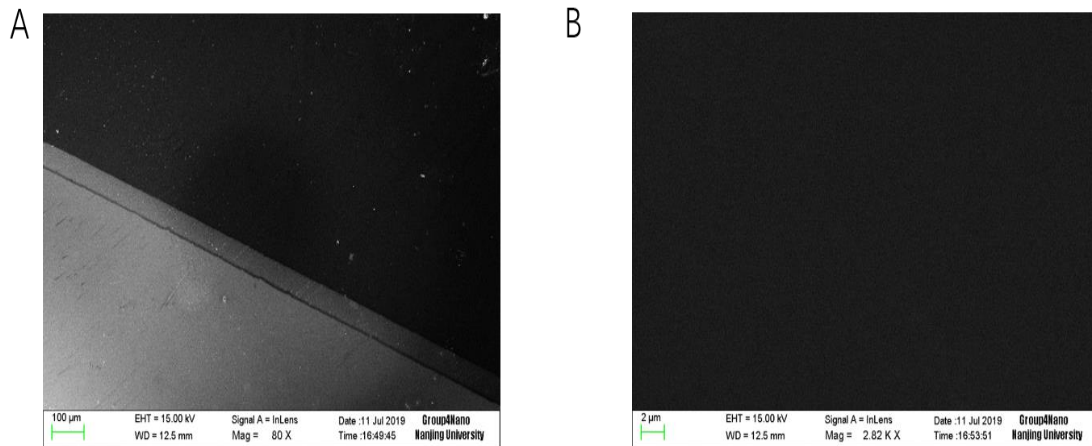

Fig 7.6 passivated method growth of 100% coverage film. A) the SEM image of sample at the boundary between clamp and film which the dark part is the monolayer of CoS_2 and the light part is GaAs substrate. B) the SEM image of the film area.

From Fig.7.6A, the light part was covered by clap of sample holder, therefore there is a boundary between light and dark part. The Fig.7.6B, indicates that the monolayer of CoS_2 covered full substrate of GaAs. Above SEM images can show the 100% coverage of monolayer on the substrate. The magnification of the two SEM images was 80K for

Fig.7.6A and 2.82K for Fig.7.6B, respectively. The scale bar of Fig.7.6A and B was $100\mu m$ and $2\mu m$.

7.6 AFM Measurement of Monolayer CoS_2

Atomic force microscopy (AFM), an analytical instrument, can be used to study the surface structure of solid materials including insulators. It studies the surface structure and properties of materials by detecting the extremely weak atomic interaction between the surface of the sample to be tested and a micro force sensing element. Atomic Force Microscopy is a surface technique widely used for investigating surface morphology and thickness. The AFM image is performed in either contact or tapping mode, using the repulsive Van der Waal force between the atoms at the tip and those of the surface. A laser beam focuses onto the cantilever, and then reflection of the beam from the cantilever is collected by a photodetector consisting of two photodiodes.

The monolayer of CoS_2 was detected the smoothness by ex-situ AFM. The smoothness of as-grown CoS_2 monolayer is flat and homogeneous as shown in Fig.7.7. The roughness in Fig.7.7A is the area average roughness calculated by software. And Fig.7.7B is the roughness of a cross line with length of $5\mu m$. The calculated roughness of $5 \times 5\ \mu m$ area is under ± 1Å. The roughness of cross line is under ± 1.8Å. As shown in the Fig.7.7, the surface of the sample presents a 2D plane, and there is no bulge or pit in the images, which indicates that the surface of the sample is extremely flat.

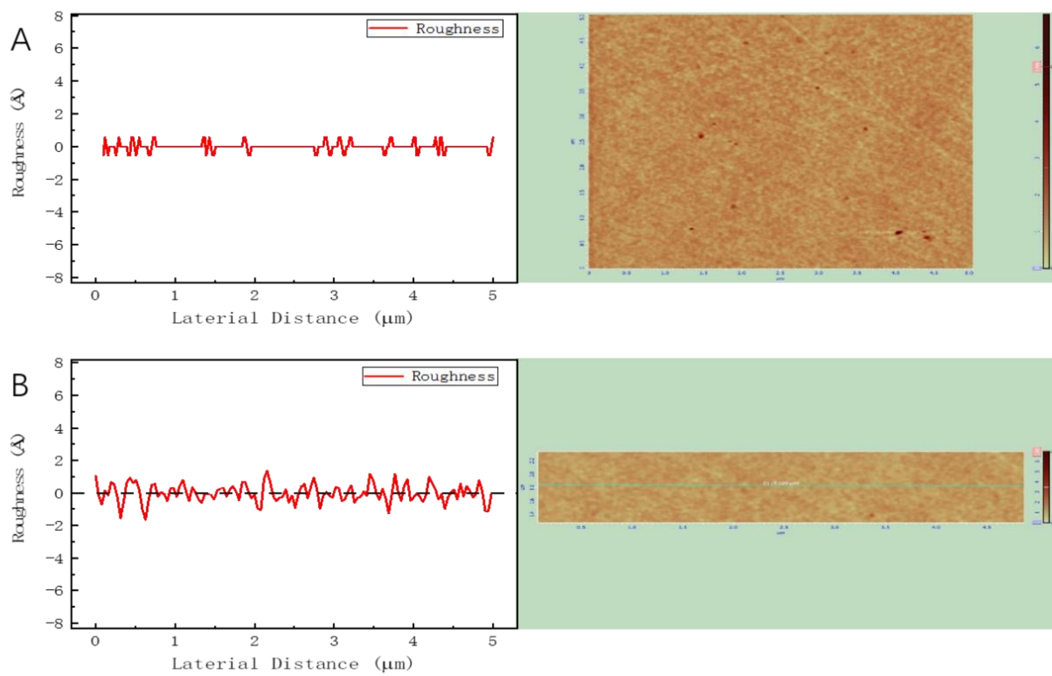

Fig 7.7 atomic force microscopy of CoS_2 monolayer. A) the average roughness of $5 \times 5 \mu m$ area which is under ± 1Å. B) a cross line of the sample with roughness of ± 1.8Å.

7.7 TEM Measurement Result and Analysis

TEM is a large-scale nonanalytic equipment, which uses high-energy electron beam as illumination source to magnify the sample. TEM is a kind of electron optical instrument with high resolution and high magnification. The resolution of TEM is much higher than that of optical microscope, SEM and AFM, which can reach $0.1 - 0.2nm$, and the magnification is tens of thousands to millions of times. Therefore, the transmission electron microscope can be used to observe the fine structure of the sample, and even the structure of the single atomic layer. TEM is an important analytical method in many fields related to physics and biology, such as cancer research, virology, materials science, nanotechnology, semiconductor research and so on.

Structural properties of the grown monolayer of CoS_2 were studied by using commercial TEM (transition electron microscopy). Cross-section TEM specimens were employed traditional method, including mechanical thinning, polishing and Ar ion milling.

Due to oxidation of CoS_2 surface, the sample had capping layer of $3nm$ Al. The TEM image can be observed that monolayer of CoS_2 fully covered the GaAs substrate from as shown in Fig.7.8. The atoms of cobalt disulfide are arranged in order on the GaAs substrate. The capping layer can be seen on the single-layer film of cobalt disulfide.

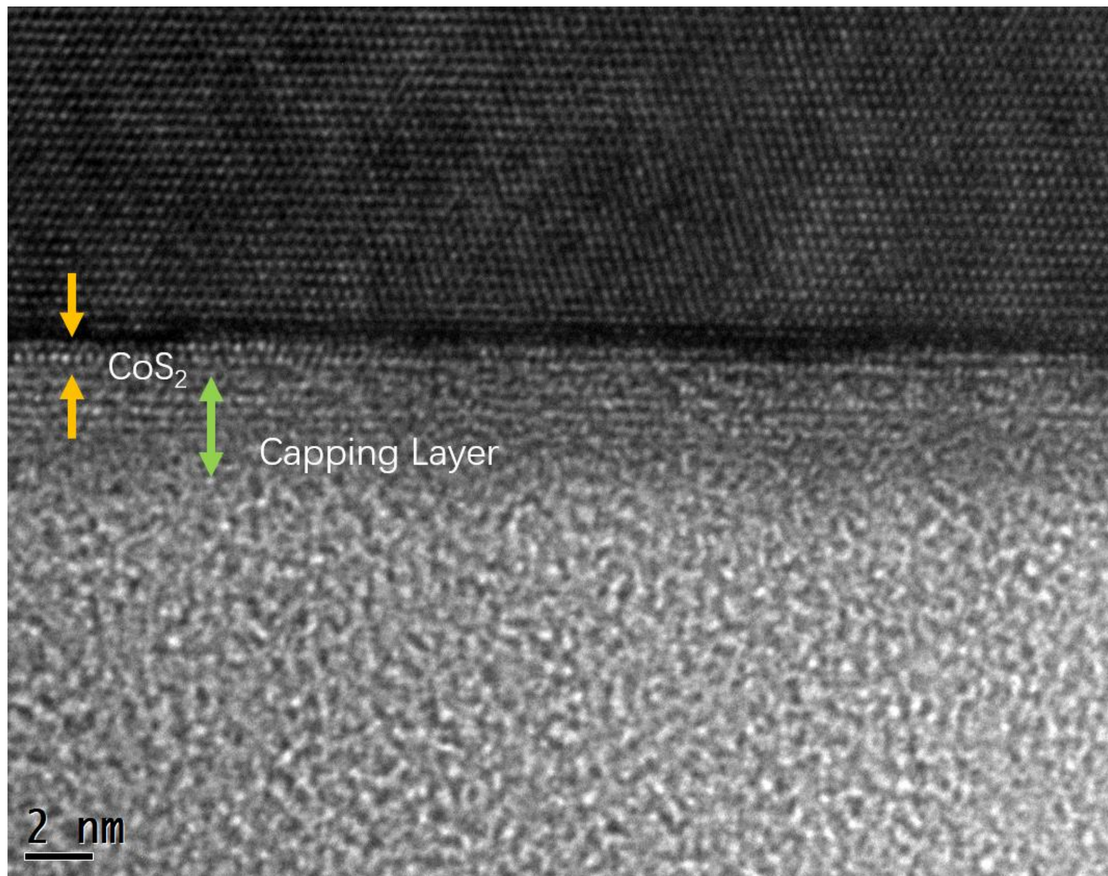

Fig 7.8 cross-section bright-filed scanning TEM micrography of Al (3nm)/ CoS_2 (1ML)/ GaAs (111) in [1 0 -1] crystal orientation. The CoS2 of monolayer can be seen two layers atoms which the lattice constant is larger than GaAs.

In Fig.7.9, the CoS_2 in [1 1 -2] oriental direction, the lattice constant is 3.8Å, which is smaller than that of GaAs substrate. However, larger than that of GaAs substrate, the thickness of monolayer CoS_2 is 8.7Å. Also, as shown in Fig.6.8 the atomic structure of monolayer CoS_2 on GaAs is 1H phase, which is most stable phase for 2D layered materials.

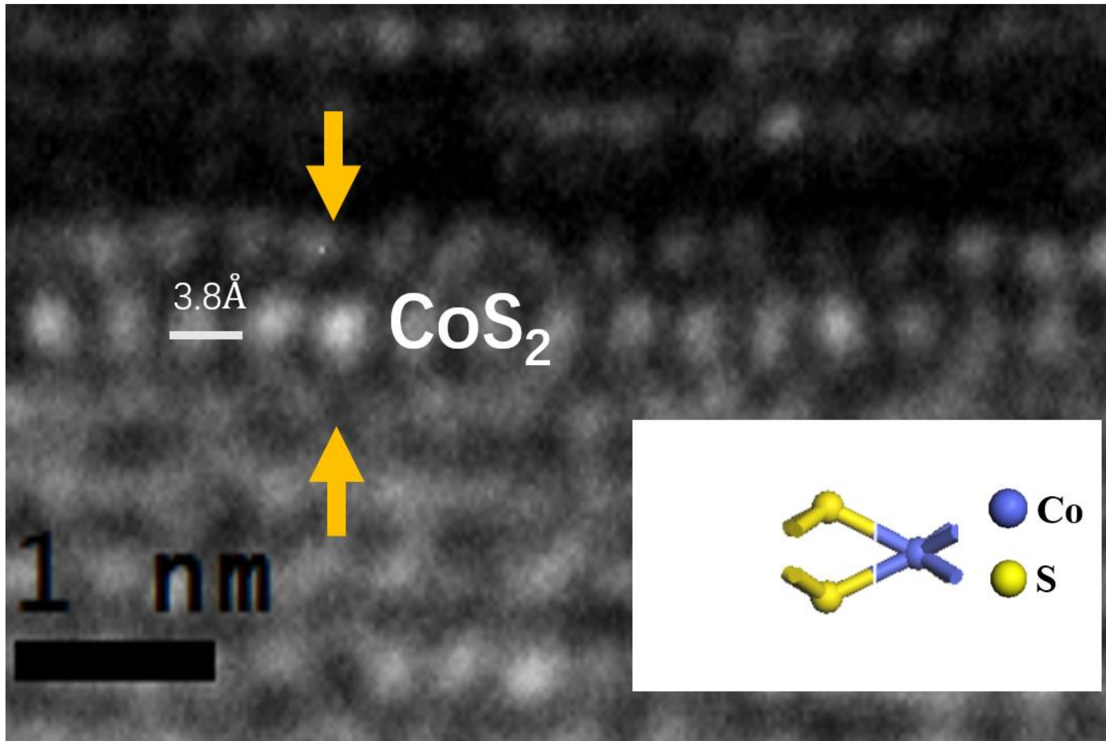

Fig 7.9 the TEM image and its atomic structure diagram of cobalt disulfide. The lattice constant a of monolayer CoS_2 is 3.8Å. The atomic structure indicates the CoS_2 with 2H phase

To further prove the CoS_2 on the GaAs, element analysis is illustrated in Fig.7.10. HAADF-EDS images are to analyze the cross section of sample. The Co and S on the GaAs (111) have been detected in Fig.7.10. This indicates that Co atoms and S atoms together constitute a single layer coated on the gallium arsenide substrate.

Because of the strong background effect, elements of Co and S can be seen in the upper part of the interface and inside the bulk GaAs in Fig 7.10A and B. Similarly, you can see that the top half of Fig.7.10C and D is also signaled by the background of Ga and As. However, these background signals are not true.

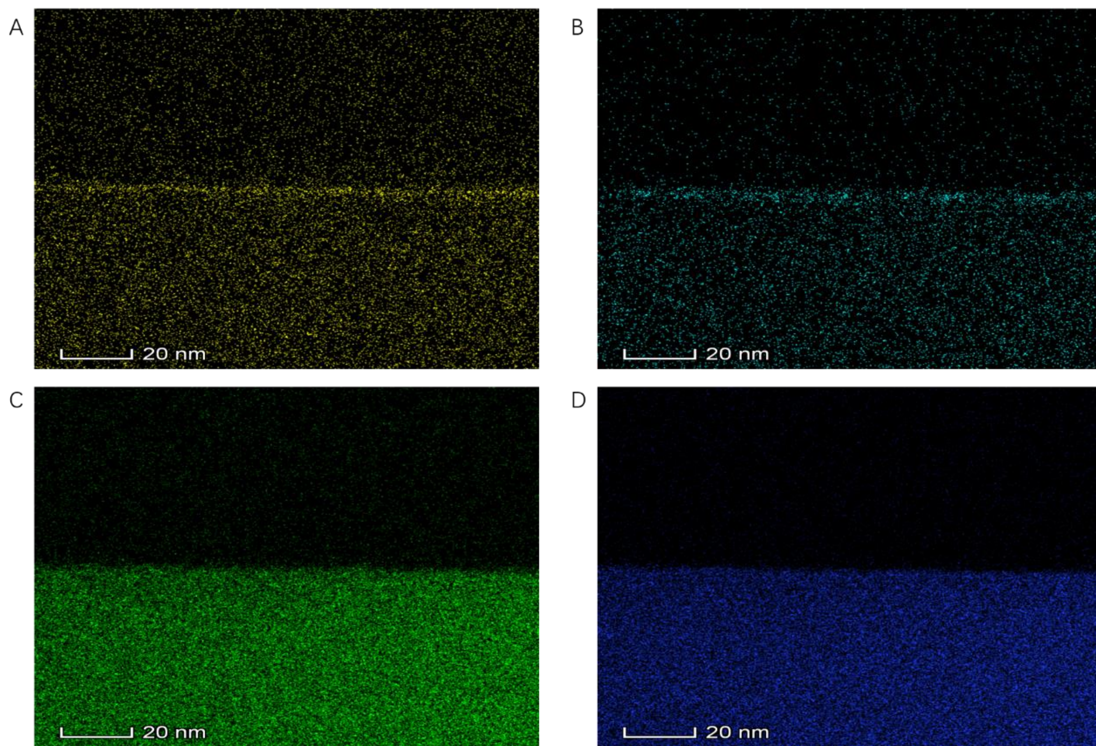

Fig 7.10 HAADF-EDS images of CoS_2 on GaAs. A) HAADF image of Co. B) HAADF of element sulfur. C) and D) the element images of Ga and As respectively.

7.8 I-V measurement of CoS_2/GaAs (111) and Analysis

The monolayer of CoS_2 has much lower conductivity than that of GaAs substrate as shown in Fig.7.11. This is the reason why SEM images present clear boundary.
The I-V curve is to detect the electronic properties of film, which a current is supplied on the sample by the tips. The two tips meanwhile collect the voltage signals.

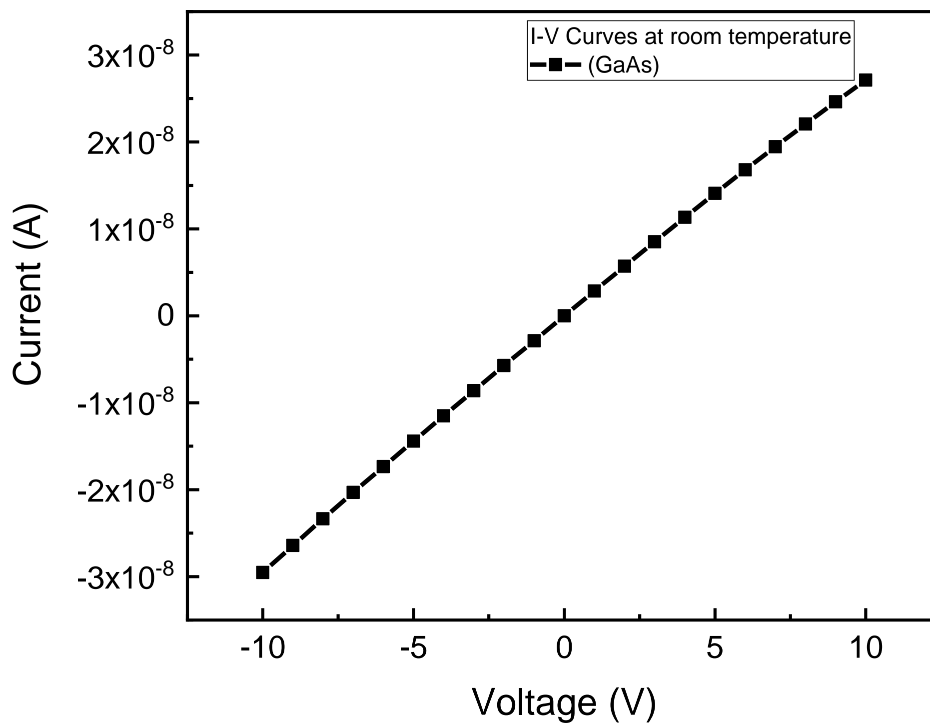

Fig 7.11 the I-V curve of undoped GaAs. (111) at room temperature, which the resistance is $3.7 \times 10^8\,\Omega$.

From Fig 7.11, the I-V curve of GaAs indicates that the resistance of GaAs is around $3.7 \times 10^8\Omega$ at room temperature. The measurement was applied in a commercial I-V probe system.
The application of two-dimensional materials in the next generation of nano electronic devices is very attractive because compared with one-dimensional materials, it is

relatively easy to fabricate complex structures from two-dimensional materials. Single layer CoS_2 is also interesting as a semiconductor analog of graphene, which has no band gap in its original form. The previous chapters reported that the new two-dimensional material CoS_2 had been successfully synthesized by MBE system. For single layer CoS_2 film on undoped GaAs, this structure has more potentials in application in the future. The structure of transistor is illustrated in Fig 7.12.

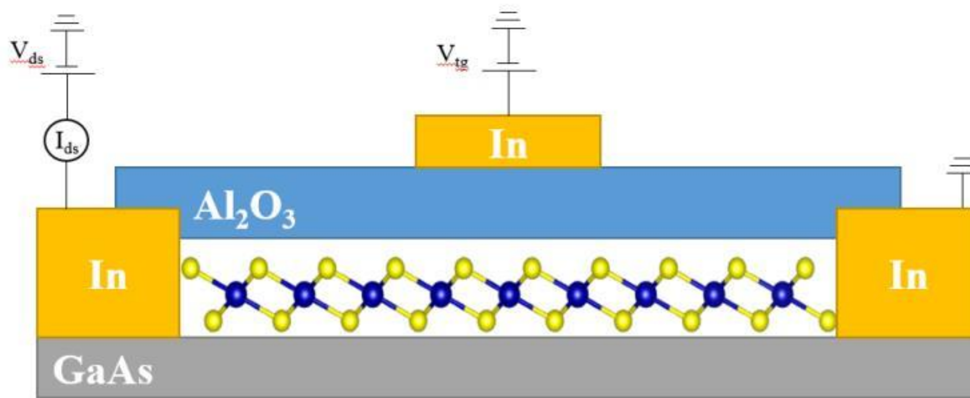

Fig 7.12 the structure of CoS_2/GaAs transistor; the monolayer CoS_2 on GaAs substrate and Al_2O_3 capped on the CoS_2 film; indium as source, drain and top gate electrodes.

The monolayer CoS_2 film was grown in MBE chamber which the growth pressure was 3×10^{-9} mbar. Consequently, the sample was capped by Al_2O_3 in sputter chamber which the growth pressure was 5×10^{-6}. Encouraged by the previous study of MoS_2 transistor [28], we proceed Al_2O_3 with 40 nm thickness, as a high-k gate dielectric for local top gate. We chose Al_2O_3 due to its high dielectric constant of 10-12, which is generally used both research community and industry manufacturers.

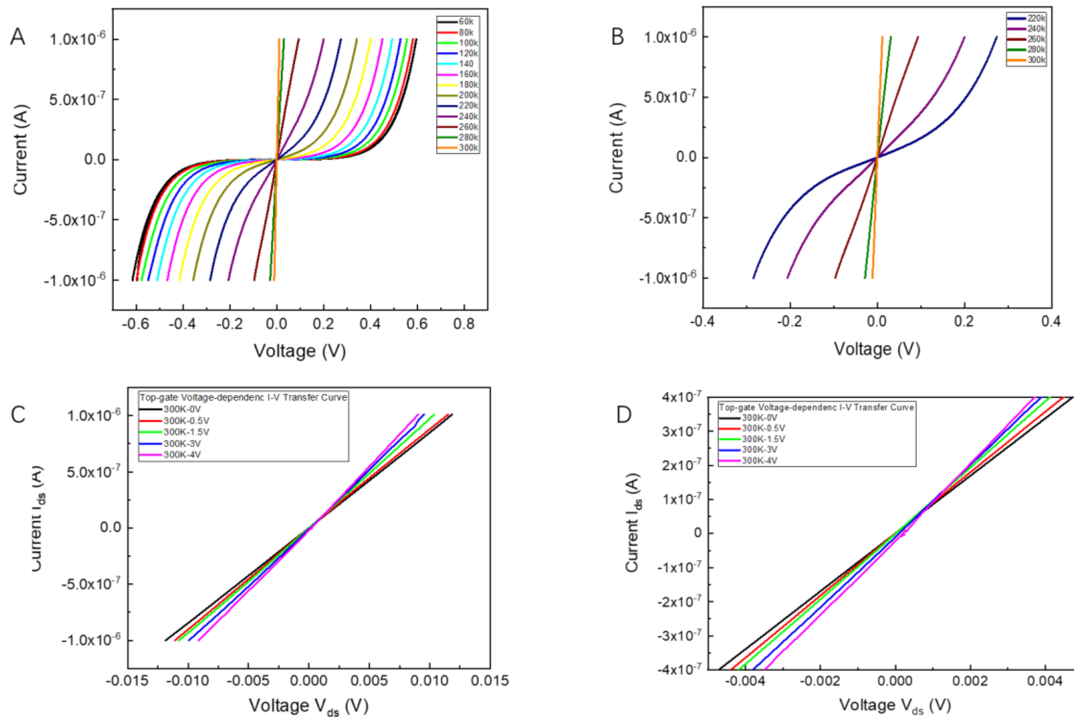

Fig 7.13 the temperature-dependence and gate-voltage CoS_2/undoped GaAs (111) semiconductor. (A) temperature-dependence I-V curve of CoS_2/GaAs from 60K to 300K. (B) the I-V curve from ohmic curve to Schottky curve. (C) tuning gate-voltage of transistor at room temperature. (D) zoom-in the gate-voltage tuning transistor of CoS_2/undoped GaAs.

From the Fig 7.13A and B, the temperature-dependence I-V curve was implemented without gate-voltage tuning. Because of extreme high resistance of undoped GaAs substrate, the resistance could be regarded as the resistance of monolayer CoS_2. At room temperature, the resistance of CoS_2 is $1.2 \times 10^4\Omega$, which is much lower than that of GaAs substrate. When the temperature decrease, the resistance is $3.1 \times 10^4\Omega$ at 280K and $9.4 \times 10^4\Omega$ at 260K. The above three temperatures, the CoS_2 film and indium electrodes represented ohmic contact. However, from 240K to 60K, the contact present Schottky contact.

The Fig 7.13 C and D show the gate-voltage tuning I-V curve of monolayer CoS_2/GaAs sample. When the gate voltage increase, the resistance drop from $1.2 \times 10^4\Omega$ at 0V

of gate voltage to $9.0 \times 10^3 \Omega$ at gate voltage of 4V.

The temperature-dependence and gate-voltage tuning I-V measurement indicate that monolayer CoS_2 is a kind of TMDC semiconductor with low resistance than GaAs. monolayer CoS_2 should has smaller bandgap than undoped GaAs. Comparing with single layer of MoS_2 transistor, the tuning voltage and tuned V_{ds} of monolayer CoS_2 are more sensitive[28] but resistance of monolayer CoS_2 is smaller than MoS_2. Because of its easily tuning property, CoS_2 could be have potential to be next generation semiconductor.

7.9 Antiferromagnetic Monolayer CoS_2 Measurement and Analysis

Antiferromagnetic properties of the grown film were studied using a Quantum Design superconducting quantum interference device (SQUID). The measurement was supported by Prof Du and Mr Liu, department of physics, Nanjing university. Monolayer CoS_2/GaAs sample was prepared in MBE chamber with 3nm Al capping layer, as shown in Fig 7.14. Magnetic field was applied 1000 Oe in perpendicular direction.

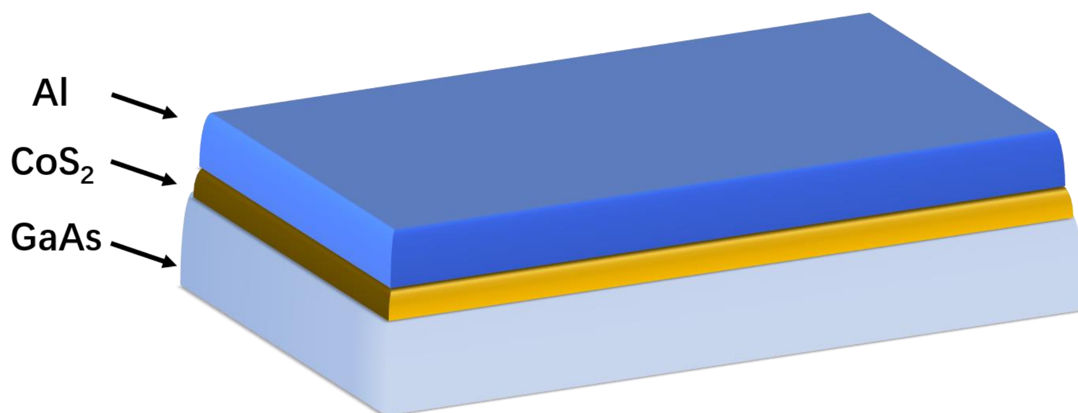

Fig 7.14 the structure of Al/CoS2/GaAs sample, which the Al capping layer thickness is 3nm and CoS_2 is 0.87nm.

Because GaAs is diamagnetic material, the measurement of CoS_2 would not be disturbed by substrate. not only for SQUID measurement, GaAs also is one of ideal substrate for other magnetic measurement[105-107]. Magnetic field was applied in perpendicular direction.

From Fig 7.15, the Al/CoS_2/GaAs sample was measured by SQUID to determine magnetism of monolayer CoS_2. As well known, Al is non-ferromagnetic and GaAs is antiferromagnetic. The sample was measured from 2K to 300K. The FC line and ZFC (red and black) line cross at 82K and then both lines increase slowly, which indicate the Neel point is at 82K. This feature is similar with diamagnetic materials. However, the

moment of CoS_2/GaAs is from -2.14×10^{-5} to -2.09×10^{-5} which is much higher than diamagnetic signal. Inconclusion, this measurement has strong diamagnetic signals and antiferromagnetic features[108, 109]. Because GaAs is a well-known diamagnetic material and Al is a nonmagnetic material, the CoS_2 can be believed that is an antiferromagnetic material, which the Neel point is 82K. Comparing previous studies of 2D materials, there is no antiferromagnetic material so far.

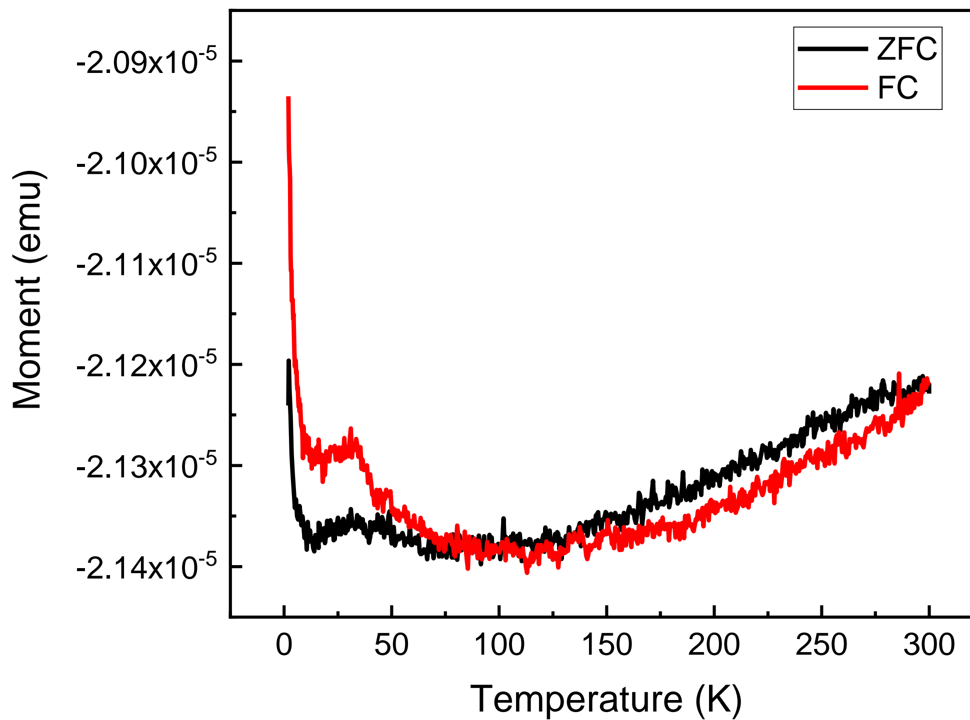

Fig 7.15 FC (Field Cooling) and ZFC (Zero Field Cooling) measurement of monolayer CoS_2 film from 300K to 2K; the antiferromagnetic feature peak at 82K in FC line.

7.10 Results and Analysis of Theoretical Calculation

The theoretical calculation in this project is supported by Mr Li and Dr Lu in Nanjing university. The ab initio package VASP based on density functional theory (DFT) is used in all calculations in this chapter[110, 111]. The lattice constant of CoS_2 is obtained by RHEED image, i.e. a = b = 3.86Å. The Perdew Burke ernzerhof (PBE) function method of generalized gradient approximation (GGA) is used to calculate the electron exchange correlation energy[112]. The real valence electron and valence electron interactions of ions are calculated by the plane projection augmented wave pseudopotential (PAW) method. In reciprocal space, the electron wave function is extended by plane wave basis set. Dft-d2 method is used to calculate the weak van der Waals interaction between adjacent layers. GGA + U method is used to modify the 3d strongly correlated electron interaction of Co atom. After testing, the effective in-situ Coulomb interaction parameter (U) is set at 4.0 eV for Mn atom. Based on the monkhorst pack scheme, the plane wave basis set truncation energy is set to 400 ev. The size of the k-grid in the first Brillouin region is set to $11 \times 11 \times 1$. In the process of structural optimization, all atoms are relaxed until the force on each atom is less than 0.01 eV/S, and the convergence standard of total energy is set at 10^{-6} eV.

The single-layer 1H-CoS_2 crystal structure is shown in Fig. 7.16, which is hexagonal honeycomb structure. Each Co atom forms a coordination with six S atoms, and its lattice constant is a = b = 3.86 Å. The difference of lattice parameter between RHEED pattern and TEM measurement, it is believed because of measurement error.

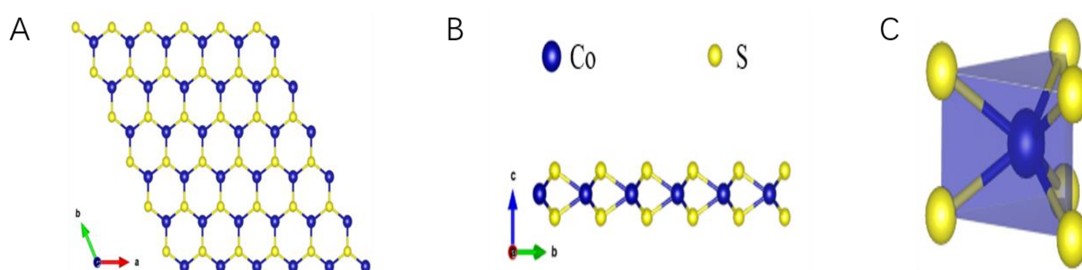

Fig 7.16 Single layer CoS_2 atomic structure: (a) top view, (b) side view, (c) polyhedral coordination

diagram.

In order to study the magnetism of single-layer CoS_2, four kinds of magnetic configurations are considered, including non-magnetic state (nm), ferromagnetic state (FM) and two kinds of antiferromagnetic states (afm1, afm2), as shown in Fig. 7.17.

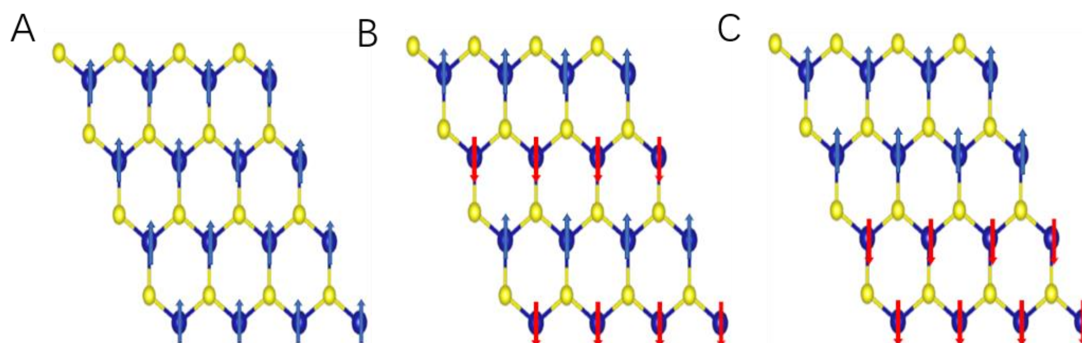

Fig 7.17 The possible magnetic configurations of monolayer CoS_2 are: (a) ferromagnetic configuration FM, (b) antiferromagnetic configuration AFM 1, (c) AFM2. The red arrows are used to indicate the spin down and blue for up.

Because of the rotational symmetry of the single-layer CoS_2 crystal and the spacing between the nearest and next nearest Co atoms, only these two antiferromagnetic configurations need to be considered here, and other antiferromagnetic configurations can be evolved or iterated on this basis. By comparing the energy differences of different magnetic configurations, the lower the energy is, the more stable the corresponding magnetic configuration is, so as to determine the most stable magnetic configuration of single-layer structure.

The energy difference between AFM1(antiferromagnetism1) and NM(non-magnetism), FM, AFM2 is shown in Table 3. It shows that the energy of afm1 is the lowest, which indicates that the monolayer CoS_2 is antiferromagnetic and has no macroscopic magnetic moment.

System	$\Delta E_{NM-AFM1}$ /eV	$\Delta E_{FM-AFM1}$ /meV	$\Delta E_{AFM2-AFM1}$ /meV
CoS_2	12.538	529.314	368.437

Table. 3 The energy difference between AFM1 and NM, FM, AFM2 in the antiferromagnetic configuration of monolayer CoS_2.

Table 4 lists the magnetic moments of each atom and the total magnetic moments of unit cell in the monolayer CoS_2 ground state system. Figure 7.18 shows the spin resolved charge density of the ground state of a single layer of CoS_2.

According to the Fig 7.18 and Table 4, in the single-layer CoS_2, Co atoms have a magnetic moment as high as 2.4 eV, but their spin charge density is positive and negative, and they are antiferromagnetic coupling. S atoms have only a small itinerant magnetic moment, but their spin directions are different. The final magnetic moments cancel each other, and the total magnetic moment per unit cell is 0, which is antiferromagnetic.

System	M_{Co} /μB	M_S /μB	M_{Total} /μB
CoS_2	±2.406	±0.045	0

Table. 4 Magnetic moments of atoms and total magnetic moments of unit cell in monolayer CoS_2 ground state system.

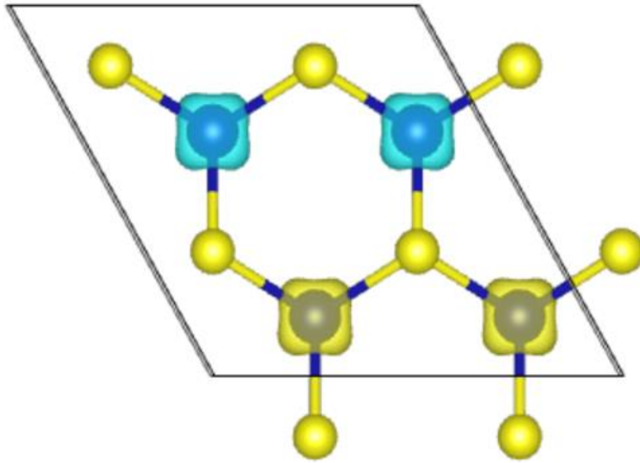

Fig 7.18 Spin resolved charge density map of the ground state of a single layer of CoS_2. The yellow (blue) isosurface represents the positive (negative) spin charge density respectively. The isosurface of spin charge density is 0.04 e/$Å^3$.

The electronic band structure and density of states of single-layer CoS_2 are shown in Fig.7.19, showing indirect band gap semiconductor properties, and the band gap is 1.1eV. According to the density of states up and down of the density of states diagram, it is completely symmetrical, which also verifies that single-layer CoS_2 does not have ferromagnetism.

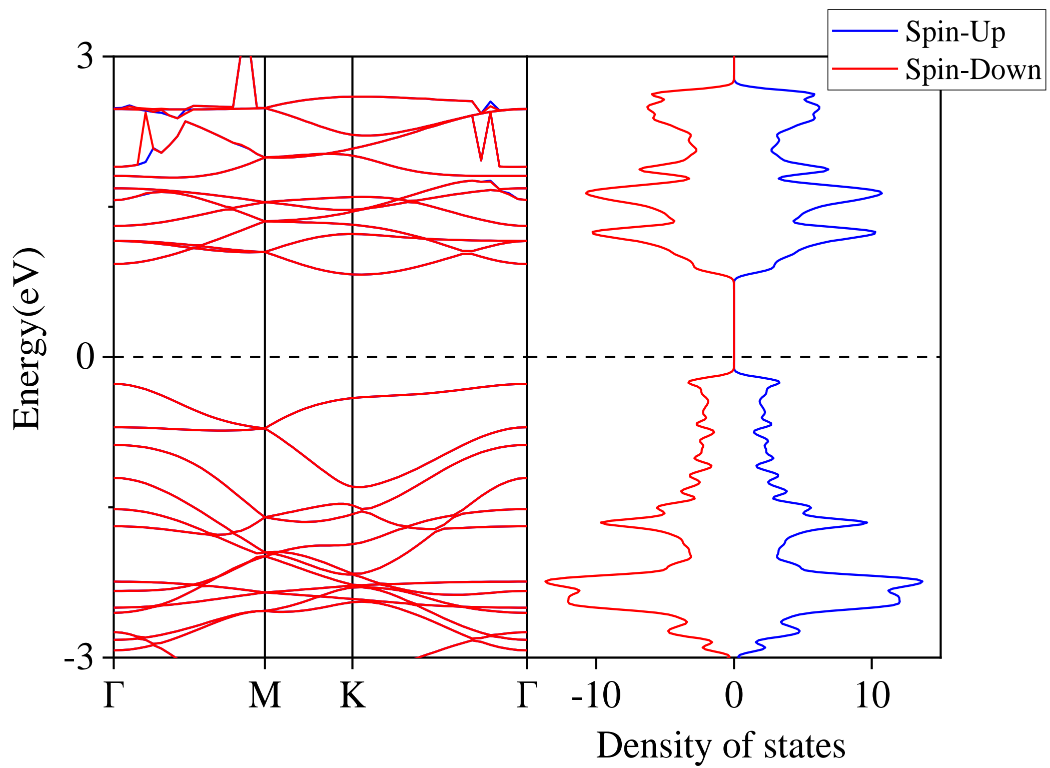

Fig 7.19 The electronic band structure and density of states diagram of single layer CoS_2. The blue (red) lines indicate spin up (spin down) respectively. The Fermi level is 0 eV.

The local density of states (LDOS) diagram of single-layer CoS_2 is shown in Fig.7.20, which further determines the hybridization and density of states distribution of each atomic orbital in single-layer CoS_2.

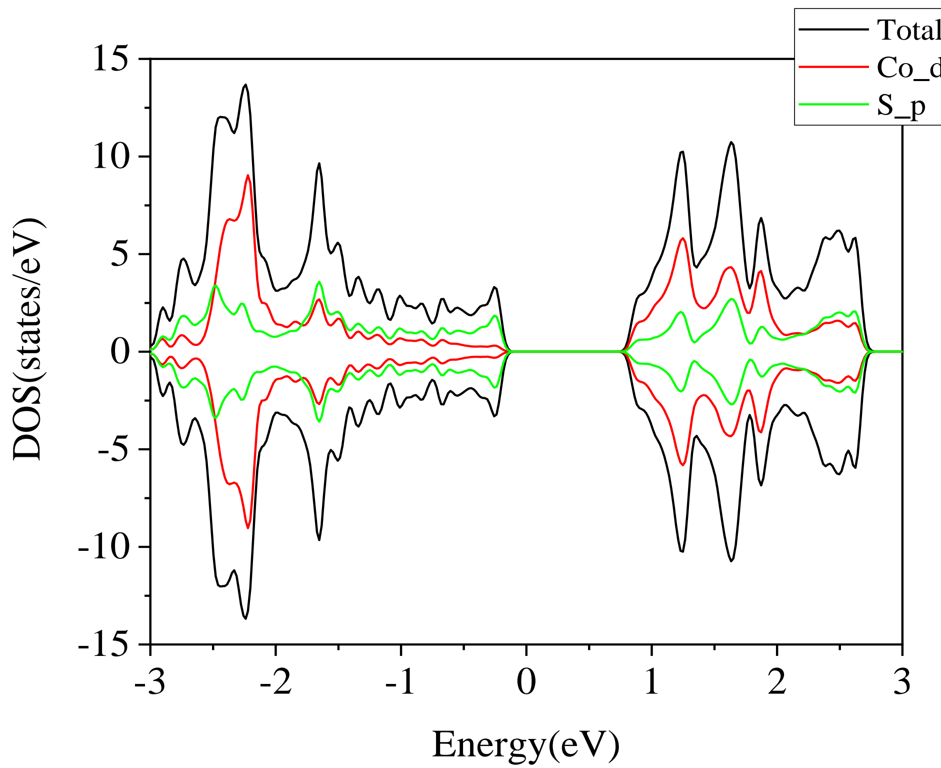

Fig 7.20 The local density of states (LDOS) diagram of single layer CoS_2. The Fermi level is 0 eV.

As shown in the Fig.7.20, near the Fermi level, the density of States is mainly contributed by the p orbital of S atom, and there is no orbital hybridization between the p orbital of S atom and the d orbital of Co atom, which indicates that the super exchange coupling interaction between the ferromagnetism of S atom and Co atom is weak, resulting in the antiferromagnetism of the unit cell. The up and down local density of states of each atom are also completely symmetrical, which indicates that the system is antiferromagnetic.

7.11 Summary of Findings and Discussion

In this chapter, the monolayer of CoS_2 was synthesized on the passivated GaAs (111) by MBE growth, which to prepare passivated GaAs has been introduced in last chapter. The quality of monolayer CoS_2 was proven by in-situ RHEED, XPS, SEM, AFM, TEM, I-V curve measurement and electron transport measurement. the data of these measurement indicate that high-quality, full-coverage, flat, homogenous antiferromagnetic monolayer transition metal disulfide was synthesised.

The RHEED patterns present the process of growth of monolayer single-crystal CoS_2, which the process was from single crystal (substrate) to quasi amorphous (after deposition) and then to single crystal (after post annealing). This process is totally different with previous studies that single-crystal film should be grown on the single-crystal substrate and the dynamic process will not be amorphous situation. After post-annealing process, the lattice parameter of single-crystal CoS_2 was obtained by RHEED pattern and d-spacing, which is 3.86Å (reference with GaAs (111) as 4.0Å). This finding also means that in certain specific circumstances monolayer transition metal disulfide can be self-assembly.

The chemical composition and its chemical properties can be detected by XPS measurement, which is in good agreement of previous studies [43, 102]. Cobalt disulfide monolayer film is a transition metal sulfide which is unstable to oxygen and is prone to oxidation. In addition to the two characteristic peaks of Co 2p (778.6eV and 793.4eV), there are two satellite peaks for oxidation of cobalt disulfide (781.6 and 797.1eV). Similar to Co 2p, S 2s also has a satellite peak of oxidation (222.3eV). Those characteristic peaks and satellite peaks are in good agreement with previous studies[43]. Through SEM measurements at different locations, we verified that this growth method can achieve full substrate coverage. Fully covered cobalt disulfide monolayer films have a clear boundary with the substrate when grown in MBE and can be detected by SEM.

To further assess more microscope morphology of the monolayer CoS_2, we used AFM

to measure the roughness of the film of CoS_2. The average roughness of whole scanning area is less than 1Å, which was calculated by NOVA (analysis software). If a transverse line is selected in the scanning area, its roughness is ±1.8Å. Therefore, we believe that the quality and roughness of single-crystal single-layer cobalt disulfide films are remarkable.

The thickness of monolayer CoS_2 was proven by TEM which also indirectly prove the full coverage. As shown in this chapter, the monolayer CoS_2 completely covered the GaAs (111) substrate. The lattice constant of a can be confirmed, which is 3.8Å. The thickness of monolayer CoS_2 is 8.7Å. HAADF-EDS spectra indicates that the film composed by Co and S elements.

A single layer of cobalt disulfide film can be identified as a semiconductor, and its electrical properties can be derived from the I-V curve. To detect the temperature-dependence I-V curve (without gate voltage), layered CoS_2 should have $1.2 \times 10^4 \Omega$ resistance. The SQUID measurement indicates monolayer CoS_2 present antiferromagnetic properties, which Neel temperature is 30.9K.

In this part of experiment and analysis, we can achieve that a new phase of monolayer CoS_2 film was successfully synthesized on GaAs substrate. The grown film has single crystal, flat, full coverage and homogenous characters. Its properties vary from traditional CoS_2 film, which have antiferromagnetic properties of semiconductor rather than ferromagnetic half-metals[113].

As introduced in chapter 2, firstly, comparing with GaAs substrate, S-passivation GaAs significantly reduce the wetting angle θ, which the Co atoms can homogenously deposit onto substrate rather than nucleation as clusters. Secondly, additional energy caused by surface is decrease due to sulfur passivation. As well known, bond energy of GaAs is much stronger than that of S-Ga and S-As bond. During growth process, growth temperature will break S-As bonds meanwhile keep S-Ga bonds. Thirdly, by passivating sulfur on GaAs substrate and heating up S/GaAs, higher Co-S bond energy can be achieved, which Co-Co bond energy cannot be significantly higher than Co-S. Consequently, these three factors are the reason why S/GaAs is an ideal substrate for

transition metal Co growth.

Because of the new methods to deal with the substrate, an absolute single-layer films can be acheived. Because we use new methods to deal with the substrate, we get absolute single-layer films that others can't get. And this single-layer film can cover the entire substrate. Some previous two-dimensional material growth methods can obtain similar results, but the samples grown with MBE are more homogeneous.[8, 18].

The Growth of Layered 2D Material PtS_2

Growth of 2D layered TMDs by MBE system was researched deeply in 2019 [7, 89]. However, the previous studies cannot meet the need of large-scale films. By sulfur-passivation method, a traditional 2D layered TMDs can totally cover the GaAs substrate. In this chapter, single layer PtS_2 will be taken as an example to introduce the monolayer growth of layered 2D materials. When the PtS_2 was grown in the ultrahigh vacuum chamber that was monitored by in-situ RHEED. In this area, SEM scanning will prove the large-scale films and 100% coverage. AFM measurement will indicate the roughness of film, meanwhile, AFM images also provide the thickness of monolayer PtS_2. The monolayer PtS_2 was detected by XPS measurement as well, which shows the chemical robust of PtS_2. From the data of XPS, AFM and SEM measurement, PtS_2 on GaAs (111) was large-scale, homogenous and stable. The film growth was done in York-Nanjing university joint center. SEM, XPS and AFM measurements were cooperated with electronic department of Nanjing university.

8.1 Background of TMDs Monolayer by MBE System Growth

The development of two-dimensional (2D) materials has opened up possibilities for their application in electronics, optoelectronics and photovoltaics, because they can provide devices with smaller size, higher speed and additional functionalities compared with conventional silicon-based devices[18]. To grow large-scale, high-quality single crystal 2D materials is essential for 2D devices industry. 2D layered transition metal dichalcogenides (TMDCs) have excellent stability, electronic properties and chemical properties which become the hot candidate of new materials of next generation. Last two decades, there were many methods to synthesize layered TMDCs to achieve high-quality surface[8, 36, 55, 70, 90, 114]. These methods include chemical vapor deposition (CVD), chemical vapor transition (CVT), and epitaxial growth. However, the size of single crystal monolayer TMDCs is typically less than 100nm[37, 70, 115]. The main difficulty to synthesize large-scale high-quality monolayer is nucleation process during growth in chamber. For growth of transition metal disulfide materials by MBE, such as MoS_2, PtS_2, WS_2, has more difficulties because of sulfur atoms unstable under ultrahigh vacuum chamber. The nucleation of transition metal disulfide materials require excessive sulfide atoms, which is similar with MX_2 growth ($X = Se\ and\ Te$)[3, 4, 6]. As well known, sulfur sublimation points is quite low at high vacuum circumstance ($10^{-4}\,torr$: 55°C; $10^{-6}\,torr$: 17°C; $10^{-8} torr$: −10°C), resulting in infeasibly equipping in ultrahigh vacuum chamber with base pressure level of $10^{-10}\,mbar$. In MBE chamber, the low sublimation point of S will contaminate chamber, K-cell sources, e-beam sources, and RHEED screen. Therefore, it is infeasible to take sulfur powder as supplement of S in the growth of transition metal disulfide. To solve supplement of sulfide atoms is a tough task for researchers.

Until recently, MBE growth of layered TMDCs was firstly reported which FeS_2 was taken as supply of sulfur[7]. Due to FeS_2 will break bonds of Fe-S and supply sufficient S atoms when FeS_2 was heated up to around 500°C[7]. Moreover, when the sulfide

atoms were evaporated at 500℃, iron atoms will not be sublimated due to high sublimation point of iron (above 1100℃ in vacuum). The Mo atoms was evaporated by a e-beam source onto graphene/Ir (111) under excessive S circumstance. After co-growth of MoS_2, the system was annealed to 1050K in the same S background.

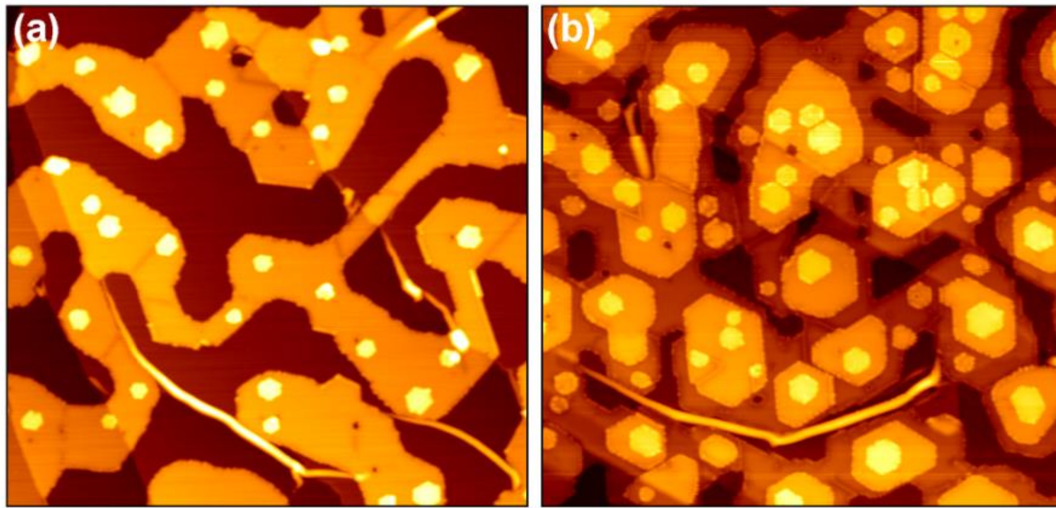

Fig 8.1 constant current STM topography of MoS_2 on Gr/Ir (111). (a) MoS_2 coverage of 0.6 layers. (b) MoS_2 coverage of 1.4 layers. Small areas of exposed Gr are visible. The TL forms islands of ≈20 nm diameter. Gr wrinkles are visible in the lower section in both typographs. STM parameters: (a) V = 1.5V, I = 0.01 nA; (b) V = 1.0V, I = 0.08 nA; each image size is 200 × 190 nm^2[70].

An overview of Fig.8.1, the thin film MoS_2 was grown on the substrate Gr/Ir (111) by MBE growth with base pressure of $5 \times 10^{-10}\ mbar$ and annealing background pressure of $2 \times 10^{-9}\ mbar$. 0.6 layer and 1.4 layer was presented in the Fig.8.1a and b respectively, which both these two samples cannot fully cover the substrates. As shown in Fig. 8.1a, MoS_2 coverage with 0.6 layers presented a network of monolayer MoS_2 film, crossing several Ir step edges. Some small bilayer MoS_2 island can be seen on monolayer films, which the island diameter is around $10nm$. It is apparent from the Fig.8.1b that some decorations of trilayer, bilayer and monolayer MoS_2 exhibited. These results of two thickness suggest that MBE growth for monolayer MoS_2 is difficult to achieve large-scale and homogeneous film.

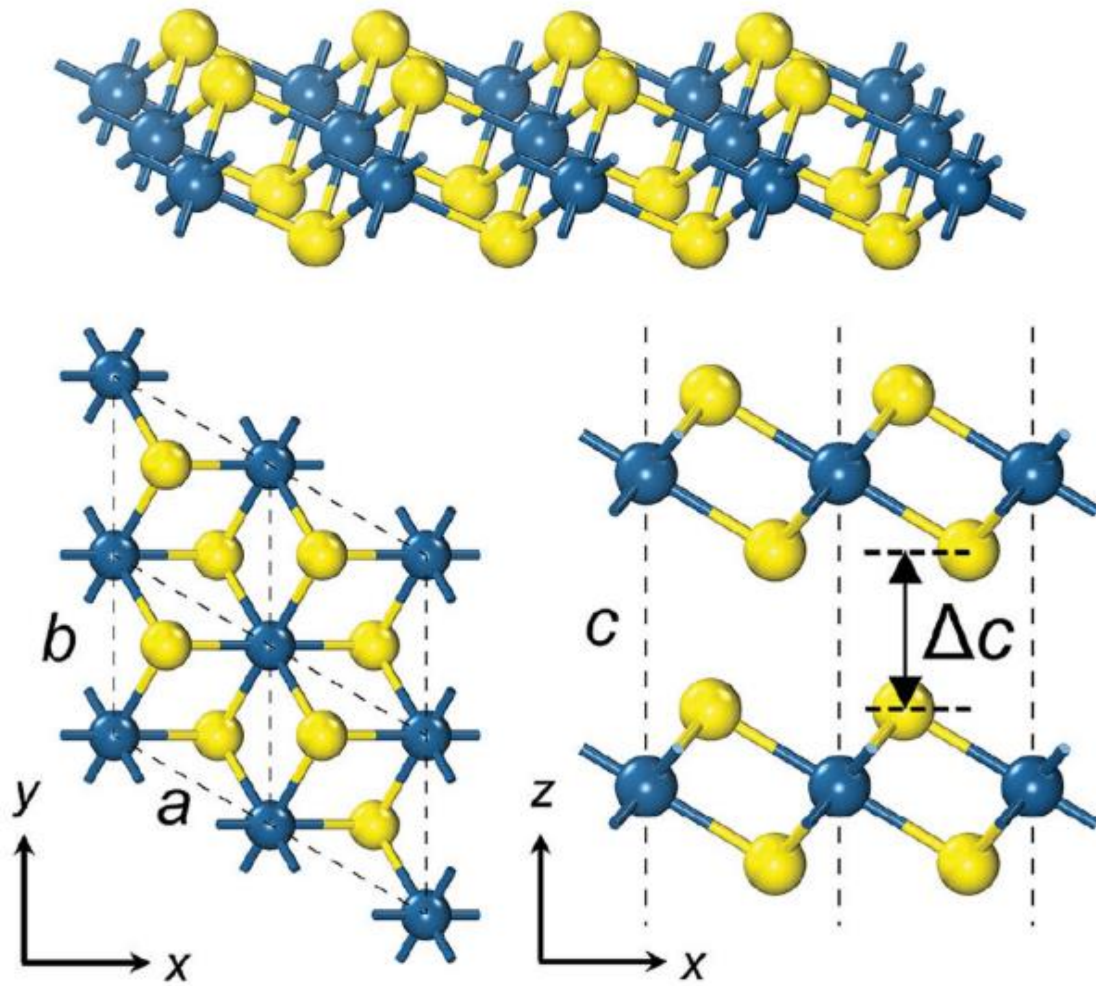

Fig 8.2 schematic drawing of crystal structure of PtS_2 in 3D, top- and side-views. Blue balls represent Pt atoms and S atoms are presented by yellow balls[116].

Fig 8.2 shows the schematic top- and side-views of atomic structures of bilayer (2L) PtS_2 after full relaxation. Each Pt atom is in a tilted octahedral site coordinated by six S atoms. The intralayer [a (b)] and interlayer (c and Δ c) lattice constants of the hexagonal structure are defined in Fig.8.2[116].

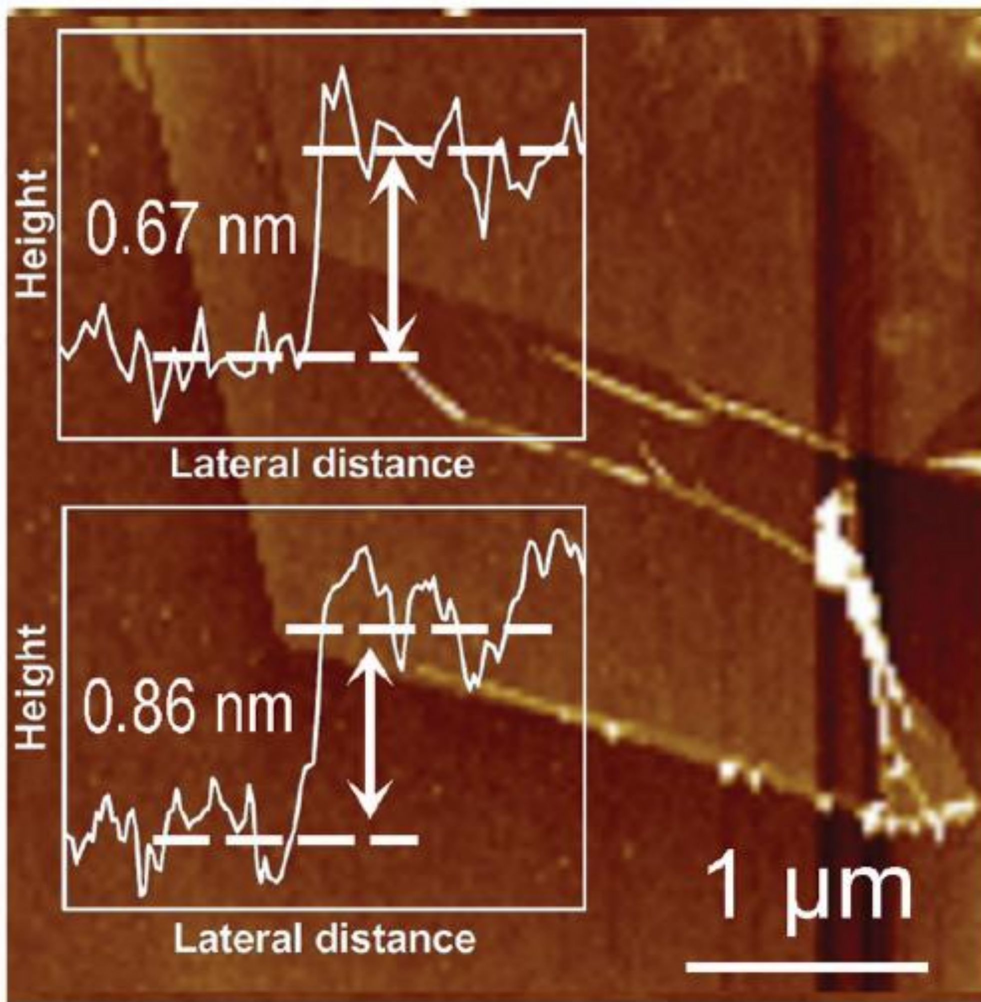

Fig 8.3 atomic force microscopy (AFM) image of the flakes of the exfoliated PtS_2 film[116].

Fig.8.3 shows the absolute height of 8.6 Å between monolayer film and substrate, and the height difference of 6.7 Å between sections (I) and (II). Although the measured thickness is slightly larger than the previously reported value of a single layer (5.03 Å) in bulk crystal[116].

It can be seen from previous reports that MBE system has not been used in the preparation of PtS_2 or other two-dimensional single-layer films, and no large area of high-quality single-layer films have been obtained.

8.2 Growth of PtS_2

A commercial GaAs wafer was supplied by AXT company. The GaAs wafer was cut into substrate with $10 \times 8\,mm$ size which match molecular beam epitaxy (MBE) sample holder. The GaAs preparation was same with monolayer CoS_2 growth. The substrate was rinsed by acetone and deionized water, then etched by mixed solution (H_2SO_4: H_2O_2: $H_2O = 3:1:1$). Finally, the substrate was rinsed by deionized water and blown by N_2. As-prepared GaAs was transferred into MBE chamber for 1-hour annealing which the temperature was 480℃ for cleaning and flatten the surface. The flat GaAs (111) B was taken out from MBE chamber, and then it is treated by $(NH)_2S_x$ solution to achieve homogenous S/GaAs (111) B. Annealing the S/GaAs with 230℃ is to remove any contamination which is on the surface.

Platinum was evaporated by an electron-beam (e-beam) source, because of its high sublimation point. The Pt sublimation point is 1747℃ at 10^{-4} torr and 1492℃ at 10^{-4} torr. The e-beam source was supplied by a current supply and a high-voltage power supply. The supplied current and voltage were 4.1 A and 980V. The emission current from tip of platinum rod is 32.3 to 33 mA. Hence, the supplied power on the tip of Pt rod was 31.7-32.3 W. The growth rate of platinum cannot be calibrated, because sublimation point and melting point is close. We defined the RHEED patterns to calibrate platinum growth rate. As well known, penetration depth of RHEED emission electrons (voltage=25 KV) is 5Å. Therefore, when 5Å Pt were grown onto substrate and RHEED pattern was totally disappeared, the growth time was 72 mins. The growth of monolayer Pt (2.78Å) should be 40 mins. During the growth of Pt, the substrate temperature was 260℃. Once one monolayer Pt growth, the system annealed to 480℃ for 60 mins at $9 \times 10^{-9}\,mbar$. In spite of PtS_2 is strong resistance oxidation, the sample do not need capping layer any more.

For the MBE growth of Pt, the melting point and sublimation point of Pt are very close, so the growth rate should be reduced as much as possible. If the growth rate is too fast, the Pt rod will melt and the film will grow unevenly.

A target to synthesize layered transition metal disulfide by MBE growth was used to

rely on FeS_2 as sulfur source, however, a monolayer of layered PtS_2 was grown in MBE chamber by S-passivation method.

8.3 RHEED Patterns of PtS_2 and Analyses

Once the substrates or samples are loaded into MBE main chamber, the most effective for examine the quality and morphology of films is from the RHEED screen. There are many merits of RHEED, such as in-situ, fast and surface sensitive. The MBE main chamber equips an electron gun with high energy (maximum voltage 25kV), emitting an electron beam. This electron beam impinges upon the surface of samples at an angle of $1°$, and is diffracted on the fluorescent screen. By the reflective electron beam, the details and information of the surface can be observed from the fluorescent screen.

Fig.8.4 presents RHEED patterns of monolayer PtS_2 growth process that is from S/GaAs substrate to final PtS_2 monolayer growth. The substrate was clean and flat by etching and annealing process. The clean substrate of GaAs (111) B was passivated by $(NH_4)_2S_2$ solution is presented in Fig.8.4A. Since the S/GaAs was loaded into main chamber, the system was heated to $230℃$ to degas and clean S/GaAs. It is clear seen from the Fig.8.4A that single crystal of S/GaAs was achieved. As shown in Fig.8.4B, the single-crystal RHEED pattern of substrate had disappeared when Pt atoms were grown onto S/GaAs. However, even though the Pt on the surface was near amorphous, some unclear spots of substrate with $230℃$ were presented on the screen.

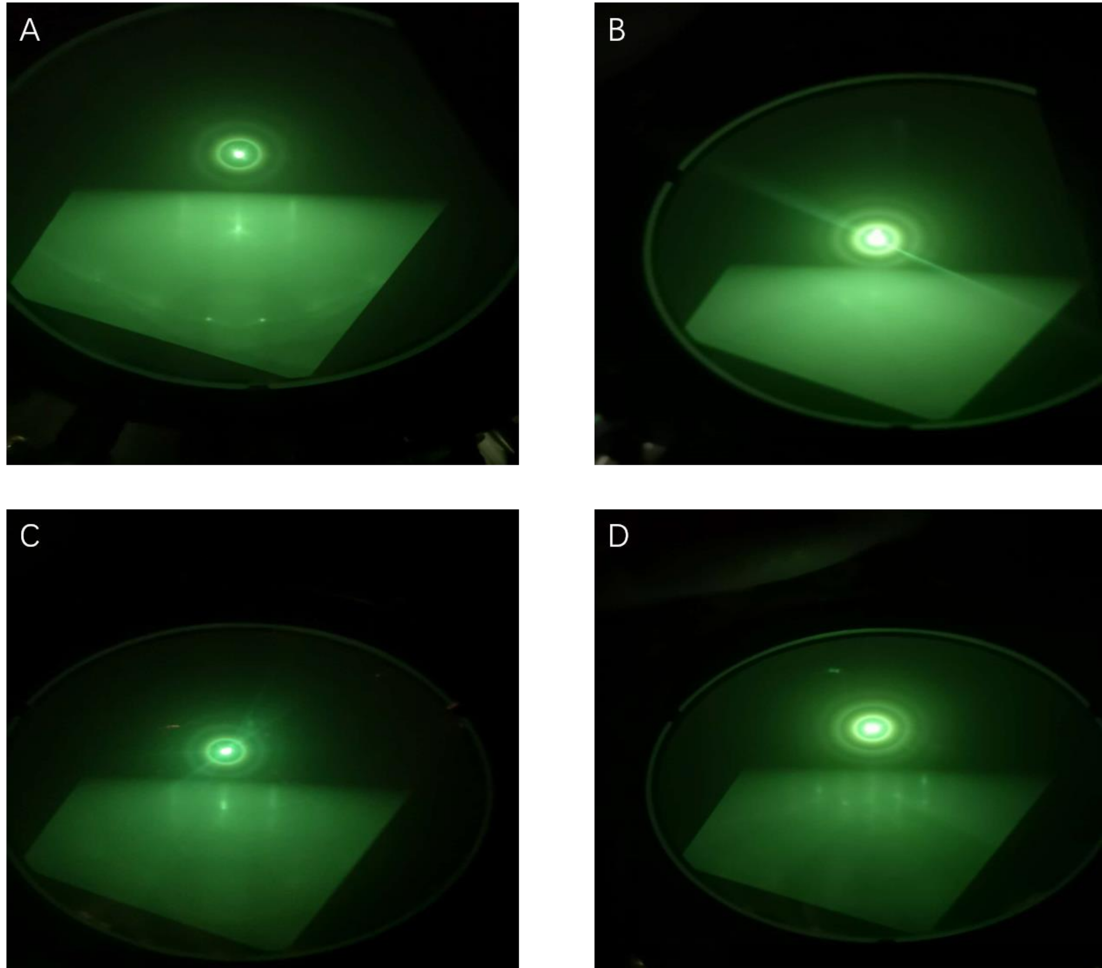

Fig 8.4 presents the RHEED patterns of PtS_2 growth on GaAs. (A) the passivated S/GaAs (111) substrate from crystal orientation of [1 1 -2]. (B) the disappeared RHEED from [1 1 -2] after 1 ML Pt growth. (C) after post annealing at 480℃ for 60 mins. (D) the PtS_2 monolayer film from the orientation of [1 0 -1].

It is apparent from the Fig.8.4C that single-crystal monolayer PtS_2 was synthesized on the surface of S/GaAs with the lattice orientation of [1 1 -2]. As Fig. 8.4D shows, there is a significant single-crystal strips of PtS_2 on the fluorescent screen from crystal orientation of [1 0 -1]. In York-Nanjing university joint center, MBE system is equipped RHEED gun with 15kV supplement, which the maximum of penetration depth basically is 5Å. Lattice mismatch does not obstruct the structure formation of single-crystal PtS_2 monolayer on the GaAs (111). The reported lattice constant of monolayer PtS_2 in experiment growth is 3.54Å[116], which is a large mismatch with GaAs (111) substrate. Nonetheless, layered PtS_2 can be grown on GaAs due to Van der Waals force between

layered PtS_2 and cubic GaAs. Therefore, freestanding monolayer PtS_2 can be formed on GaAs substrate.

Even Van der Waal connection can provide the possibility that structure formation of huge mismatch between substrates and thin films, it is required same orientation between substrates and films. in this growth, the GaAs (111) B and PtS_2 have same triangle surface construction. According previous experience, layered transition metal dichalcogenides with triangle shape cannot be formed on the GaAs (100) surface that is quadrangle construction on the surface.

8.4 XPS Measurement of PtS_2/GaAs

X-ray Photoelectron Spectroscopy (XPS), also known as Electron Spectroscopy in chemical analysis is a kind of diffusely used technique to investigate the chemical composition of surfaces. The XPS instrument measures the kinetic energy of all collected electrons. The electron signal includes contributions from both photoelectron and Auger electron lines. XPS is one of most effective measurement to investigate chemical composition of layered 2D materials.

Due to strong resistance of oxidation, the sample was not capped protected layer. The most sensitive peaks of Pt are 4f that have two peaks due to spin-orbital coupling effects. As shown in Fig.8.5A, there are two peaks of 72.4 eV and 75.7 eV that represent $4f_{7/2}$ and $4f_{5/2}$ respectively. From Fig.8.5A, there is single valence of Pt^{4+} formation on the GaAs substrate due to two smooth peaks obtained. It can be seen from Fig.8.5B that S 2s character peak is 226.9 eV. The single peak of 226.9 eV indicates that S was not oxidized in the air. For XPS measurement of sulfur, the most sensitive electron is S 2p electron, however, the binding energy of S 2p is similar with Ga 3s at 160 eV. Hence, it was performed multiple peaks simulation to analyses S 2p and G 3s, as presented in Fig.8.5C. By fitting data of multiple peaks, the $S2p_{3/2}$ and $S2p_{1/2}$ are 159.9 eV and 161.5 eV. Fig.8.5D provides the general view of XPS measurement of PtS_2/GaAs.

In conclusion, both Pt and S measurement show that single valence Pt and S exist in the system. This feature indicates that only single-phase material formed in MBE chamber. Moreover, because of ex-situ measurement of PtS_2 film, single phase of PtS_2 reveals that PtS_2 has strong resistance of oxidation in the air.

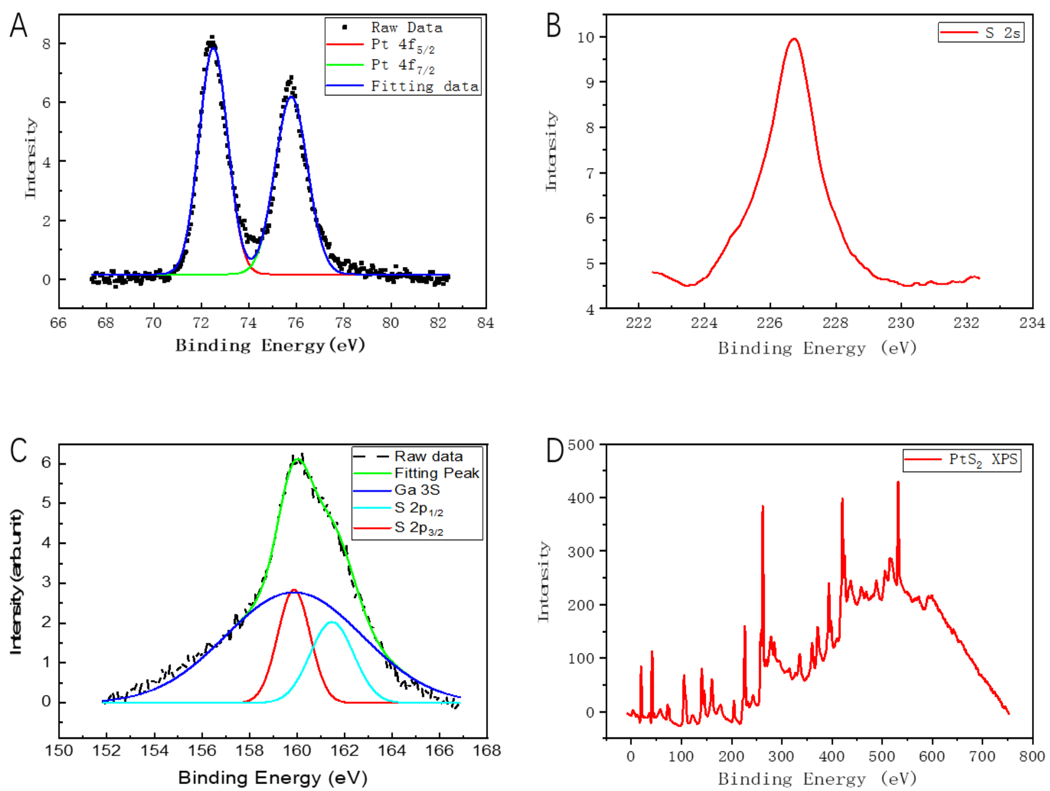

Fig 8.5 X-ray photoelectron spectroscopy of monolayer PtS_2. (A) the character peaks of $4f_{7/2}$ and $4f_{5/2}$ at 72.4 eV and 75.7 eV. (B) the S2s character peak of PtS_2 at 226.76 eV. (C) Ga3s and S2p peaks around 160 eV. (D) the overview XPS of PtS_2.

8.5 SEM Measurement of Full Coverage PtS_2

The scanning electron microscopy (SEM) is used to observe the surface morphology of the sample by detecting secondary electrons. Secondary electrons are scanning the sample with a very narrow electron beam, which produces various effects through the interaction between the electron beam and the sample. The SEM measurement was performed in electric engineering department of Nanjing university. The SEM instrument was equipped vacuum pumps in order to keep base pressure of $5 \times 10^{-6}\ torr$.

Single-crystal PtS_2 on GaAs (111) was studied ex-situ. From Fig.7.6A, it is clear to obtained that an obvious boundary between PtS_2 film and covered area by clamps. Because of different electrical conductivity, the orange line is the stage between PtS_2 film and GaAs substrate, which dark part is PtS_2 film and light part is GaAs substrate. Fig.8.6B, C and D present the SEM images of PtS_2 film with different scale bar. From SEM images, the PtS_2 film grown by S-passivation method is homogenous and 100% coverage, which the substrate is $10 \times 8\ mm$ size. From Fig.8.6 we can see that no any domains on the surface, supporting that the film is homogenous and flat.

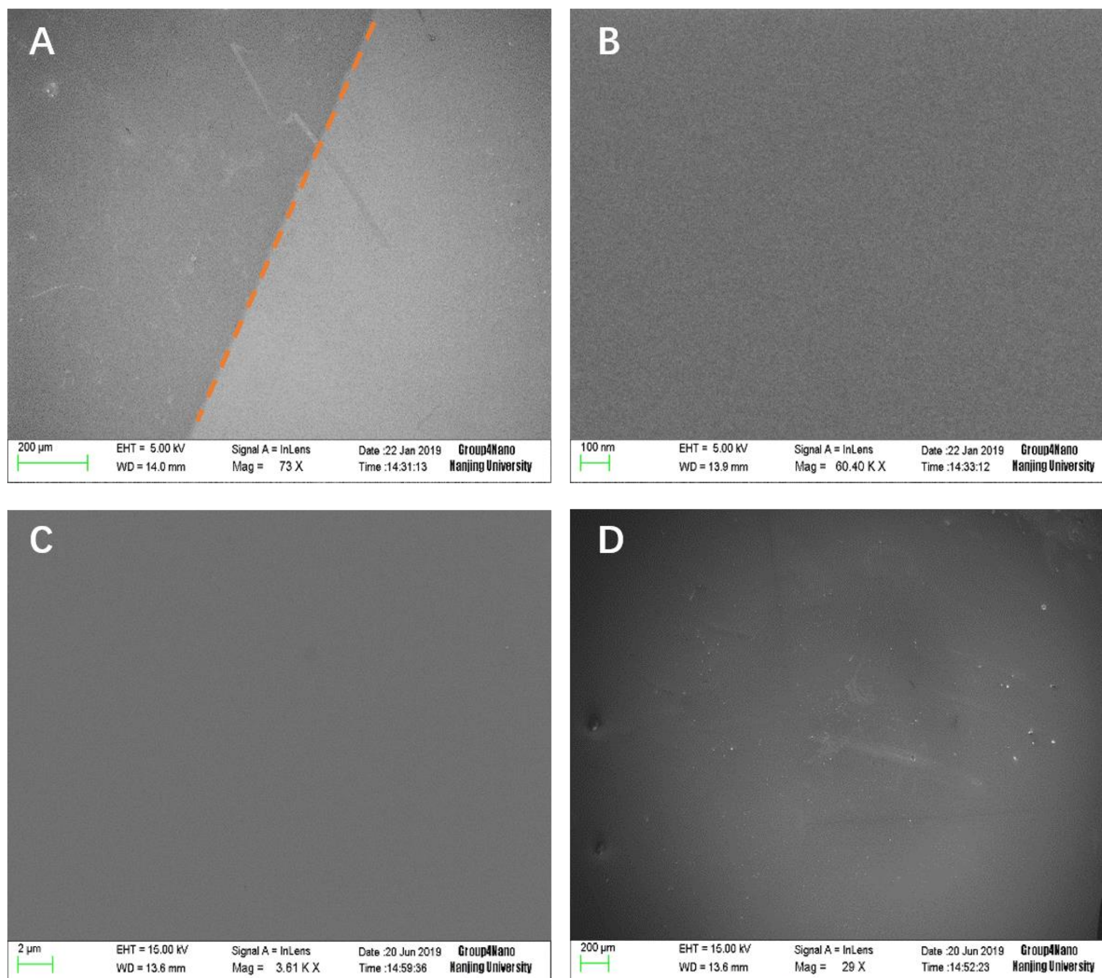

Fig 8.6 the SEM measurement images of PtS2 morphology. (A) the clamp boundary (orange dash line) between GaAs substrate and PtS2 with scale bar $200\ \mu m$. (B, C and D) center area of the sample with different resolution of $100\ nm$, $2\ \mu m$ and $200\ \mu m$ scale bar.

8.6 AFM Measurement of PtS_2

Atomic force microscopy (AFM), an analytical instrument, can be used to study the surface structure of solid materials including insulators. It studies the surface structure and properties of materials by detecting the extremely weak atomic interaction between the surface of the sample to be tested and a micro force sensing element. Atomic Force Microscopy is a surface technique widely used for investigating surface morphology and thickness. The AFM image is performed in either contact or tapping mode, using the repulsive Van der Waal force between the atoms at the tip and those of the surface. A laser beam focuses onto the cantilever, and then reflection of the beam from the cantilever is collected by a photodetector consisting of two photodiodes.

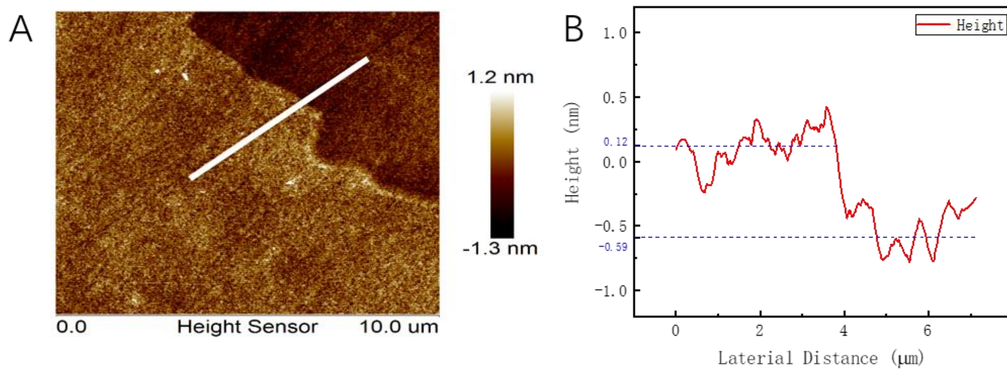

Fig 8.7 the AFM measurement of platinum disulfide monolayer. (A) the AFM image of the stair between the PtS_2 monolayer and GaAs substrate. (B) the height curve of the sample with the thickness of 0.71nm.

The sample PtS_2/GaAs was grown in ultra-high vacuum MBE chamber of base pressure $3 \times 10^{-10} mbar$, and then was taken measurement of ex-situ AFM. The AFM measurement was done in the Department of physics Nanjing university. The AFM equipment was produced by Oxford Instrument which can provide high-precision and high-resolution measurement.

The sample is clamped on the sample table by two molybdenum clamps, so the film will appear steps at the edge of the molybdenum flake. This step is the thickness of the

single-layer PtS_2 on the GaAs substrate as shown in Fig.8.7A.

From Fig.8.7A, the monolayer of PtS_2 completely cover the GaAs substrate on the left of Fig.8.7A, and there are only few humps on the surface. To the right of the edge is the GaAs substrate, which is clean and flat. The thickness of single-crystal monolayer of PtS_2 grown on the GaAs substrate was 0.71nm, which is corresponding with the previous studies from 6.7Å to 8.6Å [116].

8.7 PtS_2 Theoretical Calculation and Analysis

The crystal structure of single-layer 1T-PtS_2 is shown in Fig.8.8, which is hexagonal honeycomb structure. Each Pt atom forms octahedral coordination with six S atoms, and its lattice constant is a = b = 3.58 Å. The lattice constant in this section is from previous studies[116].

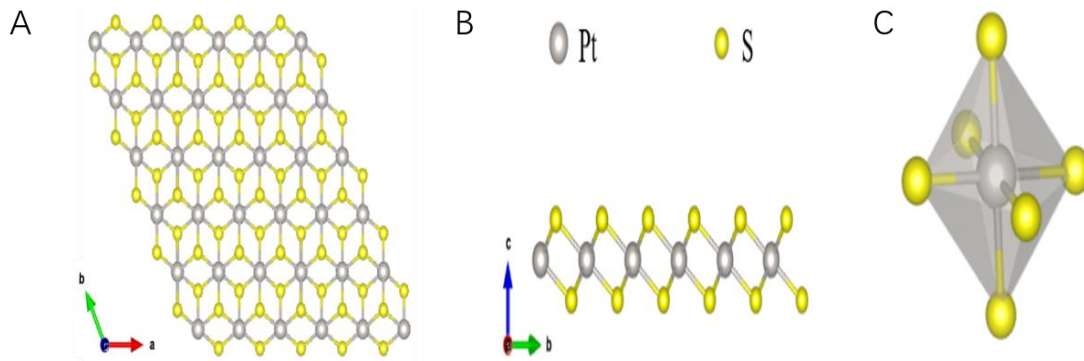

Fig 8.8 The atomic structure of PtS_2 monolayer: (A) top view, (B) side view, (C) coordination diagram of polyhedron.

By using a similar method with CoS_2, four kinds of magnetic configurations are considered, including the non-magnetic state (NM), the ferromagnetic state (FM) and two kinds of hypocritical antiferromagnetic states (AFM1, AFM2). The calculated results are shown in Table 5, which the energy of the non-magnetic state of single-layer PtS_2 is the lowest. It is shown the magnetic moment of each atom in the ground state and the total magnetic moment of unit cell in Table 6.

System	ΔE_{FM-NM} /meV	$\Delta E_{AFM1-NM}$ /meV	$\Delta E_{AFM2-NM}$ /meV
PtS_2	406.571	358.529	396.137

Table. 5 Energy difference between nonmagnetic and FM, AFM1, AFM2 of single layer PtS_2.

System	M_{Pt} /μB	M_S /μB	M_{Total} /μB
PtS_2	0	0	0

Table. 6 The magnetic moment of each atom and the total magnetic moment of unit cell in the ground state system of single layer PtS_2.

The electronic band structure and density of states of single-layer PtS_2 are shown in Fig.8.9, showing indirect band gap semiconductor properties, and the band gap is 1.80 eV. According to the density of states diagram, the upward and downward density of states are completely symmetrical, which also verifies that single-layer PtS_2 does not have ferromagnetism.

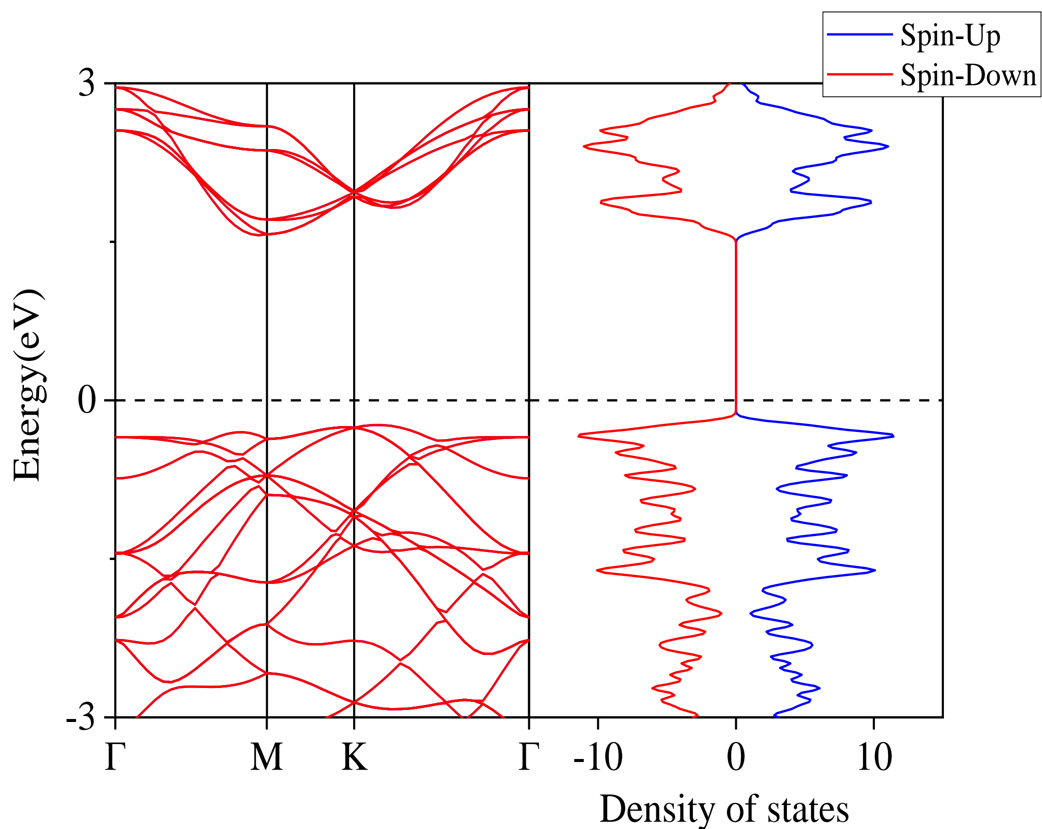

Fig 8.9 The electronic band structure and density of states diagram of single layer PtS_2. The blue and red lines indicate spin up and spin down respectively. The Fermi level is 0 eV.

8.8 Summary of Findings and Discussion

In this section, monolayer of 2D material PtS_2 firstly was grown on passivated GaAs (111) by MBE chamber. The high-quality of monolayer PtS_2 film was proven by in-situ RHEED, XPS, SEM, AFM. These measurements are verified and analyzed from the aspects of lattice structure, chemical composition, film coverage and film thickness.

In situ RHEED measurements show that the single-layer platinum disulfide film was single crystal and can have self-assembly characteristics (from amorphous to single crystal), which this feature can also be seen in growth of cobalt disulfide. This indicates that the self-assembly of atoms in the growth mode is universal.

Ex-situ XPS indicate that the chemical component of the film is PtS_2, and platinum disulfide film is antioxidant. The peak positions of Pt $4f$ and S $2s$ in platinum disulfide are consistent with the characteristic peaks of platinum disulfide. The single chemical phase of the sample film can be derived from the platinum $4f_{7/2}$, $4f_{5/2}$ and sulfur $2s$ electron peaks.

SEM measurements is strong evidence that 100% coverage of monolayer PtS_2 was grown on substrate. Up to now, there is no vacuum growth method to prepare two-dimensional single crystal films with 100% coverage. After AFM measurement, we can confirm that the film is a single atomic layer film, and its thickness is highly consistent with the previous report [116].

The theoretical calculation reveals that single-crystal monolayer PtS_2 is a semiconductor with band gap of 1.8 eV. Due to deposition on GaAs (111), the PtS_2 morphology should as traditional 2D TMDC structure such as MoS_2. As the result of magnetic monument, the PtS_2 should not present any magnetic and antiferromagnetic properties.

For the growth of platinum disulfide, we use the similar method of cobalt disulfide growth, that is, two-step method (passivation and MBE growth). The sulfur passivation layer can reduce the wetting angle, reduce the surface energy, and increase the co-s bond energy, so that a two-dimensional thin film can be formed on the S / GaAs surface

All in all, we can prepare single crystal PtS_2 thin films with large area by a novel growth

method. This preparation method has not been reported before, and the film had the characteristics of single crystal, high quality, homogenous phase without impurities and full coverage of the substrate GaAs (111). The quality of film owe to S-passivation method, which is a novel way to obtain well-grown monolayer films.

Conclusions

First of all, through a large number of background studies, this project has determined the possibility of single crystal transition metal sulfide MBE growth by using passivated film.

Sulfur passivation will combine the sulfur atoms with the gallium atoms (or arsenic atoms) on the symmetry broken gallium arsenide surface, reduce the surface bond energy, and obtain a smaller wetting angle θ.

Moreover, surfactant, which plays an important role in the growth of thin films, is an element that can be segregated on the surface. It can significantly change the surface energy (or surface tension), improve the wettability of the substrate when the film nucleates, and significantly reduce the surface roughness of the film. the sulfur deposited on the surface of GaAs by passivation plays the role of surfactant. When the transition metal grows, the sulfur surface can significantly improve the growth process. At the same time, because the sulfur element is passivated to the surface of the sample, it can also overcome the defects of the film during nucleation. The growth principle of two-dimensional binary semiconductor is similar to that of single metal MBE. This method greatly reduces the difficulty and uncertainty of growth, and also improves the film quality of two-dimensional single-layer TMDC.

The translational symmetry or surface periodicity of the crystal should continue to infinity. The appearance of the surface means the periodic interruption, so the surface is also a kind of crystal defect. The additional energy caused by surface is very high, especially for strongly bonded crystals. Therefore, the method of sulfur-passivation can form a layer of sulfur on the surface of GaAs.

in order to improve the quality of transition metal disulfide single-layer films, a new growth mode is explored from the perspective of chemical energy, and a more suitable growth method is found. By passivating sulfur on GaAs substrate and heating the substrate, higher substrate chemical bond energy can be achieved. In previous studies, similar studies on the growth of transition metal selenides were researched . Better

quality films can be obtained by passivation of selenium on GaAs substrate and growth of transition metal selenides[58]. Similarly, there are some studies on the growth of transition metal selenides using sulfur passivation. These studies show that the sulfur atoms on the surface of GaAs can promote the film quality of transition metal selenides grown by MBE to be better[68].

In the experiment of this project, we passivated the GaAs (111) B surface with ammonium sulfide solution, and got some similar data with the previous reports[58, 85]. However, we also had some new findings, such as the AFM images of sulfur surface, which had unidirectionally aligned domains on the GaAs substrate. According to previous reports of similar structure, the reason for unidirectionally aligned domains may be step edge mediated nucleus.

We have grown two-dimensional transition metal sulfides on GaAs substrates previously passivated by sulfur atoms. Using a previously sulfur-passivated gallium arsenide substrate for two-dimensional transition metal sulfide materials growth, we have grown a layered cobalt disulfide monolayer film for the first time and measured its low-temperature magnetoresistance. In the previous research, there are no any reports for successfully synthesized layered single-crystal CoS_2 films. Therefore, this work is pioneering for the growth of layered two-dimensional materials CoS_2. Moreover, through this growth method, we have also obtained a large area of flat single-layer films.

Not only a single layer of cobalt disulfide film was successfully grown, but also a single layer of PtS_2 film on S/GaAs substrate by MBE growth. Through this growth mode, the single-crystal monolayer platinum disulfide film can completely cover the gallium arsenide substrate. The chemical composition and thickness of monolayer platinum disulfide are also consistent with previous reports[116]. The MBE growth of monolayer platinum disulfide has not been reported before, so this growth method and growth mode is the first successful growth of large-area single-crystal, and high-quality monolayer platinum disulfide.

Future Work

This project mainly explores the growth methods and sample film quality of new two-dimensional materials through sulfur passivation technology. Layered transition metal sulfide CoS_2 and PtS_2 monolayer films have been proven to be well prepared by this method with large area coverage. It is known from the vacuum growth theory that this growth method can be used to grow all transition metal sulfide monolayer films. In addition to the two materials (CoS_2 and PtS_2) mentioned in this experiment, FeS_2, MnS_2, MoS_2, $Co_xFe_{1-x}S_2$ and $Co_xPt_{1-x}S_2$ films growth were also tried, which in-situ RHEED patterns presented their single-crystal structures. Nonetheless, there is not enough experimental evidence to prove that this growth method can grow all the transition metal disulfides. If we want to have a comprehensive understanding of whether this growth method can grow other transition metal sulfides, we need to try to grow more thin films and make more in-depth measurements and analyses of their structures.

For the growth of CoS_2/GaAs films, structural analysis could be more detailed, such as TEM in the top view and HR-TEM to better analyze the sample structure. The transport measurements for this project were longitudinal magnetic fields, and transverse and polar magnetic fields could be introduced in subsequent studies. Furthermore, the Rxy magnetoresistance needs to be measured to determine more magnetic properties of CoS_2.

For MBE growth of monolayer PtS_2, even the basic structure can be determined by in-situ RHEED, XPS, SEM and AFM measurements, the deeper measurement and analyze should be carried out, such as cross-section and top-view HR-TEM.

Based on this growth method, we can develop many studies on the properties of two-dimensional materials.

For transition metal sulfides, most of the monolayers are direct band gap semiconductors, while the multilayer films are indirect band gap semiconductors. Doped 2D materials are highly possible to obtain high-quality monolayer film by S-passivation MBE growth. It will be a new breakthrough to study the energy band of

doped monolayer transition metal disulfide. Therefore, the research on the band gap of single-layer materials will be an interesting hotspot in the future. Moreover, the doped TMDC materials and some special defeats can induce the magnetism, which has a broad prospect in the future[117-119].

In addition to the above-mentioned future work, two-dimensional material heterostructures will also be the focus of future research. The research of heterostructure will form PN junction, which mainly focuses on electrical properties.

In a word, there will be a lot of work in the future, whether it is the further analysis of the data of this project or the expansion of other fields based on this project, it will be some very attractive work.

Reference

1. Hsieh, D., et al., *A topological Dirac insulator in a quantum spin Hall phase.* Nature, 2008. **452**(7190): p. 970-4.
2. Hsieh, D., et al., *A tunable topological insulator in the spin helical Dirac transport regime.* Nature, 2009. **460**(7259): p. 1101-5.
3. Li, Y.Y., et al., *Intrinsic topological insulator Bi2Te3 thin films on Si and their thickness limit.* Advanced Materials, 2010. **22**(36): p. 4002-7.
4. He, K., et al., *Crossover of the three-dimensional topological insulator Bi2Se3 to the two-dimensional limit.* Nature Phys., 2010. **6**(8): p. 584-588.
5. Chen, Y., et al., *Experimental realization of a three-dimensional topological insulator, Bi2Te3.* Science, 2009. **325**(5937): p. 178-181.
6. Iwata, Y., et al., *In situ reflection high-energy electron diffraction (RHEED) observation of Bi 2 Te 3/Sb 2 Te 3 multilayer film growth.* Journal of crystal growth, 1999. **203**(1): p. 125-130.
7. Murray, C., et al., *Comprehensive tunneling spectroscopy of quasifreestanding MoS2 on graphene on Ir(111).* Phys. Rev. B, 2019. **99**(11).
8. Lin, H., et al., *Growth of environmentally stable transition metal selenide films.* Nature Mater., 2019.
9. Novoselov, K.S., et al., *Electric field effect in atomically thin carbon films.* Science, 2004. **306**(5696): p. 666-669.

10. Ohishi, M., et al., *Spin injection into a graphene thin film at room temperature.* Japanese Journal of Applied Physics Part 2-Letters & Express Letters, 2007. **46**(25-28): p. L605-L607.

11. Zeng, M., et al., *Graphene-based bipolar spin diode and spin transistor: Rectification and amplification of spin-polarized current.* Phys. Rev. B, 2011. **83**(11).

12. Geim, A.K. and I.V. Grigorieva, *Van der Waals heterostructures.* Nature, 2013. **499**(7459): p. 419-25.

13. Wang, Q.H., et al., *Electronics and optoelectronics of two-dimensional transition metal dichalcogenides.* Nature Nanotech., 2012. **7**(11): p. 699-712.

14. Chhowalla, M., et al., *The chemistry of two-dimensional layered transition metal dichalcogenide nanosheets.* Nature Chem., 2013. **5**(4): p. 263-75.

15. Nakano, M., et al., *Layer-by-Layer Epitaxial Growth of Scalable WSe2 on Sapphire by Molecular Beam Epitaxy.* Nano Lett., 2017. **17**(9): p. 5595-5599.

16. Mak, K.F., et al., *Atomically thin MoS2: a new direct-gap semiconductor.* Phys. Rev. Lett., 2010. **105**(13): p. 136805.

17. Novoselov, K.S., et al., *Electric field effect in atomically thin carbon films.* 2004. **306**(5696): p. 666-669.

18. Wang, L., et al., *Epitaxial growth of a 100-square-centimetre single-crystal hexagonal boron nitride monolayer on copper.* Nature, 2019. **570**(7759): p. 91-95.

19. Tongay, S., et al., *Magnetic properties of MoS2: Existence of ferromagnetism.* Appl. Phys. Lett., 2012. **101**(12): p. 123105.

20. Chen, Y., et al., *Achieving Uniform Monolayer Transition Metal Dichalcogenides Film on Silicon Wafer via Silanization Treatment: A Typical Study on WS2.* Adv Mater, 2017. **29**(7).

21. Mannix, A.J., et al., *Synthesis of borophenes: Anisotropic, two-dimensional boron polymorphs.* Science, 2015. **350**(6267): p. 1513-1516.

22. Feng, B., et al., *Experimental realization of two-dimensional boron sheets.* Nature Chem., 2016. **8**(6): p. 563-8.

23. Das, S., et al., *Synthesis, Properties, and Applications of 2-D Materials: A Comprehensive Review.* Crit. Rev. Solid State Mater. Sci., 2014. **39**(4): p. 231-252.

24. Ugeda, M.M., et al., *Giant bandgap renormalization and excitonic effects in a monolayer transition metal dichalcogenide semiconductor.* Nature Mater., 2014. **13**(12): p. 1091-5.

25. Burch, K.S., D. Mandrus, and J.G. Park, *Magnetism in two-dimensional van der Waals materials.* Nature, 2018. **563**(7729): p. 47-52.

26. Kong, D., et al., *Synthesis of MoS2 and MoSe2 films with vertically aligned layers.* Nano Lett., 2013. **13**(3): p. 1341-7.

27. Ashton, M., et al., *Two-Dimensional Half-Metals With Large Spin Gaps.* Nano Lett., 2017.

28. Radisavljevic, B., et al., *Single-layer MoS2 transistors.* Nature Nanotech.,

2011. **6**(3): p. 147-50.

29. Roy, A., et al., *Structural and Electrical Properties of MoTe2 and MoSe2 Grown by Molecular Beam Epitaxy.* ACS Appl. Mater. Interfaces., 2016. **8**(11): p. 7396-402.

30. Yan, M., et al., *High quality atomically thin PtSe2 films grown by molecular beam epitaxy.* 2D Mater., 2017. **4**(4).

31. Fatemi, V., et al., *Magnetoresistance and quantum oscillations of an electrostatically tuned semimetal-to-metal transition in ultrathin WTe2.* Phys. Rev. B, 2017. **95**(4).

32. Xu, X., et al., *Spin and pseudospins in layered transition metal dichalcogenides.* Nature Phys., 2014. **10**(5): p. 343-350.

33. Glazov, M.M., et al., *Spin and valley dynamics of excitons in transition metal dichalcogenide monolayers.* Phys. Status. Solidi B, 2015. **252**(11): p. 2349-2362.

34. Buscema, M., et al., *The effect of the substrate on the Raman and photoluminescence emission of single-layer MoS2.* Nano Research, 2015. **7**(4): p. 561-571.

35. Pletikosic, I., et al., *Electronic structure basis for the extraordinary magnetoresistance in WTe2.* Phys. Rev. Lett., 2014. **113**(21): p. 216601.

36. Ohuchi, F.S., et al., *van der Waals epitaxial growth and characterization of MoSe2 thin films on SnS2.* J. Appl. Phys., 1990. **68**(5): p. 2168-2175.

37. Wang, H., et al., *High-quality monolayer superconductor NbSe2 grown by*

chemical vapour deposition. Nat. Commun., 2017. **8**(1): p. 394.

38. Brent, J.R., N. Savjani, and P. O'Brien, *Synthetic Approaches to Two-Dimensional Transition Metal Dichalcogenide Nanosheets.* Prog. Mater. Sci., 2017.

39. Mao, N., et al., *Solvatochromic effect on the photoluminescence of MoS(2) monolayers.* Small, 2013. **9**(8): p. 1312-5.

40. Bhimanapati, G.R., et al., *Recent advances in two-dimensional materials beyond graphene.* 2015.

41. Desai, S.B., et al., *MoS2 transistors with 1-nanometer gate lengths.* Science, 2016. **354**(6308): p. 99-102.

42. Liu, L., I. Kankam, and H.L. Zhuang, *Single-layer antiferromagnetic semiconductor CoS2 with pentagonal structure.* Phys. Rev. B, 2018. **98**(20).

43. Faber, M.S., et al., *High-performance electrocatalysis using metallic cobalt pyrite (CoS(2)) micro- and nanostructures.* J Am Chem Soc, 2014. **136**(28): p. 10053-61.

44. Yu, Z.X., et al., *The structure of the CoS2(100)-(1 × 1) surface.* J. Phys: Condens. Matter, 2007. **19**(15).

45. Caban-Acevedo, M., et al., *Efficient hydrogen evolution catalysis using ternary pyrite-type cobalt phosphosulphide.* Nat Mater, 2015. **14**(12): p. 1245-51.

46. Brown, P.J., et al., *Magnetization distribution in CoS2; is it a half metallic*

ferromagnet? J. Phys.: Condens. Matter, 2005. **17**(10): p. 1583-1592.

47. Elliott, N., *Interatomic Distances in FeS2, CoS2, and NiS2.* J. Chem. Phys., 1960. **33**(3): p. 903-905.
48. Cai, P.L., et al., *Drastic Pressure Effect on the Extremely Large Magnetoresistance in WTe2: Quantum Oscillation Study.* Phys. Rev. Lett., 2015. **115**(5): p. 057202.
49. Yu, H., et al., *Wafer-Scale Growth and Transfer of Highly-Oriented Monolayer MoS2 Continuous Films.* ACS Nano, 2017. **11**(12): p. 12001-12007.
50. Miwa, J.A., et al., *Van der Waals epitaxy of two-dimensional MoS2–graphene heterostructures in ultrahigh vacuum.* ACS Nano, 2015. **9**: p. 6502.
51. Bruix, A., et al., *In situ detection of active edge sites in single-layer MoS2 catalysts.* ACS Nano, 2015. **9**(9): p. 9322-9330.
52. Yu, X., et al., *Defect Mitigation of Solution-Processed 2D WSe2 Nanoflakes for Solar-to-Hydrogen Conversion.* Nano Lett., 2017. **18**(1): p. 215-222.
53. Lee, J., et al., *Valley magnetoelectricity in single-layer MoS2.* Nature Mater., 2017. **16**(9): p. 887-891.
54. Zeng, Z., et al., *Single-layer semiconducting nanosheets: high-yield preparation and device fabrication.* Angew. Chem. Int. Ed., 2011. **50**(47): p. 11093-7.
55. Frindt, R.F., *Single Crystals of MoS2 Several Molecular Layers Thick.* J. Appl.

Phys., 1966. **37**(4): p. 1928-1929.

56. Fei, Z., et al., *Edge conduction in monolayer WTe2.* Nature Phys., 2017.
57. Liu, G., et al., *MoS2 monolayer catalyst doped with isolated Co atoms for the hydrodeoxygenation reaction.* Nat Chem, 2017. **9**(8): p. 810-816.
58. Yamamoto, H., et al., *Improved heteroepitaxial growth of layered NbSe2 on GaAs (111)B.* J. Vac. Sci. Technol. A, 1994. **12**(1): p. 125-129.
59. Diaz, H.C., et al., *Direct observation of interlayer hybridization and Dirac relativistic carriers in graphene/MoS(2) van der Waals heterostructures.* Nano Lett., 2015. **15**(2): p. 1135-40.
60. Peng, J.-P., et al., *Molecular beam epitaxy growth and scanning tunneling microscopy study ofTiSe2ultrathin films.* Phys. Rev. B, 2015. **91**(12).
61. Krumrain, J., et al., *MBE growth optimization of topological insulator Bi 2 Te 3 films.* Journal of crystal growth, 2011. **324**(1): p. 115-118.
62. Kou, X.F., et al., *Magnetically doped semiconducting topological insulators.* J. Appl. Phys., 2012. **112**(6): p. 063912.
63. Tsipas, P., et al., *Massless Dirac Fermions in ZrTe2 Semimetal Grown on InAs(111) by van der Waals Epitaxy.* ACS Nano, 2018. **12**(2): p. 1696-1703.
64. Van Vleck, J.H., *On the Theory of Antiferromagnetism.* The Journal of Chemical Physics, 1941. **9**(1): p. 85-90.
65. Nagamiya, T., K. Yosida, and R. Kubo, *Antiferromagnetism.* Advances in Physics, 1955. **4**(13): p. 1-112.
66. Chahara, K.i., et al., *Magnetoresistance in magnetic manganese oxide with*

intrinsic antiferromagnetic spin structure. Appl. Phys. Lett., 1993. **63**(14): p. 1990-1992.

67. Guo, Z.-F., K. Pan, and X.-J. Wang, *Electrochromic & magnetic properties of electrode materials for lithium ion batteries.* Chin. Phys. B, 2016. **25**(1).

68. Ohtake, A. and Y. Sakuma, *Evolution of surface and interface structures in molecular-beam epitaxy of MoSe2 on GaAs (111) A and (111) B.* Crystal Growth Design, 2016. **17**(1): p. 363-367.

69. Ohtake, A. and Y. Sakuma, *Heteroepitaxy of MoSe2 on Si (111) substrates: Role of surface passivation.* Appl. Phys. Lett., 2019. **114**(5): p. 053106.

70. Murray, C., et al., *Comprehensive tunneling spectroscopy of quasifreestanding MoS 2 on graphene on Ir (111).* 2019. **99**(11): p. 115434.

71. Waldrop, J.R. and R.W. Grant, *Interface chemistry of metal-GaAs Schottky-barrier contacts.* Appl. Phys. Lett., 1979. **34**(10): p. 630-632.

72. Meiners, L., *Electrical properties of the gallium arsenide–insulator interface.* J. Vac. Sci. Technol., 1978. **15**(4): p. 1402-1407.

73. Zeisse, C., L. Messick, and D. Lile, *Electrical properties of anodic and pyrolytic dielectrics on gallium arsenide.* J. Vac. Sci. Technol. , 1977. **14**(4): p. 957-960.

74. Yablonovitch, E., et al., *Nearly ideal electronic properties of sulfide coated GaAs surfaces.* Appl. Phys. Lett, 1987. **51**(6): p. 439-441.

75. Sandroff, C.J., et al., *Dramatic enhancement in the gain of a GaAs/AlGaAs heterostructure bipolar transistor by surface chemical passivation.* Appl.

Phys. Lett, 1987. **51**(1): p. 33-35.

76. Spindt, C.J., et al., *Vacuum ultraviolet photoelectron spectroscopy of (NH4)2S-treated GaAs (100) surfaces.* Appl. Phys. Lett., 1989. **55**(9): p. 861-863.

77. Oigawa, H., et al., *Studies on an (NH4) 2Sx-Treated GaAs Surface Using AES, LEELs and RHEED.* Japanese Journal of Applied Physics, 1989. **28**(3A): p. L340.

78. Fan, J.-F., H. Oigawa, and Y. Nannichi, *Metal-dependent Schottky barrier height with the (NH4) 2Sx-treated GaAs.* Japanese Journal of Applied Physics, 1988. **27**(11A): p. L2125.

79. Takahisa, O., *Passivation of GaAs (001) surfaces by chalcogen atoms (S, Se and Te).* Surf. Sci., 1991. **255**(3): p. 229-236.

80. Xia, H., et al., *Absolute coverage measurements on sulphur-passivated GaAs (100).* Surf. Sci., 1995. **324**(2-3): p. 159-168.

81. Sandroff, C., et al., *Electronic passivation of GaAs surfaces through the formation of arsenic—sulfur bonds.* Appl. Phys. Lett., 1989. **54**(4): p. 362-364.

82. Carpenter, M., et al., *Investigations of ammonium sulfide surface treatments on GaAs.* J. Vac. Sci. Technol. B, 1989. **7**(4): p. 845-850.

83. Hirayama, H., et al., *Reflection high-energy electron diffraction and x-ray photoelectron spectroscopic study on (NH4) 2S x-treated GaAs (100) surfaces.* Appl. Phys. Lett., 1989. **54**(25): p. 2565-2567.

84. Moriarty, P., et al., *Chemical bonding and structure of the sulfur treated GaAs (111) B surface.* Appl. Phys. Lett., 1995. **67**(3): p. 383-385.

85. Berkovits, V., et al., *Chemistry of wet treatment of GaAs (111) b and GaAs (111) a in hydrazine-sulfide solutions.* Journal of The Electrochemical Society, 2011. **158**(3): p. D127-D135.

86. Ohno, T., *Sulfur passivation of GaAs surfaces.* Physical Review B, 1991. **44**(12): p. 6306.

87. Bringans, R., et al., *Arsenic-terminated Ge (111): An ideal 1× 1 surface.* Phys. Rev. Lett., 1985. **55**(5): p. 533.

88. Bickel, J.E., C. Pearson, and J.M. Millunchick, *Sb incorporation at GaAs(001)-(2×4) surfaces.* Surf. Sci., 2009. **603**(1): p. 14-21.

89. Ji, D., et al., *Freestanding crystalline oxide perovskites down to the monolayer limit.* 2019. **570**(7759): p. 87.

90. Yang, J., et al., *Formation of two-dimensional transition metal oxide nanosheets with nanoparticles as intermediates.* Nature Mater., 2019. **18**(9): p. 970-976.

91. Liu, Y., Y. Huang, and X. Duan, *Van der Waals integration before and beyond two-dimensional materials.* Nature, 2019. **567**(7748): p. 323-333.

92. Koma, A., K. Saiki, and Y. Sato, *Heteroepitaxy of a two-dimensional material on a three-dimensional material.* Appl. Surf. Sci., 1990. **41**: p. 451-456.

93. A.Braginski, J.C., *The SQUID handbook: Applications of SQUIDs and SQUID systems.* John Wiley & Son, 2006.

94. Nasr Esfahani, M., et al., *Monolithic technology for silicon nanowires in high-topography architectures.* Microelectronic Engineering, 2017. **183-184**: p. 42-47.

95. Nasr Esfahani, M., *Surface stress effects on the mechanical properties of silicon nanowires: A molecular dynamics simulation.* Journal of Applied Physics, 2019. **125**(13).

96. Ziaei, S.M.R., A.H. Kokabi, and M. Nasr-Esfehani, *Sulfide stress corrosion cracking and hydrogen induced cracking of A216-WCC wellhead flow control valve body.* Case Studies in Engineering Failure Analysis, 2013. **1**(3): p. 223-234.

97. Yablonovitch, E., et al., *Nearly ideal electronic properties of sulfide coated GaAs surfaces.* Appl. phys. lett, 1987. **51**(6): p. 439-441.

98. Scimeca, T., et al., *Temperature-dependent changes on the sulfur-passivated GaAs (111)A, (100), and (111)Bsurfaces.* Phys. Rev. B, 1991. **44**(23): p. 12927-12932.

99. Anderson, G.W., M.C. Hanf, and P.R. Norton, *Growth and Magnetic Properties of Epitaxial Fe(100) on S-Passivated GaAs(100).* Phys. Rev. Lett., 1995. **74**(14): p. 2764-2767.

100. Lu, Z.H., et al., *Structure of S on passivated GaAs (100).* Appl. Phys. Lett., 1993. **62**(23): p. 2932-2934.

101. Murphy, B., et al., *Chemical and structural studies of the interactions of molecular sulfur with the GaAs (111) A and GaAs (111) B surfaces.* Surf. Sci.,

1994. **317**(1-2): p. 73-83.

102. Van der Heide, H., et al., *X-ray photoelectron spectra of 3d transition metal pyrites.* J. Solid State Chem, 1980. **33**(1): p. 17-25.

103. Utyuzh, A.N., *Influence of temperature on raman spectra of the FeS2 single crystal with pyrite structure.* Physics of the Solid State, 2014. **56**(10): p. 2050-2055.

104. Zhu, L., et al., *Investigation of CoS2-based thin films as model catalysts for the oxygen reduction reaction.* Journal of Catalysis, 2008. **258**(1): p. 235-242.

105. Ahmad, E., et al., *Hysteretic properties of epitaxial Fe/GaAs(100) ultrathin films under external uniaxial strain.* J. Appl. Phys., 2004. **95**(11): p. 6555-6557.

106. Morley, N.A., et al., *Magnetostriction and magnetocrystalline anisotropy constants of ultrathin epitaxial Fe films on GaAs, with Au overlayers.* Journal of Physics: Condensed Matter, 2005. **17**(7): p. 1201-1208.

107. Morley, N.A., et al., *MOKE hysteresis loop method of determining the anisotropy constants of ferromagnetic thin films: fe on GaAs(100) with overlayers of Au and Cr.* Journal of Magnetism and Magnetic Materials, 2006. **300**(2): p. 436-444.

108. Rao, S.S., et al., *Weakening of charge order and antiferromagnetic to ferromagnetic switch over in Pr0.5Ca0.5MnO3 nanowires.* Applied Physics Letters, 2005. **87**(18).

109. Rao, S.S., et al., *Suppression of charge order, disappearance of antiferromagnetism, and emergence of ferromagnetism inNd0.5Ca0.5MnO3nanoparticles.* Physical Review B, 2006. **74**(14).

110. S. Cristol, J.F.P., and E. Payen, *Theoretical Study of the MoS2 (100) Surface: A Chemical Potential Analysis of Sulfur and Hydrogen Coverage.* J. Phys. Chem. B, 2000. **104**.

111. Yang, H., et al., *Giant anomalous Nernst effect in the magnetic Weyl semimetal Co3Sn2S2.* Phys. Rev. Mater., 2020. **4**(2).

112. John P. Perdew, K.B., Matthias Ernzerhof, *Generalized Gradient Approximation Made Simple.* Phys. Rev. Lett., 1996. **77**(18).

113. S. K. Kwon, S.J.Y., and B. I. Min, *Itinerant ferromagnetism in half-metallic CoS2.* Phys. Rev. B, 2000. **62**: p. 4.

114. Balog, R., et al., *Bandgap opening in graphene induced by patterned hydrogen adsorption.* Nat Mater, 2010. **9**(4): p. 315-9.

115. MacNeill, D., et al., *Breaking of valley degeneracy by magnetic field in monolayer MoSe2.* Phys. Rev. Lett., 2015. **114**(3): p. 037401.

116. Zhao, Y., et al., *Extraordinarily Strong Interlayer Interaction in 2D Layered PtS2.* Adv. Mater., 2016. **28**(12): p. 2399-407.

117. Wang, Y., et al., *Defects engineering induced room temperature ferromagnetism in transition metal doped MoS 2.* Mater. Des., 2017. **121**: p. 77-84.

118. Tao, P., et al., *Strain-induced magnetism in MoS2 monolayer with defects.*

J. Appl. Phys., 2014. **115**(5): p. 054305.

119. Zheng, H.L., et al., *Tuning magnetism of monolayer MoS2 by doping vacancy and applying strain.* Appl. Phys. Lett., 2014. **104**(13): p. 132403.